INVESTIGATIONS ON WAVE PROPAGATION THROUGH PSEUDO-RANDOM-PHASE-PLATE USING He-Ne LASER AT 633 nm

A thesis submitted
in partial fulfillment for the degree of

Doctor of Philosophy

by

RICHA SHARMA

INDIAN INSTITUTE OF SPACE SCIENCE AND TECHNOLOGY
Thiruvananthapuram

September, 2015

CERTIFICATE

This is to certify that the thesis titled **Investigations on Wave Propagation Through Pseudo-Random-Phase-Plate Using He-Ne Laser at 633 nm**, submitted by **Richa Sharma**, to the Indian Institute of Space Science and Technology, Thiruvananthapuram, for the award of the degree of **Doctor of Philosophy**, is a bonafide record of the research work done by her under my supervision. The contents of this thesis, in full or in parts, have not been submitted to any other Institute or University for the award of any degree or diploma.

Prof. C. S. Narayanamurthy
Senior Professor
Department of Physics

Dr. S. Murugesh
Associate Professor & Head
Department of Physics

Place: Thiruvananthapuram
September, 2015

DECLARATION

I declare that this thesis titled **Investigations on Wave Propagation Through Pseudo-Random-Phase-Plate Using He-Ne Laser at 633 nm** submitted in fulfillment of the Degree of Doctor of Philosophy is a record of original work carried out by me under the supervision of **Prof. C. S. Narayanamurthy**, and has not formed the basis for the award of any degree, diploma, associateship, fellowship or other titles in this or any other Institution or University of higher learning. In keeping with the ethical practice in reporting scientific information, due acknowledgments have been made wherever the findings of others have been cited.

Place: Thiruvananthapuram
September, 2015

Name : Richa Sharma
Roll No. : SC10D008

ACKNOWLEDGMENTS

I would like to take this opportunity to thank IIST for giving me a podium to emerge and bloom as a research scholar. Under the watchful eye of my supervisor *Prof. C. S. Narayanamurthy*, I was exposed to all sorts of challenging situations during my tenure. I owe my present achievements and future preparedness to his guidance and support.

A sincere thanks to IIST director *Dr. K.S. Dasgupta* and my doctoral committee members, *Dr. Thomas Kurian*, *Prof. R. M. Vasu*, *Prof. S. K. Saha*, *Dr. Umesh Kadhane* and *Dr. A. K. Gupta* for timely evaluation and delightful discussions on my research topic and its possible scope and directions.

I would also like to thank *Dr. J Soloman Ivan* for a brief stint of insightful discussions and brain storming sessions which gave me an opportunity to delve deeper into my argumentative self and eventually end up tasting the fruits of a sweet success.

I would especially like to thank my contemporaries, who inculcated in me a habit of asking questions and analyzing mundane situations in a meticulous scientific way which helped me weed out many redundancies and carve a clear research path for myself.

My family members (*Papa, Mummy, Shikha didi and Shelly*), who all this while understood my non-attendance at many key events back home, are to be thanked for their patience with me. Their acceptance of my work nature and their constant support and encouragement has made me cross many hurdles.

Last but not the least, I would like to thank *Ameya Kesarkar* for being a blessing. He has been my constant unwaivering support that has helped me cut through my trying times. His presence in my success and failures alike has made me a better researcher and most importantly a better person.

ABSTRACT

Turbulence mimicking media in experimental laboratories have proved to be very helpful for investigating the properties and effects of a realistic turbulent medium. Researchers have constantly attempted on improvising the existing turbulence mimicking capacities to create robust and repeatable turbulence models for laboratory purposes. In this thesis, Pseudo-Random-Phase-Plates (PRPPs) which belong to the class of aforesaid media have been investigated by using a 633 nm He-Ne laser wave-field.

In the first place, a collimated 633 nm laser wave-field is used in two classical interferometers namely the Mach-Zehnder and the Michelson's interferometer, to determine the nature of PRPPs, which amounts to revealing whether they behave like Kolmogorov or non-Kolmogorov turbulence simulators. It is found that the two PRPPs in question behave like non-Kolmogorov turbulence simulators at $633\,\mathrm{nm}$ wavelength, whether used individually or as a combination. It is also observed that the behavior of PRPPs tends to approach towards Kolmogorov turbulence regime on increasing the number of passages of wave-field through them. Also, to discuss one of the applications of the characterized PRPPs, a phase-sharing experiment involving a Mach-Zehnder interferometer using a PRPP as object in one of the interferometric arms is mentioned.

This is followed by wave-propagation analysis using the Variance matrix on the said PRPPs with a 633 nm laser wave-field. Variance matrix, along with some derivable physical quantities is calculated using the Shack-Hartmann-Wavefront-Sensor (SHWFS) data at different propagation distances. The estimated quantities for a wave-field subjected to a propagation through PRPP (either once or twice) are compared with those for a wave-field not subject to a propagation through the PRPP. The comparison though shows an increased fluctuation in all the quantities with a passage through the PRPP, but it also reveals a decreased wave-field asymmetry on an average.

Towards the end, an attempt on PRPP characterization is made using the standard statistical parameters usually used for characterizing surface roughness.

TABLE OF CONTENTS

LIST OF TABLES

LIST OF FIGURES

ABBREVIATIONS

SHWFS	Shack-Hartmann-Wavefront-Sensor
PRPPs	Pseudo-Random-Phase-Plates
PRPP	Pseudo-Random-Phase-Plate
NIM	Near Index Matching
TEM	Transverse-Electro-Magnetic
MLA	Micro-Lens-Array
WFS	Wave-Front-Sensor
CCD	Charge-Coupled-Device
ND	Neutral Density Filter
SFA	Spatial Filtering Assembly
HWP	Half Wave Plate
PBS	Polarization Beam Splitter
L	Lens
BS	Beam Splitter
He-Ne	Helium Neon
M	Mirror
RMS	Root Mean Square

NOTATIONS

Re	Real
D_ϕ	Phase Structure Function
r_0	Fried's Coherence Length
ϕ	Phase
C_n	Refractive Index Structure Constant
$\mathbb{R}$	Set of Real Numbers
Sp	Symplectic Group
V	Variance Matrix
κ	Symplectic Eigen Value
τ	Twist
V_δ	Distance Measure between two Variance Matrices
V_{as}	Asymmetry Measurement Criterion
f	Focal Length
R_a	Roughness Average
R_q	Standard Deviation
R_t	Peak to Valley distance

CHAPTER 1

Introduction

In nature, one often encounters turbulent media having an inherent capacity of introducing random fluctuations in refractive index in the path of a beam propagating through them. The effects of these fluctuations in a beam's path can be seen in the resultant wave-field. It is important to study such a wave-field as this can throw some light on aspects related to turbulence. In laboratories, such a study can be carried out using turbulence mimicking media. Pseudo-Random-Phase-Plates (PRPPs) are a class of such turbulence mimicking media and in this thesis, these have been investigated, using a 633 nm laser wave-field.

1.1 Literature Survey and Motivation

Owing to the ubiquitous presence of turbulent media in nature, the study of their effects on the wave-fields propagating through them has been a subject of great interest over the years for the researchers *Strohbehn (1968); Sasiela (2007); Al-Habash et al. (2001); Rickett (1990); Fried (1966); Conan et al. (1995); Andrews and Phillips (2005)*. It is a well known fact that when a coherent wave-field propagates through a turbulent medium, *random* changes are acquired in both its amplitude as well as phase *Andrews and Phillips (2005); Ishimaru (1978); Charnotskii (2013); Tatarskii (1971); Booker et al. (1950); Roddier (1981); Tatarskii (1961)*.

It is important to note that the atmospheric turbulence is one such interesting turbulent medium and the study of an optical wave-field propagating through it has implications in fields such as adaptive optics *Beckers (1993); Roddier (1999); Tyson (2010); Hardy (1998); Vorontsov and Shmalgauzen (1985)*, optical communication *McAulay and Li (1999); Andrews and Phillips (2005); Zhu and Kahn (2002); Paterson (2005); Li et al. (2007); Nistazakis et al. (2009); Ricklin and Davidson (2003)*, optical imaging *Roggemann et al. (1996); Conan et al. (1995); Charnotskii et al. (1990); Tubbs (2003); Buades et al. (2005)* etc.

Past attempts on studying and characterizing such turbulence have resulted in some seminal works by researchers like A.N. Kolmogorov *Kolmogorov (1941)*, V.I. Tatarskii *Tatarskii (1961, 1971)* etc. Kolmogorov, in his work on the statistics of turbulent flow *Kolmogorov (1941)*, derived an expression for the velocity structure function in a turbulent flow, given by,

$$D_v(r) = \langle [v(\mathbf{r_i} + \mathbf{r}) - v(\mathbf{r_i})]^2 \rangle = C_v^2 r^{\frac{2}{3}} \tag{1.1}$$

with $l_0 < r < L_0$. The angle brackets in the above expression denote the statistical expectation operator, the scalar r is the magnitude of the vector $\mathbf{r}$, $v(\mathbf{r_i})$ is the velocity vector at point r_i, C_v is the velocity structure constant, l_0 and L_0 are the inner and outer scales, respectively. The domain of r between l_0 and L_0 is called the inertial subrange. This expression was further extended by Tatarskii *Tatarskii (1961)* by first employing the notion of a conservative passive additive to relate the velocity structure function and the structure function for potential temperature and then, by using the Gladstone-Dale relation *Roddier (1981); Shapiro and Strohbehn (1978)*, to derive the expression for refractive index structure function:

$$D_n(r) = \langle [n(\mathbf{r_i} + \mathbf{r}) - n(\mathbf{r_i})]^2 \rangle = C_n^2 r^{\frac{2}{3}} \tag{1.2}$$

where, $n(r_i)$ is the index of refraction at the point r_i and C_n is the index structure constant which represents the strength of turbulence *Tatarskii (1961); Tyson (2010); Hardy (1998)*. Further, many researchers have derived the expressions for the structure functions for amplitude, wavefront and phase as well. The phase structure function has been linked to the strength of atmospheric turbulence in the following manner :

$$D_\phi(r) = 2.914 k^2 r^{\frac{5}{3}} \int_0^\infty C_n^2(h) dh \tag{1.3}$$

wherein, k is the spatial wavenumber and h is the vertical height. The class of turbulence falling within the ambit of these expressions represents the Kolmogorov model for turbulence, which is the most widely accepted and explored model for describing a locally homogeneous, isotropic and incompressible turbulence *Kolmogorov (1941)*. Other models like von Karman and Tatarskii have also been proposed and have further been combined to yield a modified von Karman spectrum which accommodates

the shortcomings of the Kolmogorov model for turbulence, by including the inner and outer scale factors used to describe the size of turbulent eddies *Andrews and Phillips (2005); Roggemann et al. (1996)*.

With these expressions in the background, many scientists have derived other useful statistical parameters for turbulence interpretation. One such parameter is the Fried's parameter, given by D. L. Fried *Fried (1966)*, which relates the statistics of wave distortion in a turbulent medium to optical resolution of the detecting system. Also, Greenwood's frequency *Greenwood (1977); Tyson and Frazier (2004)*, named after its inventor Greenwood, gives a simplified expression for the frequency or bandwidth of an adaptive optics system required for an effective wavefront correction of distorted wavefronts traveling through a turbulent medium. Furthermore, Zernike polynomials are used towards describing aberrations introduced in a wavefront traveling through turbulence *Noll (1976); Roddier (1990); Wang and Silva (1980); Bhatia and Wolf (1954); Mahajan and Shannon (1994)* and Strehl ratio, to check the quality of astronomical seeing in the presence of atmospheric turbulence and evaluate the performance of any adaptive optical correction system *Mahajan (1983); Perrin et al. (2003); Mahajan (1982); Andrews et al. (2006)*.

It is evident that the most widely explored turbulence regime is that of Kolmogorov, though with time, researches have also revealed the possibility of existence of turbulence regimes other than the Kolmogorov regime, often called the non-Kolmogorov turbulence regime *Stribling et al. (1995)*. This has also got support from prompt experimental evidences, which include the observation of non-Kolmogorov statistics in troposphere and stratosphere in the atmosphere *Beland (1995); Buser (1971); Dalaudier et al. (1994); Dayton et al. (1992)*. A flurry of simulations and analysis has since then emerged describing the properties and effects of this turbulence regime on various kinds of wave-fields propagating through it *Rao et al. (2000); Stribling et al. (1995); Toselli et al. (2008, 2007); Boreman and Dainty (1996); Shchepakina and Korotkova (2010); Khrennikov (2000); Korotkova and Shchepakina (2010); Wu et al. (2010); Zilberman et al. (2008)*.

In order to study the effects of different turbulence regimes on propagating wavefields, researchers usually engage in the development of a realistic, well-defined and repeatable turbulence at laboratory level. Such turbulence-mimicking capacities also prove to be very helpful for accurately validating new generation systems used in areas

such as adaptive optics and optical communication. Several attempts have been made in this regard, which include near index matching *Rhoadarmer et al. (2001)*, hot air chambers *Keskin et al. (2006)*, liquid filled chambers *Davis et al. (1998)*, hair sprays *Thomas (2004)*, spatial light modulators *Phillips et al. (2005)*, paints *Rampy et al. (2012)*, ion exchange phase screens *Hippler et al. (2004)* and surface etching *Jia and Zhang (2012)*. The primary focus of these methods though has remained on experimentally achieving a Kolmogorov turbulence regime, other regimes are also being explored. Such well defined media at laboratory level facilitate the study of the effects that a realistic medium such as that of atmospheric turbulence can bring in on various kinds of wave-fields propagating through them.

One of the important quantities for the study of such a wave-field is the Variance matrix (V). It can capture the changes in wave-field characteristics upon its passage through a turbulent medium at the level of second moments *Simon et al. (1994); Simon and Mukunda (2000)*. The Variance matrix can be easily estimated with the available data for intensity and wave-field centroid position extracted from a Shack-Hartmann-Wavefront-Sensor (SHWFS) *Neal et al. (1996, 1999, 2000); Schäfer and Mann (2000, 2002); Schäfer et al. (2006)*. This does not involve any inbuilt wavefront reconstruction algorithm as is generally the case with SHWFS *Lane and Tallon (1992); Hudgin (1977); Fried (1977); Southwell (1980); Herrmann (1980); van Dam et al. (2002); Talmi and Ribak (2006)*. The Variance matrix estimation is thus universal and repeatable, given the same kind of wave-field. In addition to this, the Variance matrix can also give certain other quantities of physical significance such as the Twist *Allen et al. (1992); Beijersbergen et al. (2003)*, the Symplectic eigenvalues *Simon et al. (1994); Simon and Mukunda (2000)*, and a distance measure between two Variance matrices.

The Twist parameter measures the overall beam twist or rotation along the propagation direction and the Symplectic eigenvalues are direct indicators of the presence of higher-order modes in a laser wave-field. The distance measure between two Variance matrices can be used as an effective tool towards checking the wave-field's symmetry in the *x* and *y* directions and at the same time can compare the asymmetry between two Variance matrices calculated for the same wave-field in two different situations. Further the uncertainty principle, which puts a restriction on the Variance matrices that are physically possible, can be effectively used for the purpose of discarding the invalid data i.e. those Variance matrices which do not obey the principle can be neglected, thus

acting as a check on the experimental estimations of Variance matrices.

As is evident, there are many ways in which one can explore a wave-field that has propagated through turbulence. It is worth mentioning here that, some researchers have recently demonstrated the possibility of using the random phase acquired by a light field on propagation through atmospheric turbulence for cryptographic purposes *Marangon et al. (2014); Drake et al. (2013); Donnangelo et al. (2012)*. In *Marangon et al. (2014)*, random-key generation using phase fluctuations of a light field that has propagated through a turbulent atmosphere was demonstrated. In *Drake et al. (2013); Donnangelo et al. (2012)*, it was shown that the phase acquired by a light field on propagation through atmospheric turbulence like conditions can be used by two remote observers to distill a shared random key.

Motivated from these works, two PRPPs, which have been claimed as turbulence mimicking media *Mantravadi et al. (2004)* are considered in the present thesis, and are characterized at 633 nm wavelength, by using phase extracted from interference fringe patterns in two well known classical interferometric geometries, namely the Mach-Zehnder and the Michelson's interferometer *Born and Wolf (1964)*. The extracted phase in the two geometries is different in the sense that in Mach-Zehnder interferometer, the beam propagates through the object (here PRPP/PRPPs in-a-combination) only once, on the other hand, in Michelson's interferometer, the beam travels twice through the object. The Mach-Zehnder geometry therefore is also called the *single passage* geometry and similarly, the Michelson's geometry is called the *double passage* geometry. This phase introduced to a propagating beam on its passage through the turbulent medium is random and can be effectively used to determine its nature *Ikeda et al. (2005); Popescu et al. (2005); Lue et al. (2009); Xue et al. (2011)* by employing the well documented parameters like the phase structure function. In the present context thus, the PRPPs are analyzed using the phase structure function, and a robust conclusion is drawn on their nature. An interesting phenomenon in which the nature of turbulence depends upon the number of passages the wave-field travels through these media is also witnessed. In fact, a tendency of approaching towards Kolmogorov turbulence regime is observed on increasing the number of passages through the PRPP or PRPPs-in-a-combination. A PRPP then is used as a mediating medium to demonstrate the possibility of sharing a secret key between two observing ends separated by a realistic atmosphere, thus presenting one of the applications of the PRPPs in the field of optical communication.

Further, the Variance matrix of a coherent wave-field is estimated, upon its passage through a PRPP, using the Shack-Hartmann-Wavefront-Sensor (SHWFS). This includes a comparison of the quantities of physical relevance that can be extracted from the Variance matrix, namely the Twist (τ), the Symplectic eigenvalues (κ_1 and κ_2), and a distance measure between two Variance matrices (V_δ). The uncertainty principle, which puts a restriction on the Variance matrices that are physically possible, is effectively used for the purpose of discarding invalid data.

Towards the end of this thesis, on the basis of observation that the extracted phases (from a wave-field that has propagated through a PRPP) resemble random rough surfaces, the statistical parameters routinely used for characterizing surface roughness *Sedlaček et al. (2012); Rhee et al. (2005); Duparre et al. (2002); Banat (2003); Gadelmawla et al. (2002); Kendall and Yule (1950)* are also used for an attempt on PRPP characterization.

Thus, overall, the thesis primarily investigates the PRPPs using a 633 nm He-Ne laser beam. The PRPPs are first characterized as non-Kolmogorov turbulence simulators and further their effects on the propagating 633 nm He-Ne laser beam are explored through the Variance matrix. A possible application of these PRPPs in classical cryptography is also mentioned.

1.2 Research Contributions

The contributions of the thesis are summarized as follows:

1. Characterization of two PRPPs (individually/in-a-combination) as non-Kolmogorov turbulence simulators at 633 nm wavelength using the Mach-Zehnder and Michelson's interferometric geometries.

    - The results reveal wavelength dependence of characteristics of PRPPs.
    - It is observed that on an increase in the number of passages through the PRPP/PRPPs in-a-combination, there is a possibility of achieving Kolmogorov turbulence regime. This trend is found to be more pronounced with individual PRPP than with the PRPPs in-a-combination.

2. A brief mention about the application of PRPP in a phase-sharing scheme, wherein

the PRPP is inserted in one of the arms of the Mach-Zehnder interferometric setup to distill a shared random secret key between two remote observers.

3. Study of a coherent wave-field on its passage through a PRPP using the Variance matrix by computing the quantities of physical interest such as Twist parameter, Symplectic eigenvalues, and a distance measure between two Variance matrices.

4. An attempt on characterization of PRPP by evaluating the standard statistical parameters, which are usually used for characterizing surface roughness.

The chapter-wise organization of this thesis has been given in the next section.

1.3 Organization of Thesis

- Chapter 2 discusses the characterization of PRPPs at 633 nm wavelength, using the two well known classical interferometric geometries, 1) the Mach-Zehnder and 2) the Michelson's interferometer. It also analyses the nature of PRPPs, when used in combinations. The chapter ends with an application of PRPPs in a phase sharing experiment.

- In Chapter 3, a 633 nm laser beam is propagated through PRPP to obtain the corresponding distorted wave-fields at various propagation distances. Also, the undistorted wave-fields are obtained when the PRPP is removed from the propagation path. Subsequently, some physically meaningful quantities are obtained for such distorted and undistorted wave-fields from the Variance matrix calculations.

- Chapter 4 explores another method of PRPP characterization, which involves the usage of standard statistical parameters that are usually used for determining surface roughness.

- Finally, Chapter 5 provides the conclusion of the work and its possible future scope.

CHAPTER 2

Single and Double Passage Interferometric Analysis of Pseudo-Random-Phase-Plates and their Application to Classical Cryptography

2.1 Introduction

In order to simulate atmosphere-like-conditions at the laboratory level, several methods have been attempted by the researchers across the world *Rhoadarmer et al. (2001); Keskin et al. (2006); Davis et al. (1998); Thomas (2004); Phillips et al. (2005); Rampy et al. (2012); Hippler et al. (2004); Jia and Zhang (2012).* Most of these methods try to achieve *Kolmogorov turbulence regime* that simulates either single or multiple layers of atmosphere. Out of them, the one proposed by *Mantravadi et al. (2004)* is a popularly used technique which employs static phase plates manufactured by *Near-Index-Matching (NIM)* process. One usually relies on the PRPPs manufactured by this method for carrying out various experiments on a turbulent medium at the laboratory level.

It is often observed that the manufacturers claim the designed phase plate's behavior as a *Kolmogorov turbulence simulator* at a few specified wavelengths. However, it is quite possible that their behavior falls into non-Kolmogorov turbulence regime at some other wavelength having practical significance. In such cases, before employing the plates for an experiment, it becomes important to check whether they exhibit *Kolmogorov* or *non-Kolmogorov* behaviour at the wavelength under consideration. The present chapter considers two such Pseudo-Random-Phase-Plates (PRPPs) supplied by Lexitek motors (which have been claimed as Kolmogorov turbulence simulators at 1550 nm wavelength by the supplier) and characterizes them at a wavelength of 633 nm . Furthermore, as an application of the PRPPs, the chapter mentions an experiment involving the Mach-Zehnder interferometric geometry with a PRPP in one of its arms for demonstrating the possibility of sharing a secret key between two spatially separated observers.

2.2 Description of Interference, Interferometric Geometries, and PRPPs

This section gives some prior knowledge about the interference phenomenon, the two classical interferometric geometries and the Pseudo-Random-Phase-Plates (PRPPs), which is essential for understanding our experiment (as will be presented later in Section 2.3).

2.2.1 Interference and Interferometers

A superposition of two or more light waves/beams derived from the same source, results in an intensity distribution, in which the maximum has an intensity greater than the summation of two waves and minimum has an intensity reaching towards zero. This is called interference *Born and Wolf (1964)*. The superposition of two strictly monochromatic waves, arising from the same source always gives rise to an interference pattern. This is attributed to the fact that the two waves arising from the same source are correlated to each other in either complete or partial sense, i.e. they are coherent. This can be contrasted with the incoherence of beams arising from different sources, the superposition of which does not result in an interference pattern in ordinary experimental circumstances.

An interference measuring arrangement is referred to as an interferometer. In an interferometer, interference from the same source can be achieved in two ways, which also forms the basis for classifying the interferometric arrangements. The first being, the division of wavefront, in which a beam originating from a point source is divided into two or more point sources by means of apertures placed side by side. An example for the same is Young's double slit experiment. The second is called the division of amplitude, in which the wave amplitude or intensity is in general divided into two by means of beam splitters. This is used in case of extended sources. The familiar examples for the same being the Mach-Zehnder and the Michelson's interferometers.

In our experiment, the latter case, involving the division of amplitude in the Mach-Zehnder and Michelson's interferometric geometries has been used. In the following subsection, the phenomenon of superposition of two monochromatic waves forming an interference pattern has been derived mathematically.

2.2.2 Interference of two Monochromatic Waves

For a monochromatic wave, the electric field vector $\mathbf{E}$ is given as,

$$\mathbf{E}(\mathbf{r},t) = Re\left(\mathbf{A}(\mathbf{r})e^{-i\omega t}\right) = \frac{1}{2}\left[\mathbf{A}(\mathbf{r})e^{-i\omega t} + \mathbf{A}^*(\mathbf{r})e^{i\omega t}\right] \tag{2.1}$$

Where, $\mathbf{A}$ is the complex vector having Cartesian coordinate representation,

$$A_x = a_1(\mathbf{r})e^{ig_1(\mathbf{r})}, \qquad A_y = a_2(\mathbf{r})e^{ig_2(\mathbf{r})}, \qquad A_z = a_3(\mathbf{r})e^{ig_3(\mathbf{r})} \tag{2.2}$$

In Eqn. (2.2), a_j and g_j (j= 1, 2, 3) are real. From Eqn. (2.1) one can write $\mathbf{E}^2$ as:

$$\begin{aligned}
\mathbf{E}^2 &= \frac{1}{2}\left[\mathbf{A}(\mathbf{r})e^{-i\omega t} + \mathbf{A}^*(\mathbf{r})e^{i\omega t}\right].\frac{1}{2}\left[\mathbf{A}(\mathbf{r})e^{-i\omega t} + \mathbf{A}^*(\mathbf{r})e^{i\omega t}\right] \\
&= \frac{1}{4}\left[\mathbf{A}(\mathbf{r})^2e^{-2i\omega t} + \mathbf{A}^*(\mathbf{r})^2e^{2i\omega t} + 2\mathbf{A}(\mathbf{r}).\mathbf{A}^*(\mathbf{r})\right] \\
&= \frac{1}{4}\left[\left(A_x^2 + A_y^2 + A_z^2\right)e^{-2i\omega t} + \left(A_x^{*^2} + A_y^{*^2} + A_z^{*^2}\right)e^{2i\omega t} + 2\mathbf{A}(\mathbf{r}).\mathbf{A}^*(\mathbf{r})\right] \\
&= \frac{1}{4}[\left(a_1^2e^{2ig_1} + a_2^2e^{2ig_2} + a_3^2e^{2ig_3}\right)e^{-2i\omega t} + \left(a_1^2e^{-2ig_1} + a_2^2e^{-2ig_2} + a_3^2e^{-2ig_3}\right)e^{2i\omega t} \\
&+ 2\mathbf{A}(\mathbf{r}).\mathbf{A}^*(\mathbf{r})] \\
&= \frac{1}{4}[a_1^2\left(e^{2i(g_1-\omega t)} + e^{-2i(g_1-\omega t)}\right) + a_2^2\left(e^{2i(g_2-\omega t)} + e^{-2i(g_2-\omega t)}\right) + \\
&a_3^2\left(e^{2i(g_3-\omega t)} + e^{-2i(g_3-\omega t)}\right) + 2\mathbf{A}(\mathbf{r}).\mathbf{A}^*(\mathbf{r})] \\
&= \frac{1}{2}\left[a_1^2\left(cos(g_1-\omega t)\right) + a_2^2\left(cos(g_2-\omega t)\right) + a_3^2\left(cos(g_3-\omega t)\right) + \mathbf{A}(\mathbf{r}).\mathbf{A}^*(\mathbf{r})\right]
\end{aligned} \tag{2.3}$$

The average of $\mathbf{E}^2$ over a time period much greater than $T = \frac{2\pi}{\omega}$ is written as:

$$\begin{aligned}
\langle\mathbf{E}^2\rangle &= \langle\frac{1}{2}\left[a_1^2\left(cos(g_1-\omega t)\right) + a_2^2\left(cos(g_2-\omega t)\right) + a_3^2\left(cos(g_3-\omega t)\right) + \mathbf{A}(\mathbf{r}).\mathbf{A}^*(\mathbf{r})\right]\rangle \\
&= \frac{1}{2}\left[a_1^2\langle\left(cos(g_1-\omega t)\right)\rangle + a_2^2\langle\left(cos(g_2-\omega t)\right)\rangle + a_3^2\langle\left(cos(g_3-\omega t)\right)\rangle + \langle\mathbf{A}(\mathbf{r}).\mathbf{A}^*(\mathbf{r})\rangle\right] \\
&= \frac{1}{2}\langle\mathbf{A}(\mathbf{r}).\mathbf{A}^*(\mathbf{r})\rangle = \frac{1}{2}\langle\left[|A_x|^2 + |A_y|^2 + |A_z|^2\right]\rangle \\
&= \frac{1}{2}\left[a_1^2 + a_2^2 + a_3^2\right]
\end{aligned} \tag{2.4}$$

Now, when the vector $\mathbf{E}$ is a superposition of two waves $\mathbf{E_1}$ and $\mathbf{E_2}$, then:

$$\mathbf{E}^2 = \left(\mathbf{E_1} + \mathbf{E_2}\right)^2 = \left(\mathbf{E_1}^2 + \mathbf{E_2}^2 + 2\mathbf{E_1}.\mathbf{E_2}\right) \tag{2.5}$$

In terms of intensity:

$$I = (I_1 + I_2 + J_{12}) \tag{2.6}$$

Where, I_1 and I_2 are understood as $\langle \mathbf{E_1}^2 \rangle$ and $\langle \mathbf{E_2}^2 \rangle$ respectively and the average $\langle \cdot \rangle$ is taken over a time interval which is much greater than the time period T. These two terms are nothing but the individual intensities of the two respective superimposing waves. Term $J_{12} = 2\langle \mathbf{E_1}.\mathbf{E_2} \rangle$ is the *interference term*.
The complex amplitudes of the two superimposing waves are:

$$\begin{aligned} A_x, A_y, A_z &= a_1 e^{ig_1},\ a_2 e^{ig_2},\ a_3 e^{ig_3} \\ B_x, B_y, B_z &= b_1 e^{ih_1},\ b_2 e^{ih_2},\ b_3 e^{ih_3} \end{aligned} \tag{2.7}$$

Now, in terms of $\mathbf{A}$ and $\mathbf{B}$,

$$\begin{aligned} \mathbf{E_1}.\mathbf{E_2} &= \frac{1}{2}\left[\mathbf{A}(\mathbf{r})e^{-i\omega t} + \mathbf{A}^*(\mathbf{r})e^{i\omega t}\right].\frac{1}{2}\left[\mathbf{B}(\mathbf{r})e^{-i\omega t} + \mathbf{B}^*(\mathbf{r})e^{i\omega t}\right] \\ &= \frac{1}{4}\left(\mathbf{A}.\mathbf{B}e^{-2i\omega t} + \mathbf{A}^*\mathbf{B}^*e^{2i\omega t} + \mathbf{A}.\mathbf{B}^* + \mathbf{A}^*.\mathbf{B}\right) \end{aligned} \tag{2.8}$$

Proceeding in a similar manner as was done for Eqn. (2.3),

$$\begin{aligned} J_{12} &= 2\langle \mathbf{E_1}.\mathbf{E_2} \rangle = \frac{1}{2}\left(\mathbf{A}.\mathbf{B}^* + \mathbf{A}^*.\mathbf{B}\right) \\ &= a_1 b_1 cos(g_1 - h_1) + a_2 b_2 cos(g_2 - h_2) + a_3 b_3 cos(g_3 - h_3) \end{aligned} \tag{2.9}$$

If the experimental arrangement is made such that the same phase difference is introduced in all the components, then:

$$g_1 - h_1 = g_2 - h_2 = g_3 - h_3 = \delta \tag{2.10}$$

Substituting Eqn. (2.10) in Eqn. (2.9),

$$J_{12} = 2\langle \mathbf{E_1}.\mathbf{E_2} \rangle = (a_1 b_1 + a_2 b_2 + a_3 b_3)\, cos\delta \tag{2.11}$$

As is clear from the above equation, the interference term depends on amplitudes of components of two superimposing waves and the phase difference them. The phase δ

depends on the path difference between two waves. This property can thus be manipulated to determine the phase adding properties of transparent transmissive objects.

In the next subsection, the basic principle and working of these two classical interferometers namely the Mach-Zehnder and the Michelson's interferometer (which are the familiar examples for interferometers based on division of amplitude) has been explained.

2.2.3 Two Beam Interference Based on Division of Amplitude

2.2.3.1 *(i) Mach-Zehnder Interferometer*

The diagram of a basic Mach-Zehnder interferometer has been shown in Figure 2.1. In this arrangement, a laser source is coupled with spatial filtering assembly (SFA), the purpose of which is to filter out the central lobe of Airy pattern formed in the far field as a result of diffraction from circular aperture at the laser source.

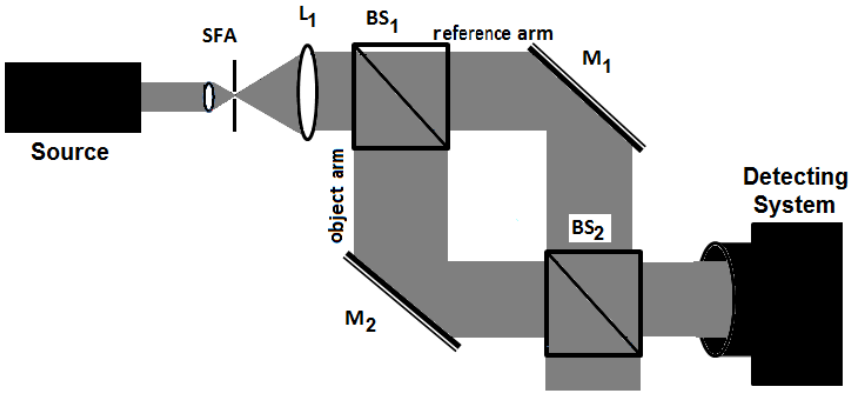

Figure 2.1: The Mach-Zehnder Interferometer

This is followed by a collimating lens L_1 of an appropriate focal length. The front focal plane of L_1 is adjusted such that it lies at the pinhole of spatial filtering assembly, thus giving a collimated beam. This beam now splits up at the beam splitter BS_1 into two equal intensity beams, one is transmitted out of the beam splitter and another is reflected from its surface. These beams propagate at an angle of 90° with respect to each other. The beam going in line with the propagation direction of the unsplitted beam is labeled, the reference beam, and the corresponding arm of the interferometric set up, the reference arm. Similarly, the beam propagating perpendicular to the unsplitted beam is

labeled the object beam and the corresponding interferometric arm, the object arm.

The mirrors, M_1 and M_2 are both placed at equal distance with respect to the beam-splitter BS_1 so as to make the path length traveled by both the object and reference beams approximately equal. The object and reference beams, after traveling through their respective paths combine at the beam splitter BS_2 and form an interference fringe pattern, which can be seen at any of beam splitter end. The fringes formed are circular, when the mirrors M_1 and M_2 are parallel. These can be made convex inwards or outwards or approximately straight parallel by suitably adjusting the mirror tilts.

2.2.3.2 *(ii) Michelson's Interferometer*

In Michelson's interferometer Figure 2.2, in a similar manner, a spatial filtering assembly (SFA) and a collimating lens (L_1) render the incoming laser beam parallel, after which it is split by a beam splitter BS_1 into two mutually perpendicular plane propagating beams.

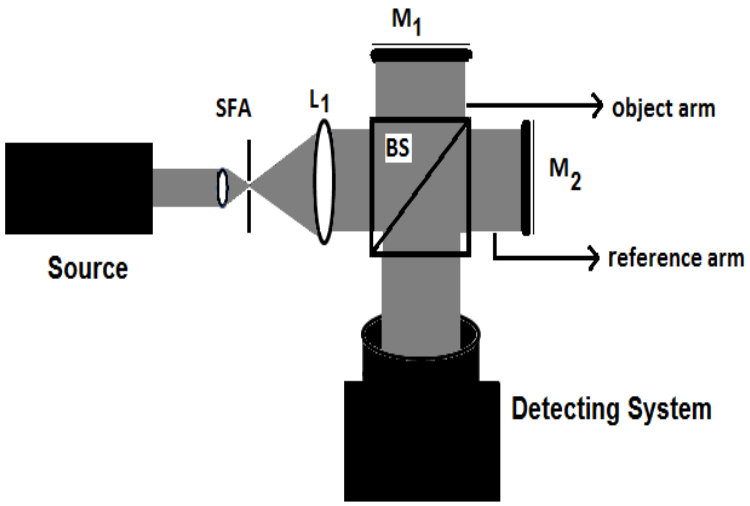

Figure 2.2: The Michelson's Interferometer

The beam propagating parallel to the direction of propagation of the unsplitted beam is labeled the reference beam and the corresponding arm, the reference arm and the beam propagating perpendicular to the unsplitted beam is labeled the object beam and the corresponding arm, the object arm. Both these beams combine at the beam splitter BS_1 after respective reflections from mirrors M_2 and M_1. The fringes thus formed are circular when M_1 is parallel to the virtual image of M_2. The mirror tilts can be adjusted

accordingly to get desirable fringes.

It should be noted that though both the above interferometric geometries are similar in the sense of mechanism of obtaining the interference fringes (i.e. division of amplitude), they differ in their geometries. In Michelson's interferometer, on account of back reflection from the mirrors M_1 and M_2, both the object and reference beams travel in their respective arms twice, retracing their paths, before combining again at the source beam splitter. This should be contrasted with the Mach-Zehnder geometry, in which the object and reference beams split up and combine at a separate beam splitters and do not retrace their path. Thus, one can refer to the Mach-Zehnder geometry as *single passage* and Michelson's geometry as *double passage* geometry. In both these interferometric arrangements, when an unknown transmissive medium is inserted as object in one of their arms, an additional phase is added to the object beam once in Mach-Zehnder and twice in Michelson's interferometer. This added phase can be extracted from the acquired fringe pattern images.

In the next part, slight modifications to the above said geometries have been explained. This involves adding a $4f$ imaging system, to image the object wave-field appearing right after the inserted object directly into the imaging system.

2.2.3.3 *(iii) Modified Interferometers by Inclusion of the 4f Imaging Systems*

A $4f$ imaging system uses the Fourier transforming property of a lens and gives an exact image of the object field distribution (Figure. 2.3).

When an object is placed at the first focal plane of a converging lens, its Fourier transform or the Fraunhoffer diffraction pattern appears at the back focal plane of the lens. This pattern can act as object for another convex or converging lens, when its focal plane coincides with the back focal plane of the first lens (and hence the pattern), the second lens further acts as a Fourier transformer (to the pattern appearing at the back focal plane of the first lens) and the Fourier transform of the said pattern can be seen at its back focal plane. This final Fourier transform is nothing but the original object field distribution. Therefore, in order to retrieve the exact object field distribution, from a $4f$ imaging system, one needs to place the object-in-question at the front focal plane and the detecting system at the back focal plane of this system.

The scheme of a $4f$ imaging system has been shown in Figure 2.3. The object to

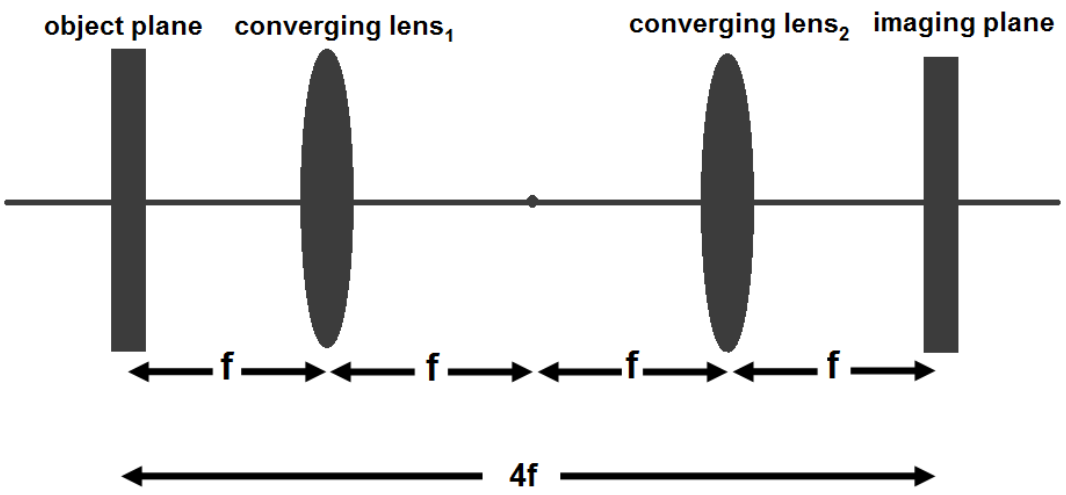

Figure 2.3: 4f Imaging System

be imaged is kept at the object plane which is at a distance f (i.e. focal length of converging lens 1 and 2) with respect to the first converging lens. The image is captured at the imaging plane which is at the back focal plane of the second converging lens. The two lenses are $2f$ distance apart.

The interferometric arrangement which is being used for calculating the phase adding properties of an unknown transmissive medium, can be modified by the insertion of a $4f$ imaging system, placed strategically such that its first focal plane coincides with the exit plane of the object (when present) and the detecting system with the second focal plane (Figure 2.4 (a) and (b)).

The system thus formed is then capable of measuring the phase added to the propagating beam at the exit plane of the object-in-question rather than after some propagation in free space behind it. This method of including a $4f$ imaging system in the interferometric geometry is advantageous in the sense that, since the beam traversing through the object is captured right at its exit plane, there is no inclusion of any other effects because of its propagation through another medium (i.e. free space). In other words, the phase added purely due to a propagation inside the object can be computed. Thus, while analyzing phase added to the propagating beam due to the said object, one can achieve results which are purely for wave propagation through the object.

The modified schemes of Mach-Zehnder and Michelson's interferometers have been shown in Figure 2.4(a) and (b) (with the insertion of $4f$ imaging system) respectively. The object is inserted at the indicated places.

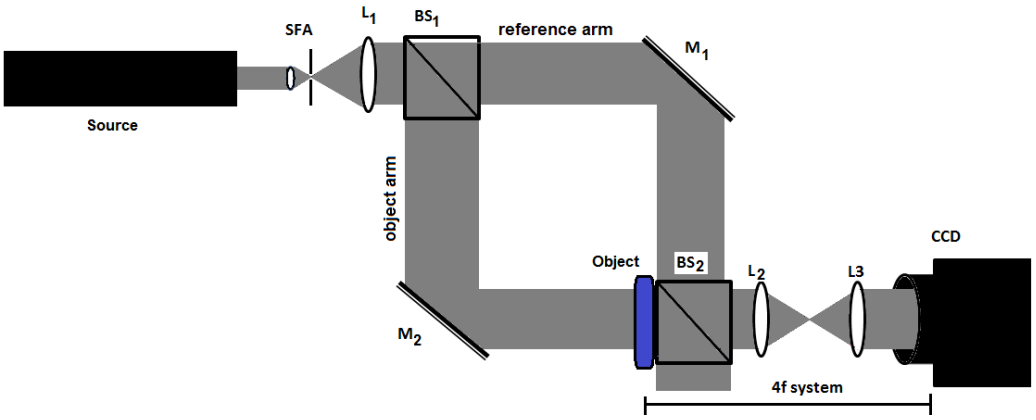

(a)

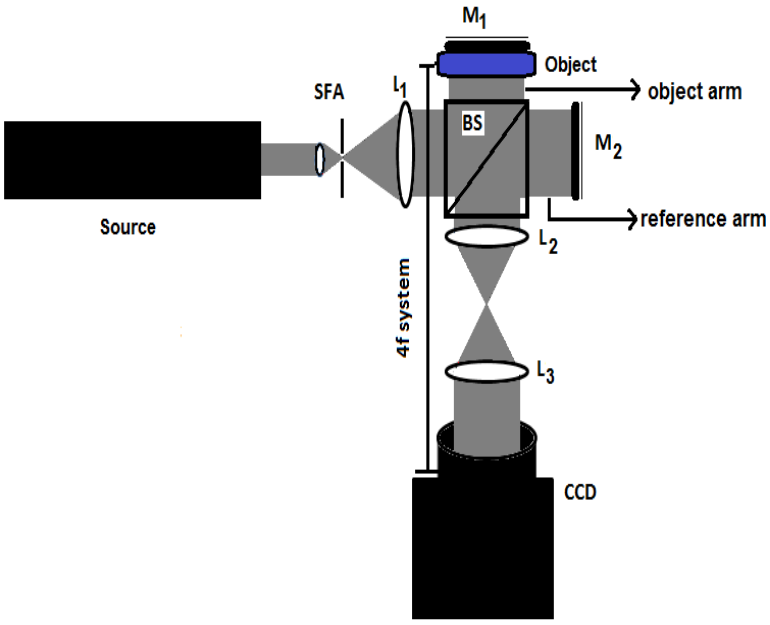

(b)

Figure 2.4: Modified Mach-Zehnder (a) and Michelson's (b) Interferometers

Since the basic aim of the work requires to retrieve the additional phase added to a 633 nm wavelength on its propagation through the PRPPs, both the modified geometries of the Mach-Zehnder and Michelson's interferometers are considered for the purpose. The said PRPPs have been manufactured in such a fashion that they have the capacity of introducing a random phase to a beam propagating through them without affecting its amplitude. The PRPPs' composition has been explained in detail in the following section.

2.2.4 Details of Pseudo-Random-Phase-Plates

The mentioned phase plates (referred to as $PRPP_1$ and $PRPP_2$) along with their controlling systems have been bought from Lexitek motors *Mantravadi et al. (2004)*. These have been designed and tested for providing atmospheric turbulence like conditions to a propagating beam at 1550 nm wavelength. The phase plates apparently are packed, static, circular and transparent media having annular regions. They are approximately 10 mm thick (refer Figure 2.5).

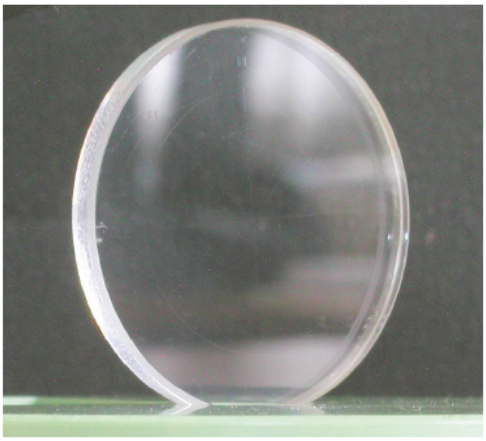

Figure 2.5: Photograph of a Pseudo-Random-Phase-Plate

Inside, these have been designed using optical glass, acrylic, and a unique near-index-matching polymer that gives them a stable mechanical structure. As can be seen in Figure 2.6, they are composed of 5 layers : 2 outer optical windows of BK7 glass, 2 inner layers of near-index-matching polymer, and 1 layer of acrylic with the desired turbulence profile written on one side.

In order to manufacture such a configuration, the acrylic layer is first machined with the turbulence onto one surface. A layer of polymer is then placed onto each side of the acrylic resulting in a near-index matching sandwich. Next, the plate is sealed with optical window glass which holds the entire package together in a mechanically stable configuration. The BK7 glass is then coated with an anti-reflective coating. The arrangement of layers is seen to be mechanically symmetric so that environmental factors such as stress due to thermal expansion are less likely to cause the PRPPs to separate into their individual layers. Owing to their design, the PRPPs are mechanically robust enough to be mounted easily without deformation. The PRPPs' design was developed at the Starfire Optical Range, and they were manufactured by Lexitek corpo-

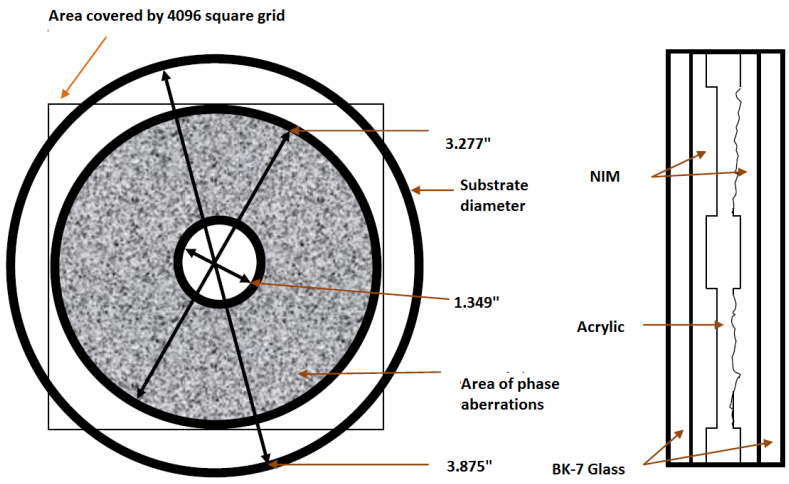

Figure 2.6: A Pseudo-Random-Phase-Plate (PRPP)

ration *Mantravadi et al. (2004)*. These PRPPs have been imprinted with Kolmogorov turbulence, with a known Fried's parameter. This was done by generating phase screens using standard Fourier transform techniques filtered with a Kolmogorov spectrum. Each phase screen had 4096 sample phase points across a side. The turbulence was written on a 3.28" diameter acrylic annulus, with a 1.35" diameter obscuration, resulting in approximately 20μ m sample spacing (Figure 2.6). Before machining the phase profile into the acrylic, two modes of tilt were removed to help with fabrication tolerances. The two PRPPs, differ in the sense of Fried's coherence length for a particular wavelength. Once mounted on specially designed high speed rotary stage, the PRPPs can be controlled and rotated with speeds ranging from 0.15625 rpm to 2470.2 rpm. The photograph of the PRPP mount (which is connected to stepper motor controller for rotation) has been shown in Figure 2.7.

The varying refractive index profile in a PRPP lies only in the middle of the annular region and the whole phase plate is divided into 4096 sample phase points Figure 2.6. The diameters of various regions have been indicated in Figure 2.6 and a section showing layers involved in the manufacture of a phase plate has been shown towards the right in the same figure.

These specially designed phase plates are used as objects in the modified Mach-Zehnder and Michelson's interferometers and the additional phase added by them to the propagating 633 nm laser beam is retrieved. The following sections explain the

Figure 2.7: Photograph of a PRPP Mount

experimental algorithm for the same.

2.3 Experimental Procedure and Theory

The interference pattern in a modified interferometer (i.e. inserted with a $4f$ imaging system) can be recorded in the following two situations :

1. When the unknown medium (here, PRPP) has not been inserted.

2. When the unknown medium has been inserted in the object arm.

In situation 1, straight line fringes tilted with respect to the horizontal axis at an angle of about 45° (obtained by suitably tilting mirrors M_1 and M_2) are captured. In situation 2, the fringes seen in situation 1 shift or get distorted in accordance with the properties of the medium in question (PRPP). This additional phase introduced due to the medium can be retrieved and analysed by subtracting the phase retrieved from fringes in situation 1 from those retrieved in situation 2. This is done with the intention of understanding the behavior of two PRPPs i.e. PRPP_1 and PRPP_2 (available in the laboratory) at a wavelength of 633 nm using a low power ($12\,\mathrm{mW}$) He-Ne laser.

Both the interferometric geometries for the modified Mach-Zehnder and the Michelson's interferometer are used for retrieving the phase added due to these phase plates to a 633 nm wavelength laser beam. These phases are subsequently analysed by calculating the phase structure function.

As has been previously discussed, in Mach-Zehnder interferometer, the object beam traverses through the unknown medium kept in the object arm *only once* before combining with the reference beam at the second beam splitter to form the fringe pattern. Thus, the object beam experiences only a single passage through the medium under consideration (i.e. here, PRPP_1 or PRPP_2). On the other hand, in case of Michelson's interferometer, the object beam passes through the medium *twice*, thereby experiencing a double passage through the medium. Therefore, eventually a total of four different cases are to be dealt with :

1. PRPP_1 inserted as object in the object arm of the Mach-Zehnder interferometer.
2. PRPP_2 inserted as object in the object arm of the Mach-Zehnder interferometer.
3. PRPP_1 inserted as object in the object arm of the Michelson's interferometer.
4. PRPP_2 inserted as object in the object arm of the Michelson's interferometer.

Figure 2.8 illustrates modified interferometric schemes used in the laboratory for the present experimental purposes.

Here, in both (a) and (b), SFA is the spatial filtering assembly, ND is the neutral density filter, BS_1 and BS_2 are 50-50 beam splitters, M_1 and M_2 are the reflecting mirrors, L_1 is $f = 10\,\text{cm}$ collimating lens, L_2 and L_3 are convex lenses with focal length $f = 25\,\text{cm}$ each, PRPP is one single Pseudo-Random-Phase-Plate (either of PRPP_1 or PRPP_2), and CCD is the charge coupled device. In Figure 2.8 (a), the interferometric geometry has been shown for the experimental step in which one PRPP (any of PRPP_1 or PRPP_2) has been inserted in the object arm of the Mach Zehnder interferometer. Similarly, Figure 2.8 (b) shows the experimental step in which one PRPP (any of PRPP_1 or PRPP_2) is inserted in the object arm of the Michelson's interferometer. The readings for the step in which any PRPP is not inserted are taken by just omitting the PRPP from the indicated position in both the shown cases.

In Mach-Zehnder set up, as can be seen in Figure 2.8 (a), a $4f$ imaging system is inserted after the beam splitter BS_2 such that the object to be analysed can be placed at the first focal plane of lens L_2 and the imaging system (i.e. the CCD) at the second focal plane of lens L_3. The reference beam on reflection from mirror M_1 reaches the beam splitter BS_2 and combines with the object beam. The fringe pattern formed due to the superposition of 1) wave field appearing at the second focal plane of lens L_3

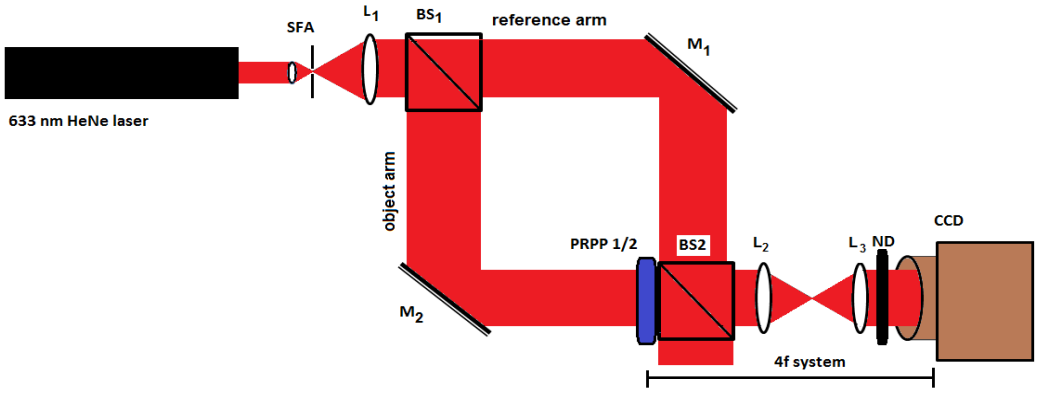

(a)

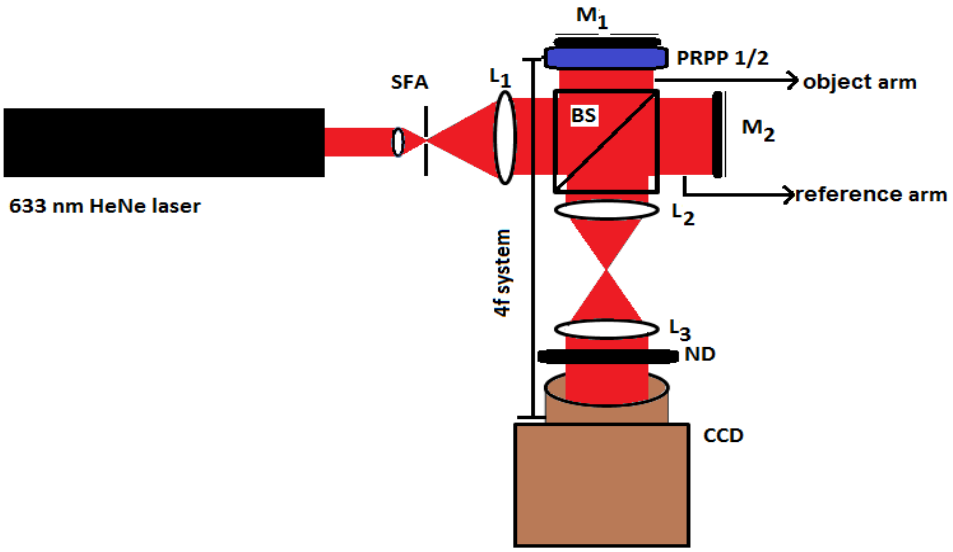

(b)

Figure 2.8: Mach-Zehnder and Michelson's Schemes used in Laboratory

(which is same as the one transmitted just out of the object) and 2) reference beam, is captured by the CCD at the second focal plane of lens L_3. Thus, in this geometry, the random phase added solely due to the object is isolated by capturing fringes in two situations, 1) without the object, 2) with the object inserted at the specified location and subtracting the phase retrieved in situation 1) i.e. when no object has been inserted from that retrieved in 2), when the object is inserted.

In Michelson's interferometer (Figure 2.8 (b)), again, a $4f$ imaging system is inserted in the object arm and the images are captured using a CCD carefully placed at the second focal plane of lens L_3. In this interferometric geometry the object ($PRPP_1$ or $PRPP_2$) is placed very close to the mirror M_1, so that the distance between the object and

mirror is negligible, hence ensuring that the beam after traversing through the PRPP (1 or 2), suffers almost a negligible propagation through free space, before getting reflected from the mirror M_1 again into the PRPP. Here also, the wavefront appearing right after the object is captured into the CCD using the same $4f$ system as was done in the Mach-Zehnder arrangement (Figure 2.8 (a)) The random phase added solely due to the object is isolated by capturing the fringes in the same two situations, i.e., 1) without the object, 2) with the object inserted at the specified location and subtracting the phase retrieved in 1) from that in 2).

The CCD used in both the experiments is a 640×480 camera having pixel size $9.9 \times 9.9\,\mu m^2$ and a frame capturing speed of 51.9 frames per second. During the experiments, the PRPPs are always rotated with the same velocity so that the object beam sees different portions of the phase plates, but the rotation speed is kept such that for all practical purposes, the camera always captures a static phase plate scenario. In the next section, the theory and the steps involved in phase retrieval from the fringe pattern images has been explained.

2.3.1 Phase Retrieval

The spatial frequency of a captured fringe pattern is always kept high, so that while analyzing the fringe pattern images, the interference term (Eqn. (2.11)) can be easily isolated from the dc term (i.e. first two terms in Eqn. (2.8)) by high pass filtering in the Fourier domain. It should be noted that in Eqn. (2.8), the first two terms represent the intensities of the two interfering beams. These have been rendered uniform owing to collimation and hence the summation of these two gives a uniform background intensity (or dc) to the fringe images. The sinusoidal interference term can thus be isolated by Fourier High pass filtering of the fringe pattern image. Since this isolated signal now is real, one can form a complex analytic signal out of this given real signal by suppressing the negative spatial frequencies in its Fourier domain and inverse Fourier transforming the remaining signal. The angle of the finally obtained complex signal $\left(\text{i.e. } \tan^{-1}\left(\frac{\text{Imaginary part of the obtained complex signal}}{\text{Real part of the obtained complex signal}}\right)\right)$ gives the phase δ.

2.3.1.1 *Phase Retrieval Steps using MATLAB Code*

As has been discussed above, the obtained fringe pattern images are analysed one-by-one by realizing the following steps *Ikeda et al. (2005)* using a MATLAB program.

1. A captured fringe image matrix is converted to a gray scale matrix, retaining only the intensity information (Figure 2.9)

2. This gray scale matrix is first resized from 640×480 to 480×480 and then is padded with zeros equally on all four sides, so that the matrix size now increases to a size, 960×960 and the corresponding image looks like an image embedded in a black background. The padding with zeros is done to increase the spatial resolution. This new image matrix is denoted as $I_{padded}(i, j)$, where i and j are the row and column indices respectively of this matrix and both go from 1 to 960.

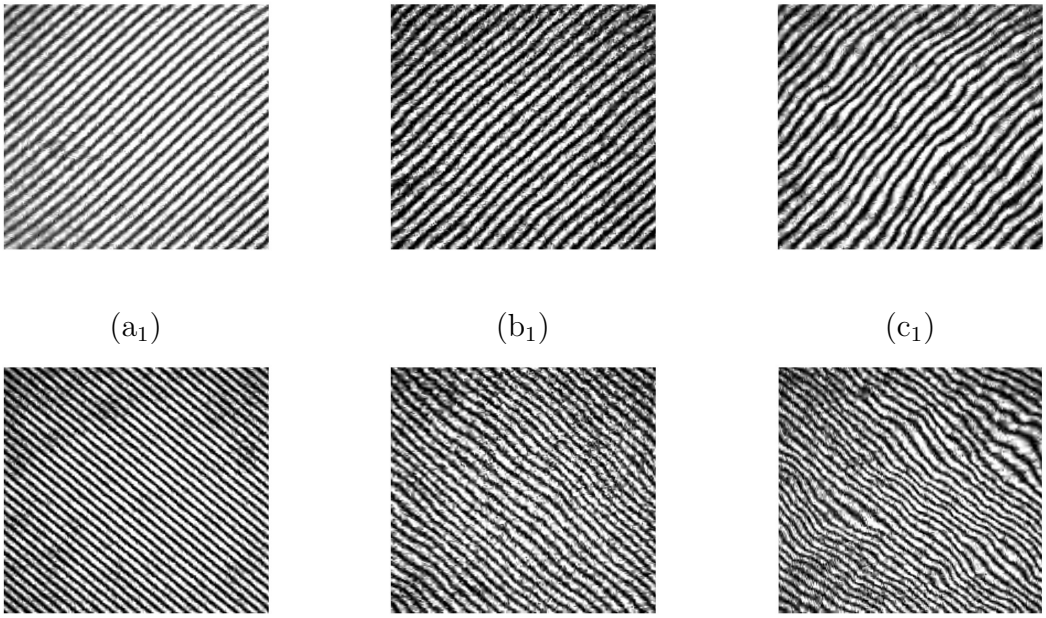

Figure 2.9: Row 1: (a_1), (b_1) and (c_1) respectively show captured images of the undistorted fringes, fringes when $PRPP_1$ is inserted and fringes when $PRPP_2$ is inserted in Mach-Zehnder interferometer. Row 2: (a_2), (b_2) and (c_2) now show captured images of the undistorted fringes, fringes when $PRPP_1$ is inserted and fringes when $PRPP_2$ is inserted (respectively) in Michelson's interferometer.

The figures above (in Figure 2.9) show the captured (resized and gray-scaled)

images when $PRPP_1$ and $PRPP_2$ are inserted as objects in the Mach-Zehnder and Michelson's interferometric geometries respectively. The first row images, i.e. (a_1), (b_1) and (c_1) respectively show the undistorted fringes (i.e. fringes without the insertion of any phase plate), the distorted fringes due to insertion of $PRPP_1$ as object and the distorted fringes due to insertion of $PRPP_2$ as object in Mach-Zehnder (single passage) interferometer. The second row (i.e. (a_2), (b_2) and (c_2)) shows the fringes in a similar sequence but with the respective insertions in Michelson's interferometer.

3. $I_{padded}(i,j)$ is now Fourier transformed using the MATLAB command *fft2* and the Fourier transform of $I_{padded}(i,j)$ is called $I_{fourier}(i,j)$. It should be noted that $I_{fourier}(i,j)$ is also of the size 960×960.

4. $I_{fourier}(i,j)$ is now centered using the MATLAB command *fftshift*. This command swaps the first quadrant with the fourth quadrant and second quadrant with the third quadrant.

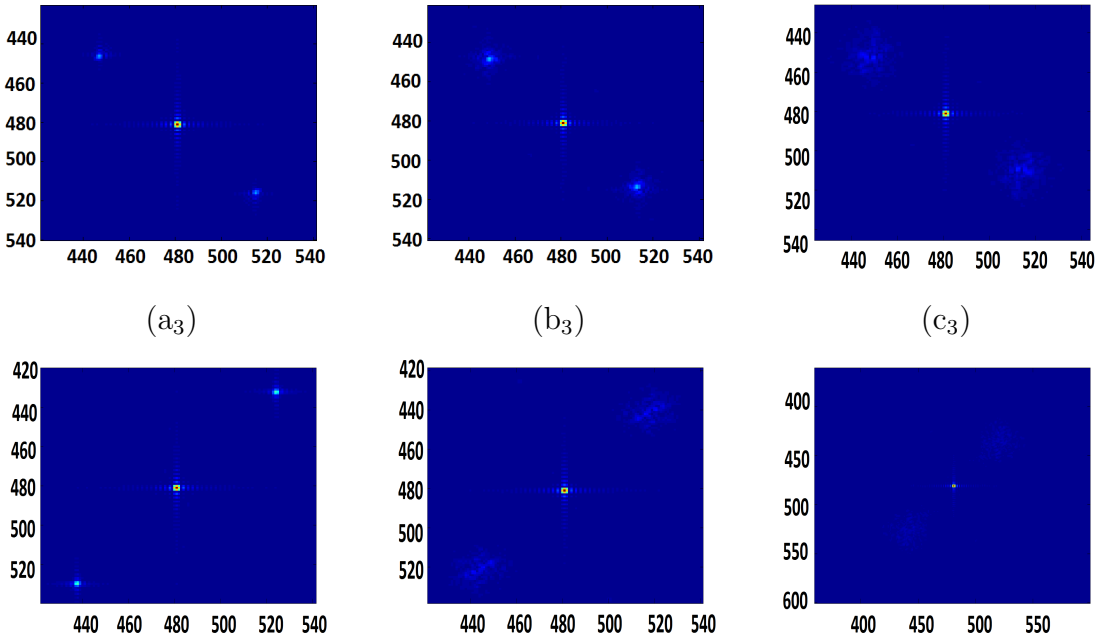

(a_3) (b_3) (c_3)

(a_4) (b_4) (c_4)

Figure 2.10: The above zoomed in images show the (fftshifted) Fourier domain representations of the images shown in Figure 2.9 in the same order.

The new centered matrix is called, $I_{fftshift}(i,j)$ (Figure. 2.10). Due to *centering* by *fftshift*, in the matrix $I_{fftshift}(i,j)$, the whole dc term comes to the center i.e.

at the pixel position $i = 480, j = 480$ and the side frequency bands can also be easily located. In this matrix, the frequencies to the left of the column $j = 480$ are the negative spatial frequencies and those towards its right are the positive ones.

Figures in 2.10 show the centered (zoomed in) Fourier transforms of the captured images. (a_3), (b_3) and (c_3) respectively show the centered Fourier transforms of the undistorted fringes (i.e. fringes without the insertion of any phase plate), the distorted fringes due to insertion of PRPP_1 as object and the distorted fringes due to insertion of PRPP_2 as object in Mach-Zehnder (single passage) interferometer. The second row (i.e. (a_4), (b_4) and (c_4)) similarly shows the centered Fourier transforms with the insertions in Michelson's interferometer in the same sequence as the first row.

5. The Butterworth High pass filter matrix $H(i, j)$, which is defined as:

$$H(i,j) = \frac{1}{(1 + (\frac{r_0}{r(i,j)})^{2n})} \tag{2.12}$$

with $r_0 = 40$, $n = 1$ and $r^2(i, j) = (i - 480)^2 + (j - 480)^2$, the radial distance corresponding to each $(i, j)^{th}$ location in the matrix, with respect to $i = 480, j = 480$ is now computed.

6. This, $H(i, j)$ is point-wise multiplied with $I_{fftshift}(i, j)$, thus filtering out the dc term and the lower spatial frequencies from the $I_{fftshift}(i, j)$. With the removal of the dc term, one is only left with the desired sinusoidal phase term. The Butterworth High pass filtered $I_{fftshift}(i, j)$ is now referred to as $I_{filter}(i, j)$. This has been shown in Figure 2.11, where, the centered Fourier transforms shown in Figures 2.10 have been filtered using the Butterworth High pass filter.

7. From $I_{filter}(i, j)$, the negative spatial frequencies are removed, by assigning a zero value to all the matrix entries before $j = 480$. The new matrix is now named as $I_{filterpositive}(i, j)$.

8. This $I_{filterpositive}(i, j)$ is now again *decentered* using *fftshift* in MATLAB and the 480×480 quadrant containing the side band with higher spatial frequencies is retained as a new matrix $I_{fftfinal}(i, j)$ with i and j now going from 1 to 480.

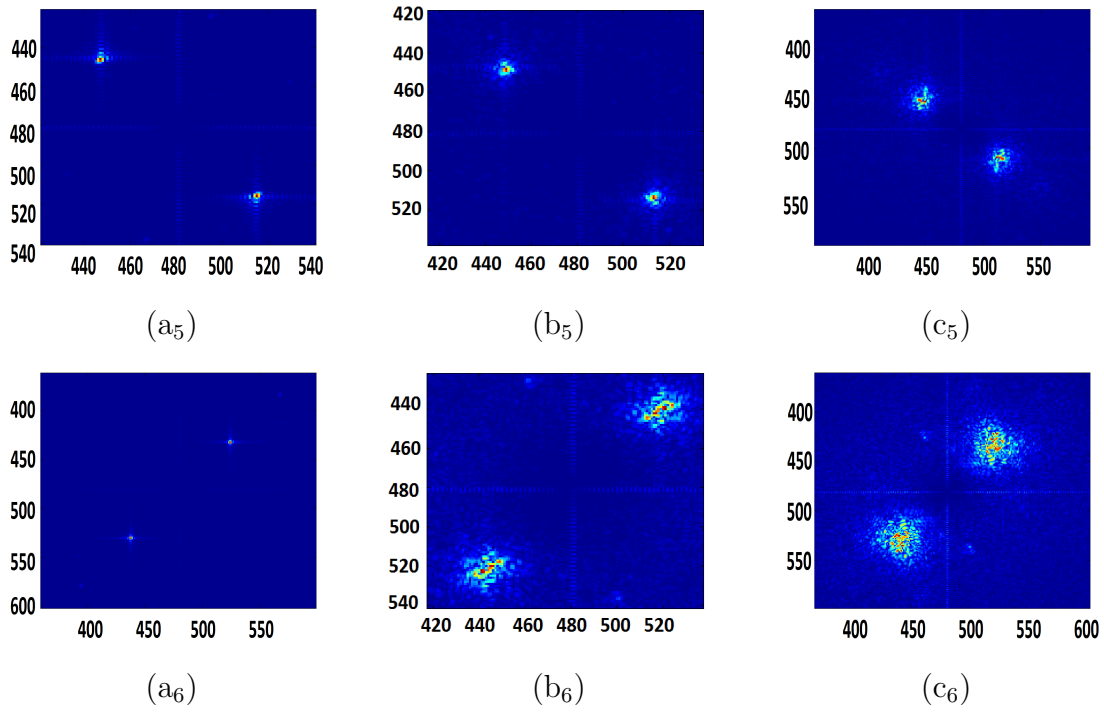

Figure 2.11: The Fourier domain images shown in Figure 2.10 are now filtered using Butterworth high pass filter and the resultant images have been shown above in the same order as previous.

Figure 2.12 shows the finally selected, zoomed in portions of $I_{fftfinal}(i,j)$ for each of the said case, in the usual sequence.

9. The inverse Fourier transform of $I_{fftfinal}(i,j)$ is the required complex analytic signal *Ikeda et al. (2005)* and is named as $I_{final}(i,j)$. It is of size 480×480.

10. Finally, tangent-inverse of the ratio of imaginary part by the real part of every entry in $I_{final}(i,j)$ gives the required phase angle for each matrix entry and hence the initial image. The resultant is the phase angle matrix denoted as $\Phi(i,j)$.

11. Since, the phase extracted from an image, $\Phi(i,j)$ is in a highly wrapped form, the MATLAB command *unwrap* is used on the matrix $\Phi(i,j)$ to unwrap it.

Using the above algorithm, the phase matrix $\Phi(i,j)$ is extracted out of the retrieved fringe pattern images for all cases (i.e. insertion of $PRPP_1$/$PRPP_2$ as object) in both *single* and *double* passage interferometric geometries. Also, in both the said geometries, the phase matrix when no object is inserted in the object arm (using the same algorithm as above) is extracted and is called $\Phi_{directmach}(i,j)$ for the phase extracted

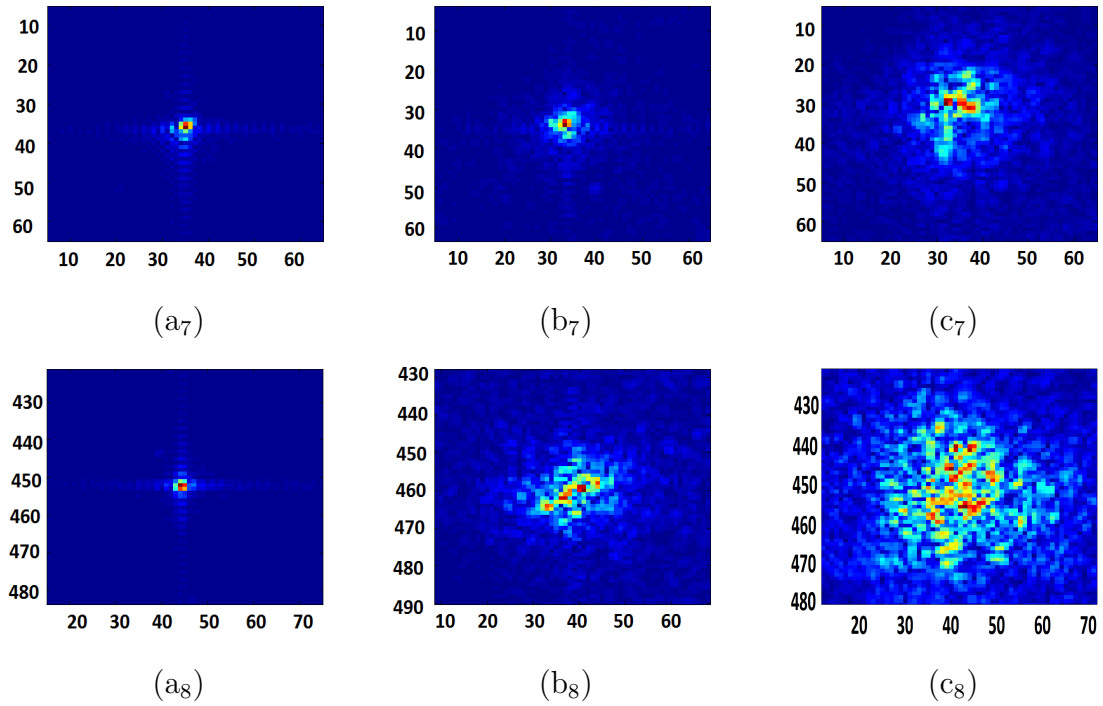

Figure 2.12: Here, the finally selected, zoomed in portions of $I_{fftfinal}(i,j)$ (i.e. the finally selected portion in Fourier domain of an image) for each of the said case, in the usual sequence have been shown.

in Mach-Zehnder interferometric geometry (*single passage*) and $\Phi_{directmich}(i,j)$ for the corresponding phase in Michelson's geometry (*double passage*).

Now, to retrieve the phase added to the beam just because of the inserted object for all cases, in both the geometries, $\Phi_{directmach}(i,j)$ is point-wise subtracted from $\Phi(i,j)$ extracted for object insertions in Mach-Zehnder geometry and similarly $\Phi_{directmich}(i,j)$ is point-wise subtracted from $\Phi(i,j)$, extracted for object insertions in Michelson's geometry. This gives the desirable phase introduced into the beam due to its passage just through $PRPP_1$/$PRPP_2$. Only 55×55 sized faithfully unwrapped matrix could be retrieved in this manner, since the removal of all phase discontinuities could only be done within this sized portion for all cases (Figure 2.13).

In (a_9) and (a_{10}) in Figure 2.13, the phase unwrapped portions extracted for the undistorted fringe pattern images (with no object inserted) in Mach-Zehnder ($\Phi_{directmach}(i,j)$) and Michelson's interferometers ($\Phi_{directmich}(i,j)$) respectively have been shown. These are further subtracted point wise from the phase unwrapped portions retrieved when any of $PRPP_1$ or $PRPP_2$ is inserted in the mentioned interferometers. (b_9) shows one such 55×55 phase unwrapped portion when $PRPP_1$ is inserted as object in the Mach-Zehnder

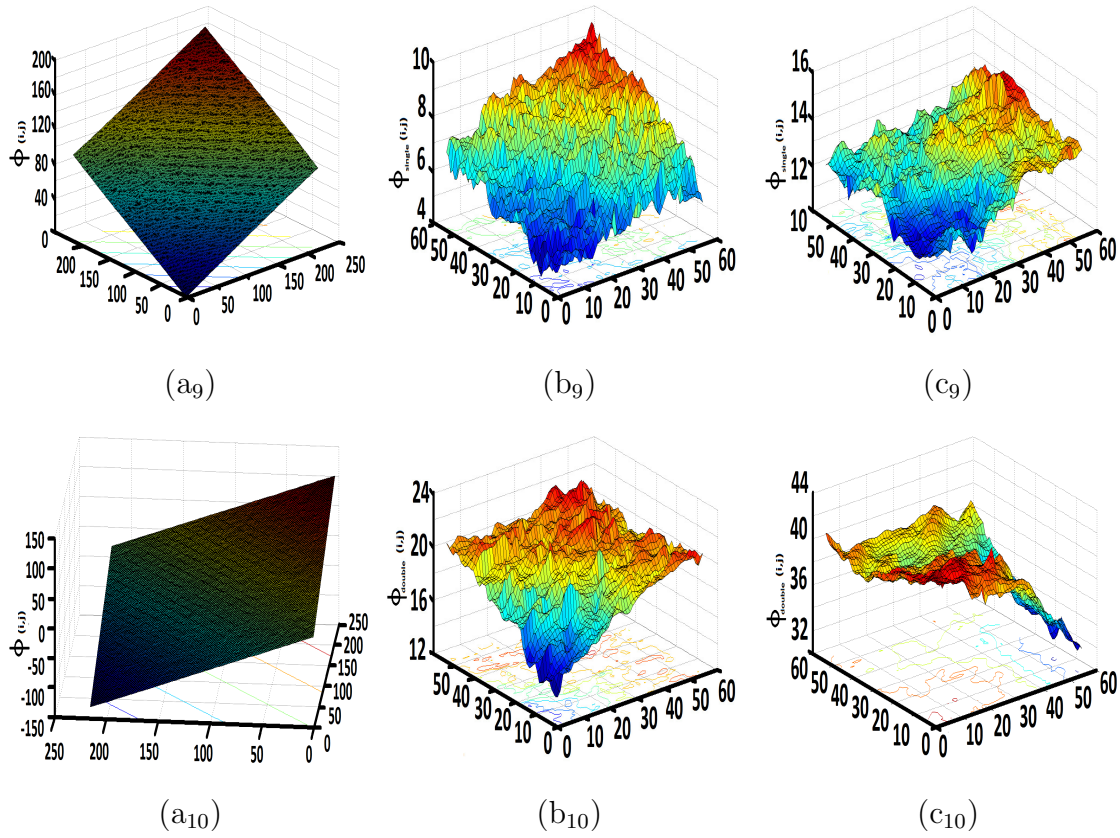

(a_9) (b_9) (c_9)

(a_{10}) (b_{10}) (c_{10})

Figure 2.13: In the above, the phase unwrapped portions extracted from fringe pattern images (shown in the sequence of figures from (Figure 2.9 to Figure 2.12) have been presented in similar sequence.

interferometer. (c_9) on the other hand shows another 55×55 phase unwrapped portion when $PRPP_2$ is inserted as object in the Mach-Zehnder interferometer. Similarly, (b_{10}) and (c_{10}) show the 55×55 phase unwrapped portions when $PRPP_1$ and $PRPP_2$ are respectively inserted in the Michelson's interferometer.

The steps given above are repeated for all the captured fringe pattern images in *single* (Mach-Zehnder interferometer) as well as *double passage* (Michelson's interferometer) cases to get the corresponding 55×55 retrieved phase matrix portions. Each entry of these retrieved matrices is indicative of the phase introduced in the beam due to its passage just through $PRPP_1$/$PRPP_2$.

In the next section, the analysis done on these retrieved phase matrices has been explained. This is required to decide about the nature (Kolmogorov/non-Kolmogorov) of the $PRPP_1$/$PRPP_2$ under consideration and pursue a further discussion on them.

2.3.2 Analysis, Results, and Discussion

2.3.2.1 *(i) Theoretical Background*

Let the retrieved single passage phase matrices be denoted as $\Phi_{\text{single}}(\text{i},\text{j})$ and the double passage phase matrices as $\Phi_{\text{double}}(\text{i},\text{j})$, where the pixel positions are the $(\text{i},\text{j})^{th}$ matrix entries owing to discretization of the detector area (CCD surface). The corresponding structure functions are calculated from $\Phi_{\text{single}}(\text{i},\text{j})$ and $\Phi_{\text{double}}(\text{i},\text{j})$ as follows:

$$D_{\Phi_{single}}(r) = \langle(\Phi_{single}(\text{i},\text{j}) - \Phi_{single}(\text{i}+\text{r},\text{j}))^2\rangle \tag{2.13}$$

$$D_{\Phi_{double}}(r) = \langle(\Phi_{double}(\text{i},\text{j}) - \Phi_{double}(\text{i}+\text{r},\text{j}))^2\rangle \tag{2.14}$$

where r varies from 1 to 54 in units of pixels. $\langle\cdot\rangle$ denotes the ensemble average which is taken for the given case (single or double passage) over all the considered phase portions.

The following are the relations between $D_\Phi(r)$ and r for the Kolmogorov and non-Kolmogorov behavior of the given transmission medium *Rao et al. (2000)*:

$$D_\Phi(r) = \begin{cases} \gamma_\beta \left(\frac{r}{\rho_0}\right)^{\beta-2} & 2<\beta<4 \\ -2^{\beta-2}\frac{\Gamma(\beta/2)}{\Gamma\left(\frac{2-\beta}{2}\right)}\gamma_\beta\left[\frac{K_0^{4-\beta}}{(\beta-2)(\beta-4)}\right]\frac{r^2}{\rho_0^{\beta-2}} & \beta>4 \end{cases} \tag{2.15}$$

Where, $\gamma_\beta = \frac{2^{\beta-1}\left[\Gamma\left(\frac{\beta+2}{2}\right)\right]^2\Gamma\left(\frac{\beta+4}{2}\right)}{\Gamma\left(\frac{\beta}{2}\right)\Gamma(\beta+1)}$ and $K_0 = \frac{2\pi}{L_0}$.

L_0 represents the turbulence outer scale.

In Eq. (2.15), β is the factor which determines the power law for r and has a value $\frac{11}{3}$ for the Kolmogorov case. γ_β is the consistency parameter that depends on β (for $\beta = \frac{11}{3}$, $\gamma_\beta \approx 6.88$). ρ_0 is the generalized coherence length, which is equal to Fried's coherence length r_0 for $\beta = \frac{11}{3}$. It can also be observed from Eqn. (2.15) that:

- For $2 < \beta < 4$, the slope of the plot between $\log_{10}(D_\Phi(r))$ and $\log_{10}(r)$ lies in $(0, 2)$ (for Kolmogorov case where, $\beta = \frac{11}{3}, \text{slope} = \beta - 2 = \frac{5}{3} \approx 1.67$) and,
- For $\beta > 4$, the slope is 2.

For the present case, the computed $D_{\Phi_{single}}(r)$ and $D_{\Phi_{double}}(r)$ are tested for the nature of their dependence on r. Using a separate MATLAB code, the phase structure

function is calculated using Eq. (2.13) and (2.14) from the collected samples (for single and double passage cases) and the slope for linear curve fits between $log_{10}(D_{\Phi_{single/double}}(r))$ and $log_{10}(r)$ are obtained for each case.

The characterization of the PRPPs as Kolmogorov/non-Kolmogorov turbulence simulators is done according to the values of the obtained slopes as has been outlined above.

2.3.2.2 *(ii) Tables, Plots, and Interpretations*

For the purpose of characterizing the PRPPs, an ensemble of 1200, 55×55 phase unwrapped portions is collected for every case defined in Section 2.3. Then, for each case, through a separate MATLAB code, an increasing number of phase unwrapped portions is randomly selected as an ensemble, out of the given total of 1200. Starting with an ensemble size of 200, the ensemble size is increased in steps of 200, until the maximum available size of 1200 is reached. Each process for random sample selection of a given size and the subsequent phase structure function calculation from it (for the determination of slope for linear fit between $log_{10}(D_{\Phi}(r))$ vs. $log_{10}(r)$) is repeated 10 times and finally the mean for all the 10 slopes is taken as the slope value corresponding to the ensemble size in question.

In this manner, the values of slopes for the linear fits between $log_{10}(D_{\Phi_{single}}(r))$ vs. $log_{10}(r)$ and $log_{10}(D_{\Phi_{double}}(r))$ vs. $log_{10}(r)$ obtained for a single passage in Mach-Zehnder interferometer and double passage in Michelson's interferometer respectively are calculated for all cases. Table 2.1 summarizes the results for the mean values of slopes for $log_{10}(D_{\Phi_{single}})$ vs. $log_{10}(r)$ calculated for 10 iterations each of an increasing number of randomly selected phase unwrapped portions from a total available 1200

Table 2.1: Single Passage: Slope calculation

No. of Randomly Selected Phase Unwrapped Portions	**Slope**	
	$PRPP_1$	**$PRPP_2$**
200	0.91 ± 0.35	1.24 ± 0.31
400	0.94 ± 0.35	1.24 ± 0.36
600	0.93 ± 0.31	1.24 ± 0.34
800	0.93 ± 0.35	1.24 ± 0.35
1000	0.93 ± 0.34	1.24 ± 0.34
1200	0.93 ± 0.34	1.24 ± 0.34

portions for single passage in Mach-Zehnder geometry.

Similarly, Table 2.2 shows the mean values of slopes for $log_{10}(D_{\Phi_{double}})$ vs. $log_{10}(r)$, again calculated for 10 iterations each of an increasing number of randomly selected phase unwrapped portions, for double passage in Michelson's interferometer geometry.

Table 2.2: Double Passage: Slope Calculation

No. of Randomly Selected Phase Unwrapped Portions	**Slope**	
	PRPP$_1$	**PRPP$_2$**
200	1.34 ± 0.27	1.64 ± 0.18
400	1.34 ± 0.26	1.64 ± 0.21
600	1.34 ± 0.28	1.64 ± 0.22
800	1.34 ± 0.29	1.64 ± 0.21
1000	1.34 ± 0.27	1.64 ± 0.21
1200	1.34 ± 0.28	1.64 ± 0.21

As is evident from these tables, the slope calculation is fairly robust and reproducible till the second decimal place, thus the slope values for the whole ensemble i.e. sample number 1200 are considered as final results for further analysis and interpretations. Figure 2.14 shows plots for the obtained results for all the cases discussed in Section 2.3.

Frame (a) and (b) show the linear curve fit plots between $log_{10}(D_{\Phi_{single}}(r))$ vs. $log_{10}(r)$ for cases with the insertion of PRPP$_1$ and PRPP$_2$ respectively in Mach Zehnder (or single passage) geometry (Eqn. 2.13) and frames (c) and (d) show the linear curve fits between $log_{10}(D_{\Phi_{double}}(r))$ vs. $log_{10}(r)$ for the same cases in Michelson's (or double passage) geometry (Eqn. 2.14). The averaging for the calculation of phase structure function has been done over a sample number of 1200 in all the cases.

The violet straight line in each case shows the linear curve for Kolmogorov's case, wherein the slope is $\frac{5}{3}$. It should be noted that for a realistic Kolmogorov turbulence, the violet straight line shown will have a finite intercept depending on Fried's coherence length (r_0) and will not pass from zero on the y axis. Here, the straight line has been drawn like this, just for a visual comparison. Also, error bars (calculated on the lines of APPENDIX A) for each point in all plots have been shown as green dots.

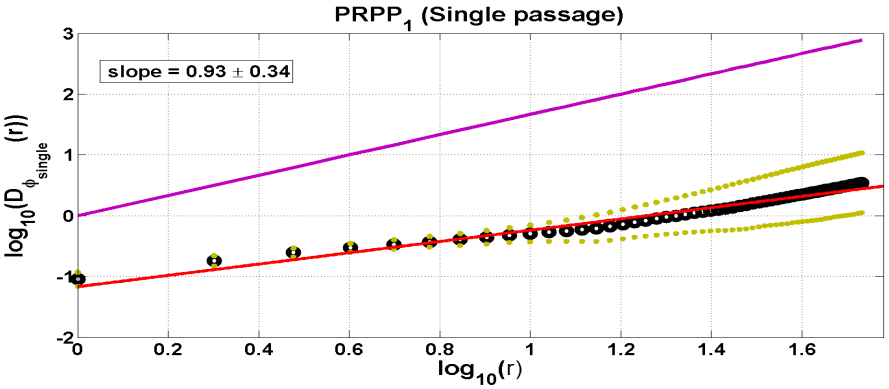

(a)

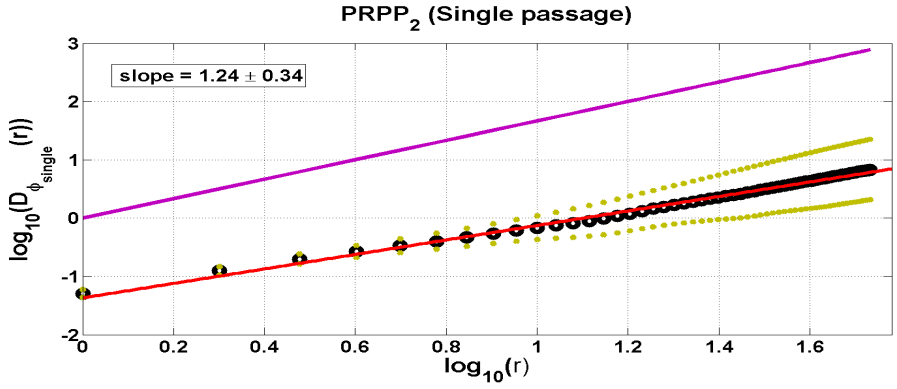

(b)

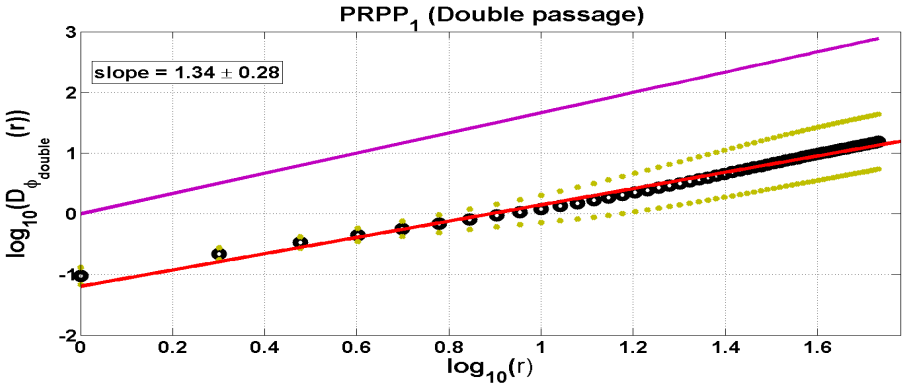

(c)

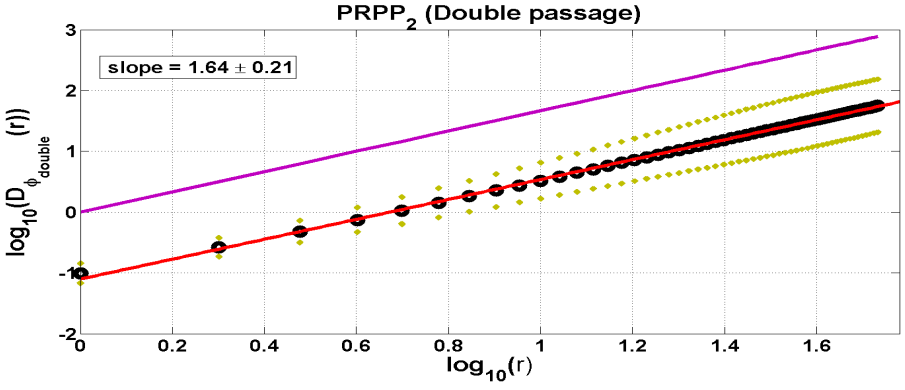

(d)

Figure 2.14: Plots Obtained for Characterization

The slopes obtained from the linearly fitted curves for all cases can be seen in the equations mentioned in the corresponding frames. It is evident from the plots that all the four considered cases represent non-Kolmogorov turbulence regimes Eqn. (2.15) with varying levels of closeness with respect to the Kolmogorov regime (which has been drawn as a violet line in each plot with a slope value of $\frac{5}{3}$). The closest possible case (i.e. the slope which shows the maximum closeness to the Kolmogorov slope) is that for a double passage through $PRPP_2$. Table 2.3 and Table 2.4 show the obtained results for the slopes obtained for both single and double passage geometries, when $PRPP_1$ and $PRPP_2$ respectively were used as objects. For a comparison between the two slopes obtained in the two geometries (single and double passage), a criterion *Difference(%)*, is defined and is given as :

$$\text{Difference}\,(\%) = \frac{(x_{double} - x_{single})}{x_{single}} \times 100 \tag{2.16}$$

where, x denotes the parameter in question i.e, slope. It compares the Difference percentage introduced due to double passage with respect to its single passage value.

It can be seen from the Difference (%) value in these tables, that, there is an increasing tendency of approaching towards the slope value for Kolmogorov turbulence on an increase in the number of passages through the phase plate. $PRPP_2$ (with the double passage slope value of 1.64) almost approaches Kolmogorov slope value of 1.67 with a Difference (%) equal to 32. On the other hand, though the measured increase in the Difference (%) for $PRPP_1$ is greater, the slope value approaches only 1.34.

Therefore, it is evident from the results summarized in Tables 2.3 and 2.4 that by increasing the number of passages through a PRPP, which otherwise presents a non-Kolmogorov turbulence regime in the path of the propagating beam, one can possibly approach the Kolmogorov turbulence regime.

To summarize, two Pseudo-Random-Phase-Plates ($PRPP_1$ and $PRPP_2$) have been characterized, using the Mach-Zehnder and Michelson's interferometers respectively. The Michelson's interferometer geometry allows a double passage through the object in question, in contrast to the single passage allowed through the object in the Mach-Zehnder interferometer. The phase introduced due to a PRPP is retrieved in both the cases and is analysed by calculating the phase structure function. It is found that though both the PRPPs behave like non-Kolmogorov turbulence simulators in both single and

Table 2.3: Slope Comparison for $PRPP_1$

Interferometric Scheme	**$PRPP_1$**
Single Passage	0.93
Double Passage	1.34
Difference (%)	44

Table 2.4: Slope Comparison for $PRPP_2$

Interferometric Scheme	**$PRPP_2$**
Single Passage	1.24
Double Passage	1.64
Difference (%)	32

double passage cases for 633 nm wavelength, the characteristics of turbulence in the two cases are different. The difference in these characteristics has been summarized in Tables 2.3 and 2.4 by means of the Difference(%). The results show that on increasing the number of passages through the PRPPs, there is a possibility of achieving Kolmogorov turbulence regime.

In the next section, an analysis of the interferometric experiments done with the two possible combinations of $PRPP_1$ and $PRPP_2$ has been presented.

2.4 Analysis on Combinations of PRPPs

Now, a combination of PRPPs (i.e. $PRPP_1$ and $PRPP_2$) which have been characterized at 633 nm as non-Kolmogorov turbulence simulators is used in the Mach-Zehnder (single passage through the object) and Michelson's (double passage through the object) interferometer as a *combined object*. The retrieved phases from the fringe pattern images in these two geometries are again analysed using the phase structure function. The experiments are performed using both Mach-Zehnder (single passage through the object) and Michelson's (double passage through the object) interferometers as has been shown in the Figures 2.15 (a) and (b).

The above Figure 2.15 shows the interferometric schemes used for the experiment. These are similar to those discussed in Figures. 2.8 (a) and (b), except for the fact that

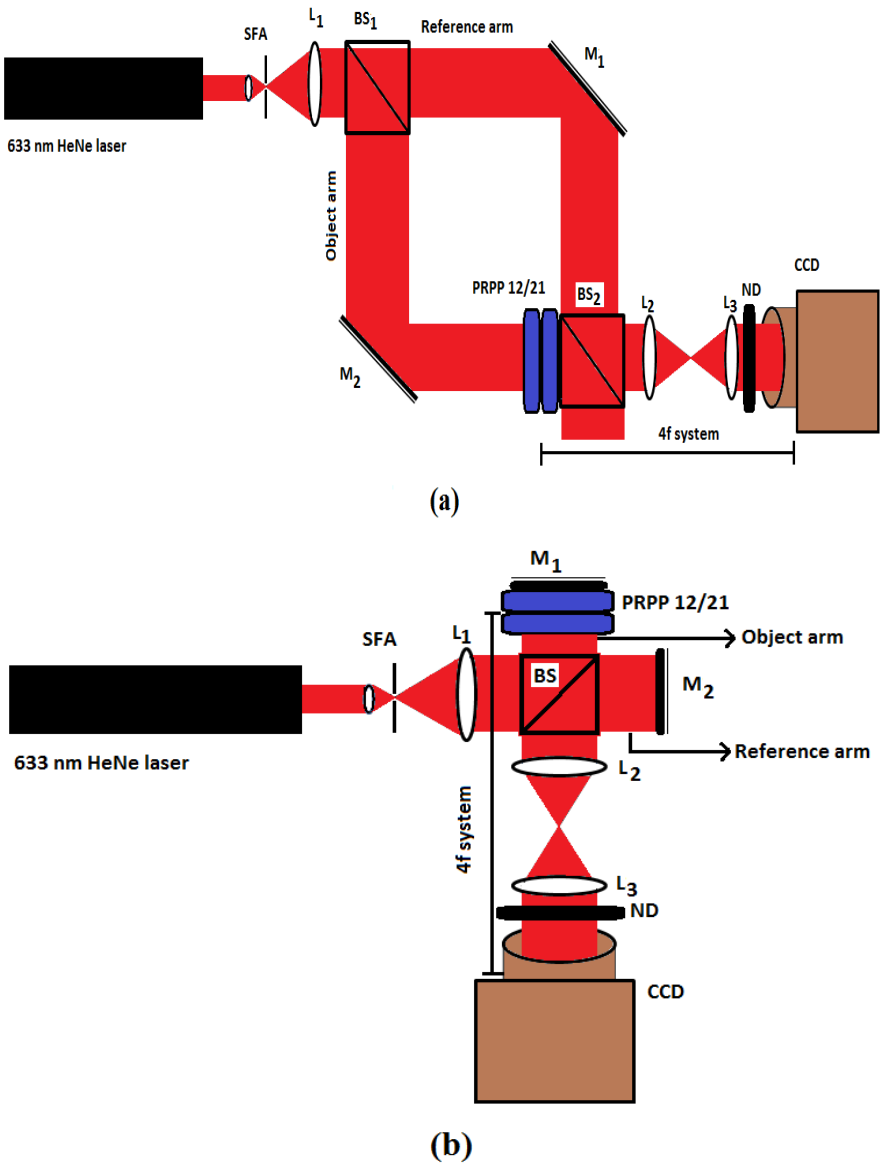

Figure 2.15: Interferometric Schemes for Combined Object

now the inserted objects are PRPP combinations.

It must be noted that the sequence of insertion, when looked in the direction of the propagating beam in object arm is $\text{PRPP}_1 \rightarrow \text{PRPP}_2 \rightarrow$ Beam-Splitter, the inserted object together has been named as PRPP_{21}. On the other hand, the name PRPP_{12} refers to the sequence $\text{PRPP}_2 \rightarrow \text{PRPP}_1 \rightarrow$ Beam-Splitter. The phases added to the 633nm collimated He-Ne laser beam propagating through PRPP_{12} and PRPP_{21} are retrieved, by performing phase retrievals on images, using Hilbert-transform pair technique *Ikeda et al. (2005)* in MATLAB codes (discussed earlier in Section 2.3.1.1).

Subsequently, a 55×55 phase unwrapped portion is selected out of each and the

phase structure function $D_{\phi_{single/double}}$ *Rao et al. (2000)* is calculated on this collected ensemble for each case (Eqns. (2.13) and (2.14)).

Figure 2.16 illustrates the procedure for obtaining 55×55 unwrapped phase portions from the fringe pattern images obtained in *Mach Zehnder (or single passage)* and *Michelson's (or double passage)* interferometric geometry for the above discussed cases. The sequence *a* (i.e. (a_1), (a_2), (a_3), (a_4) and (a_5)) illustrates the steps involved in phase extraction from fringe pattern images when the combination PRPP_{12} is inserted as object (in the focal plane of lens L_2) in the Mach-Zehnder interferometer (Figure 2.15 (a)). (a_1) shows a captured fringe image from the CCD, (a_2) shows the zoomed in version of the Fourier transform for (a_1), (a_3) shows the same zoomed in version of the Fourier transform after high pass filtering, (a_4) is the finally selected zoomed in portion in the Fourier domain and (a_5) shows one of the extracted phase unwrapped portions introduced just due to PRPP_{12}. Similarly, the sequence *b* ((b_1), (b_2), (b_3), (b_4) and (b_5)) corresponds to the case where PRPP_{12} was inserted in the focal plane of lens L_2 as object in the Michelson's interferometer (Figure 2.15 (b)). It shows one of the images taken by the CCD in (b_1), its Fourier transform in (b_2), its high pass filtered Fourier transform in (b_3), the zoomed in finally selected portion in Fourier domain in (b_4) and one of the retrieved phase unwrapped portion of size 55×55 in (b_5). In a similar fashion, the phase unwrapped portions and the involved steps for the cases where PRPP_{21} was inserted as object (in the focal plane of lens L_2) in the Mach-Zehnder and the Michelson's interferometer have been shown in sequences *c* and *d* respectively.

The slope for $log_{10}D_{\phi_{single/double}}(r)$ vs. $log_{10}(r)$ with r going from 1 to 54 in pixel units for each case, along with the equation for its linear fitted curve has been shown in Figure 2.17. These figures show the results for the possible combinations of the PRPPs in the two interferometric geometries considered, i.e. Mach-Zehnder (single passage) and Michelson's (double passage). Also, the slope for Kolmogorov regime has been drawn in violet for all the cases.

$PRPP_{12}$ in Single Passage Geometry	$PRPP_{12}$ in Double Passage Geometry	$PRPP_{21}$ in Single Passage Geometry	$PRPP_{21}$ in Double Passage Geometry

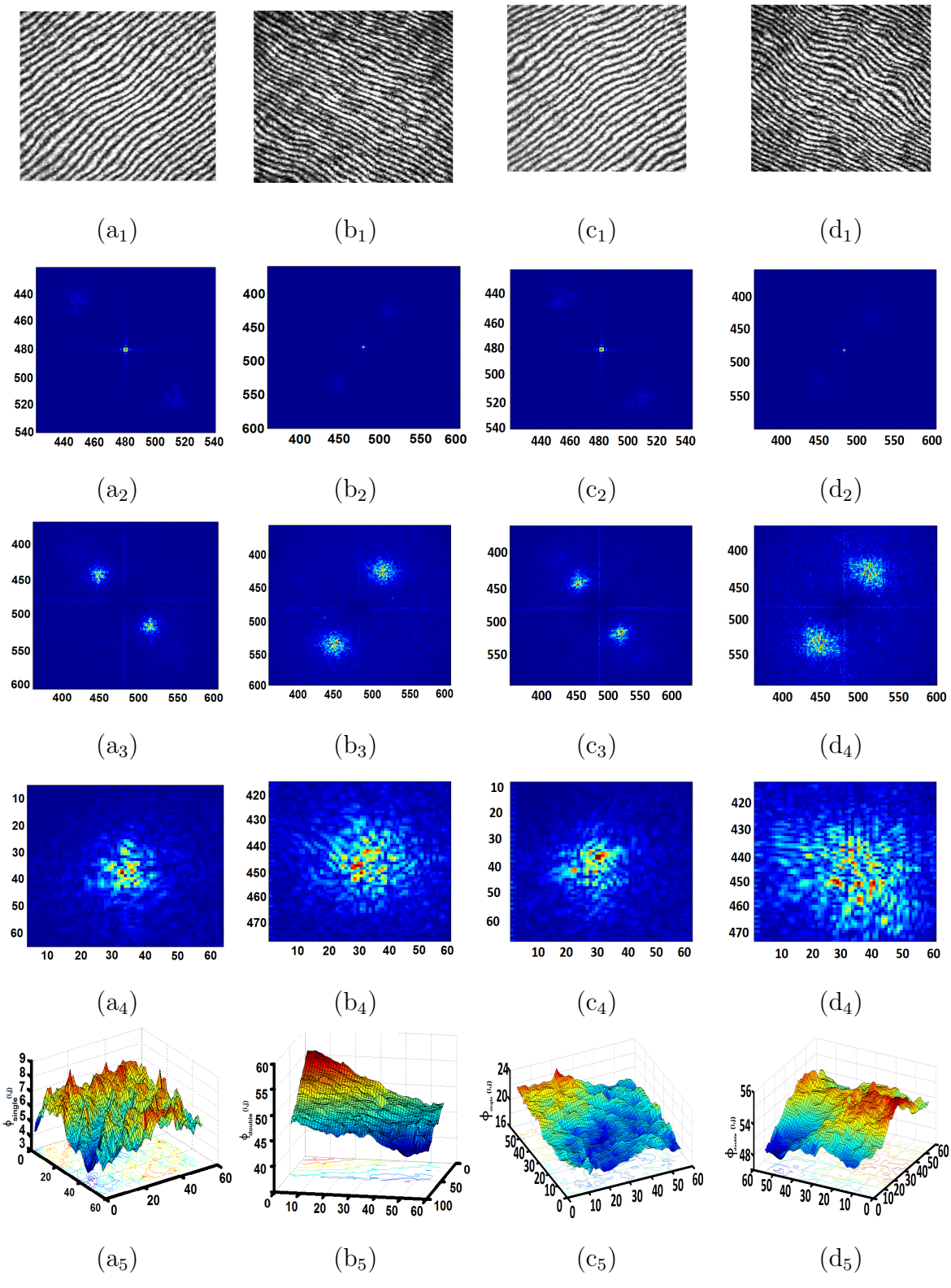

Figure 2.16: Steps Involved in Phase Retrieval for PRPP Combinations

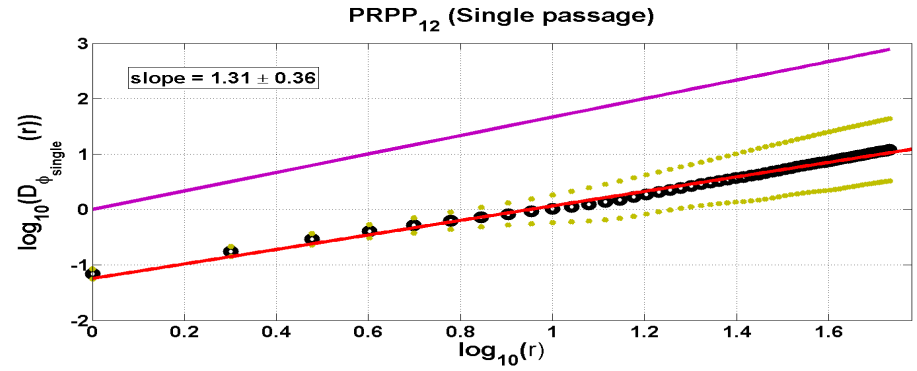

(a)

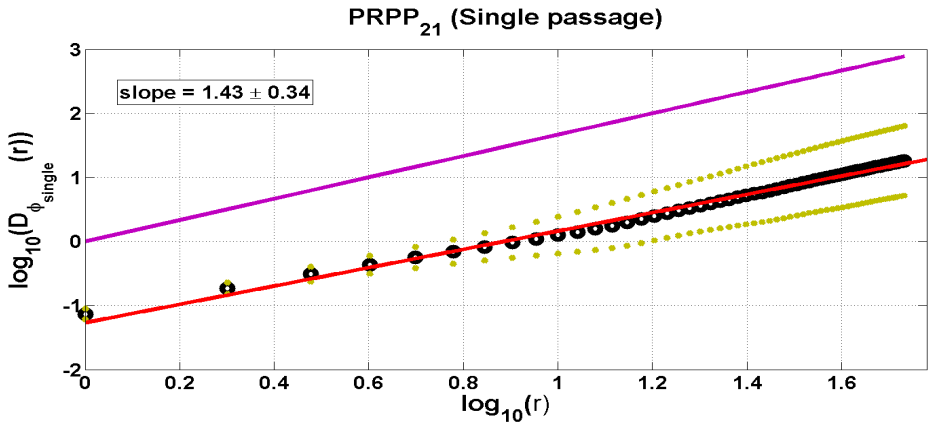

(b)

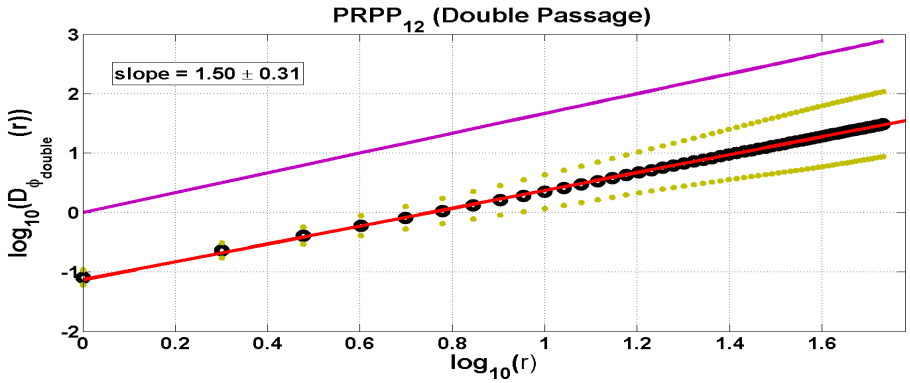

(c)

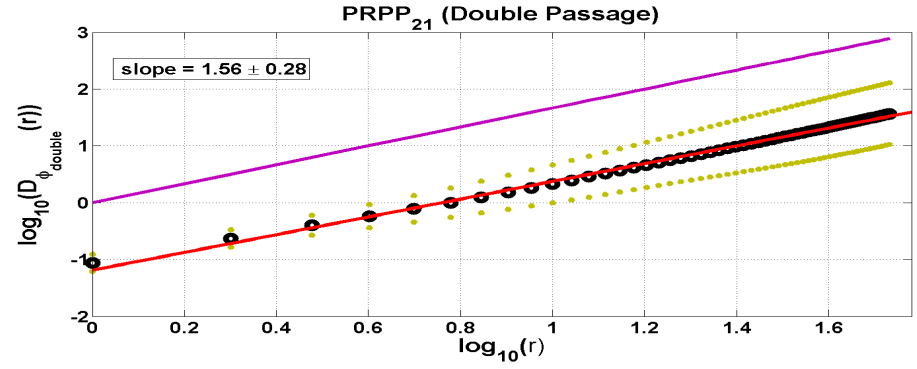

(d)

Figure 2.17: Plots Obtained for the Two respective cases for Combined PRPPs

Table 2.5 shows the results obtained for the two possible combinations of $PRPP_1$ and $PRPP_2$ for both single and double passage cases using the Difference(%) (refer Eq. (2.16)) as the comparison criterion.

Table 2.5: Slope Comparison for $PRPP_{12}$ and $PRPP_{21}$

Interferometric Scheme	**$PRPP_{12}$**	**$PRPP_{21}$**
Single Passage	1.31	1.43
Double Passage	1.50	1.56
Difference (%)	14	9

It is found that though all the considered cases fall into the non-Kolmogorov turbulence regime, the non-Kolmogorov regime presented is different for $PRPP_{12}$ and $PRPP_{21}$. Therefore, it can be concluded that the random phase profile added to the propagating beam by these two random phase plates is dependent on the sequence in which the beam passes through these phase plates. The tendency of approaching towards Kolmogorov turbulence regime on increasing the number of passages through the combined objects ($PRPP_{12}$ and $PRPP_{21}$) is also apparent.

In the next section, a phase-sharing experiment involving a Mach-Zehnder interferometric geometry has been mentioned. This is one of the applications of PRPP in classical cryptography.

2.5 Phase Sharing using Mach-Zehnder Interferometer

To demonstrate the usage of PRPP (here, $PRPP_2$), a phase-sharing scheme using the Mach-Zehnder interferometric set-up has also been designed. In this scheme, two coherent light fields of the same wavelength having orthogonal polarizations are used as sources at the two ends of a Mach-Zehnder interferometer. These are made to interfere independently at the opposing ends of the interferometer, so that the phase estimated by two observers at the two opposing ends of the interferometer is nearly identical. The PRPP now, is inserted in one of the arms of the interferometer to demonstrate that such a phase-sharing scheme could be converted to a secret-key sharing scheme.

The experimental scheme for the mentioned experiment has been shown in Figure 2.18. Coherent light field from 633 nm He-Ne laser (which is fully polarized) is

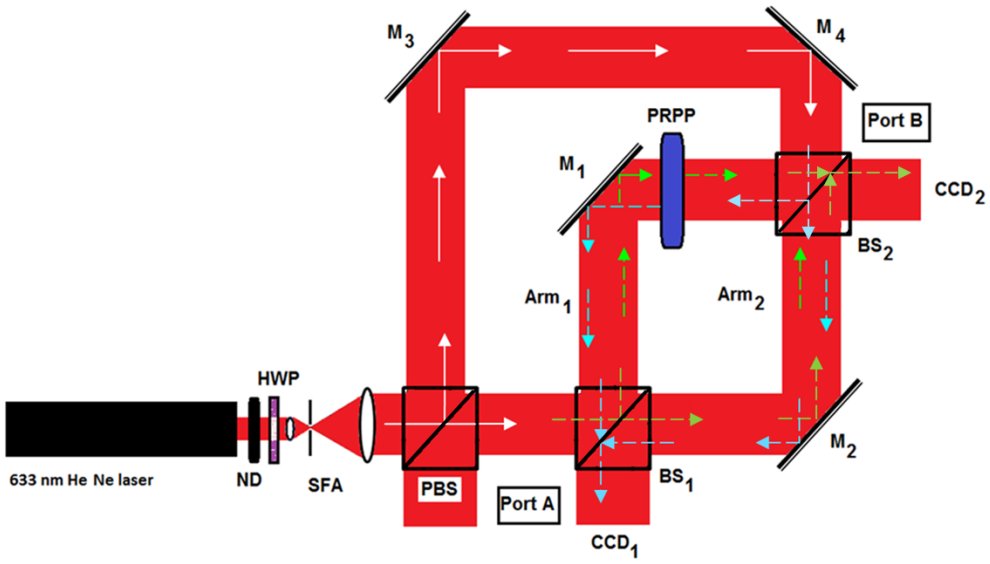

Figure 2.18: Phase-sharing Experiment with the Mach-Zehnder Interferometer

attenuated (using a neutral density filter ND), spatially filtered (with a spatial filtering assembly SFA), collimated, and passed through a rotated half-wave plate (HWP), before being split by a polarizing beam-splitter (PBS) into two light field sources with orthogonal polarizations. These two light field sources act as the two inputs at the two arms of the Mach-Zehnder interferometer. Both these sources are split and recombined by Beam-splitter 1 and Beam-splitter 2 (BS_1, BS_2) to obtain the interference patterns at the two observer ends of the interferometer. The PRPP is inserted in one of the arms of the interferometer so that both the light field sources with orthogonal polarizations encounter the same phase difference in the two arms of the interferometer.

Through the evaluation of the phase correlates of the shared phase samples available at the respective ends of the interferometer, the shared secret-key generation can be demonstrated. The scheme could be in principle used by two remote observers to simultaneously monitor and study a phase object inserted in one of the arms of the interferometer.

Also, one of the major ways of tapping the suggested experiment's potential is when the two remote observers are well-separated spatially so that *atmospheric turbulence* in the arms of the interferometer generates the shared random phases. It is worth noticing that, the shared random phases could also be used in a more direct manner by the respective observers for random phase encryption of images as well as other cryptographic applications.

2.6 Summary

In total, in the present work, the random phase introduced by two PRPPs (either *individually* or *in-a-combination*) in the path of a propagating 633 nm He-Ne laser wave-field has been analysed. This has been done by inserting the PRPPs as objects (individually or in-a-combination) in one of the arms of a Mach-Zehnder and a Michelson's interferometers. It is found that both the PRPPs under consideration (which have been claimed by the manufacturers as Kolmogorov turbulence simulators at 1550 nm) behave like non-Kolmogorov turbulence simulators at 633 nm , when introduced individually or jointly. Therefore, the work has quite emphatically revealed the *wavelength dependence* of the characteristics of these media. It is also noticed that the nature of turbulence depends upon the number of passages the beam travels through these PRPPs (individually or in-a-combination) and there is a tendency of approaching towards Kolmogorov turbulence regime with an increase in the number of passages for 633 nm wavelength. This shows the *number of passage dependence* of the characteristics of these media for a particular wavelength.

It should also be noted that the employment of the two well known interferometric geometries, namely the Mach-Zehnder and Michelson's interferometer for *single* and *double* passage respectively through the medium ($PRPP_1$/$PRPP_2$/PRPPs in-a-combination) is also a novel approach for the exploration of such random media. Finally, a characterized PRPP ($PRPP_2$) has been used in a phase-sharing experiment involving a Mach-Zehnder interferometric geometry to demonstrate the possibility of sharing a secret key between two remote observers.

CHAPTER 3

Wave Propagation Analysis using the Variance Matrix

3.1 Introduction

To characterize a given wave-field, one usually computes the expectation value of the observable operators (such as *position* and *momentum*) on the wave-field *Siegman (1990); Wright et al. (1992); Simon et al. (1994); Simon and Mukunda (2000); Bastiaans (1979).* For a coherent wave-field, this can be done in a restricted manner by evaluating its second moments which form the *Variance matrix* (V) *Simon et al. (1994); Simon and Mukunda (2000).* When a coherent wave-field propagates through a medium capable of inducing random changes to its phase and amplitude, the wave-field gets distorted, which is captured through V. This V can then be compared with the V corresponding to the undistorted wave-field, i.e. the one, which is not subject to passage through random medium in question.

The present chapter considers one of the Pseudo-Random-Phase-Plates (PRPPs) belonging to the class of such media *(which were characterized earlier in Chapter 2 as non-Kolmogorov turbulence simulators with a 633 nm He-Ne laser source)* and estimates the V at different propagation distances, by allowing a single and double passage of the wave-field through it.

3.2 Variance Matrix (V): Genesis, Properties, and Applications

The complete characterization of a beam upto the level of second moments can be done using the *Variance matrix*, V *Simon et al. (1994); Simon and Mukunda (2000).* It is a $2n \times 2n$ (with n being the number of modes), real, symmetric, positive-definite matrix. For a realistic beam propagating along z direction (say), completely described by the x and y modes in one particular transverse plane, V is a 4×4 matrix with 10 independent second moments.

In the present section, the genesis of V, and some of its important properties have been put forth. Also, some physically significant entities derivable out of V are described. These are subsequently used to investigate the effects of propagation of a 633 nm laser beam through the PRPP.

3.2.1 Basics of V

First, an arrangement of Hermitian operators *Simon et al. (1994)* $\hat{q}$s and $\hat{p}$s in the form of a $2n$ component column vector $\Delta\hat{\xi}$, is considered. This is expressed as follows:

$$\Delta\hat{\xi} = \begin{bmatrix} \Delta\hat{q_1} = \hat{q_1} - \langle\hat{q_1}\rangle \\ \Delta\hat{p_1} = \hat{p_1} - \langle\hat{p_1}\rangle \\ \Delta\hat{q_2} = \hat{q_2} - \langle\hat{q_2}\rangle \\ \Delta\hat{p_2} = \hat{p_2} - \langle\hat{p_2}\rangle \\ \vdots \\ \Delta\hat{q_n} = \hat{q_n} - \langle\hat{q_n}\rangle \\ \Delta\hat{p_n} = \hat{p_n} - \langle\hat{p_n}\rangle \end{bmatrix} \tag{3.1}$$

where, $\langle . \rangle$ denotes the ensemble average of the respective variable.

$n = 2$ case is of importance here, i.e. a system described by a set of 2 variables/-modes, such that: $\hat{q}_1 = \hat{x}$, $\hat{q}_2 = \hat{y}$, $\hat{p}_1 = \hat{p}_x$ and $\hat{p}_2 = \hat{p}_y$. Therefore, $\Delta\hat{\xi}$ becomes,

$$\Delta\hat{\xi} = \begin{bmatrix} \Delta\hat{x} \\ \Delta\hat{p_x} \\ \Delta\hat{y} \\ \Delta\hat{p_y} \end{bmatrix} \tag{3.2}$$

Considering $\left[\Delta\hat{\xi}_i, \Delta\hat{\xi}_j\right]$, where $[\cdot]$ are the well known commutator brackets and both i and j go from 1 to 4, all the commutation relationships between the elements of the matrix $\Delta\hat{\xi}$ can be derived in the manner shown in APPENDIX B.1

$[\Delta\xi_i \Delta\xi_j]$, when written explicitly in a matrix form, becomes :

$$[\Delta\xi_i \Delta\xi_j] = \begin{bmatrix} [\Delta\xi_1, \Delta\xi_1] & [\Delta\xi_1, \Delta\xi_2] & [\Delta\xi_1, \Delta\xi_3] & [\Delta\xi_1, \Delta\xi_4] \\ [\Delta\xi_2, \Delta\xi_1] & [\Delta\xi_2, \Delta\xi_2] & [\Delta\xi_2, \Delta\xi_3] & [\Delta\xi_2, \Delta\xi_4] \\ [\Delta\xi_3, \Delta\xi_1] & [\Delta\xi_3, \Delta\xi_2] & [\Delta\xi_3, \Delta\xi_3] & [\Delta\xi_3, \Delta\xi_4] \\ [\Delta\xi_4, \Delta\xi_1] & [\Delta\xi_4, \Delta\xi_2] & [\Delta\xi_4, \Delta\xi_3] & [\Delta\xi_4, \Delta\xi_4] \end{bmatrix} = \begin{bmatrix} 0 & i\lambda & 0 & 0 \\ -i\lambda & 0 & 0 & 0 \\ 0 & 0 & 0 & i\lambda \\ 0 & 0 & -i\lambda & 0 \end{bmatrix}$$

$$= i\lambda \begin{bmatrix} 0 & 1 & 0 & 0 \\ -1 & 0 & 0 & 0 \\ 0 & 0 & 0 & 1 \\ 0 & 0 & -1 & 0 \end{bmatrix} \tag{3.3}$$

The above deduced relations can be written in a concise form as follows :

$$[\Delta\hat{\xi}_i, \Delta\hat{\xi}_j] = i\lambda\beta \tag{3.4}$$

where, both the indices i, j go from 1 to 4, and in (3.4), β is defined as :

$$\beta = \begin{bmatrix} 0 & 1 & 0 & 0 \\ -1 & 0 & 0 & 0 \\ 0 & 0 & 0 & 1 \\ 0 & 0 & -1 & 0 \end{bmatrix} = \begin{bmatrix} i\sigma_2 & \mathbf{0} \\ \mathbf{0} & i\sigma_2 \end{bmatrix} \tag{3.5}$$

with, σ_2 being the Pauli's matrix :

$$\sigma_2 = \begin{bmatrix} 0 & -i \\ i & 0 \end{bmatrix} \tag{3.6}$$

Now, considering the matrix , $\Delta\hat{\xi}\Delta\hat{\xi}^T$:

$$\Delta\hat{\xi}\Delta\hat{\xi}^{T} = \begin{bmatrix} \Delta\hat{x} \\ \Delta\hat{p_x} \\ \Delta\hat{y} \\ \Delta\hat{p_y} \end{bmatrix} \begin{bmatrix} \Delta\hat{x} & \Delta\hat{p_x} & \Delta\hat{y} & \Delta\hat{p_y} \end{bmatrix} \tag{3.7}$$

$$= \begin{bmatrix} (\Delta\hat{x})^2 & \Delta\hat{x}\Delta\hat{p_x} & \Delta\hat{x}\Delta\hat{y} & \Delta\hat{x}\Delta\hat{p_y} \\ \Delta\hat{p_x}\Delta\hat{x} & (\Delta\hat{p_x})^2 & \Delta\hat{p_x}\Delta\hat{y} & \Delta\hat{p_x}\Delta\hat{p_y} \\ \Delta\hat{y}\Delta\hat{x} & \Delta\hat{y}\Delta\hat{p_x} & (\Delta\hat{y})^2 & \Delta\hat{y}\Delta\hat{p_y} \\ \Delta\hat{p_y}\Delta\hat{x} & \Delta\hat{p_y}\Delta\hat{p_x} & \Delta\hat{p_y}\Delta\hat{y} & (\Delta\hat{p_y})^2 \end{bmatrix} \tag{3.8}$$

The elements of the above matrix can be evaluated further by considering the equations (B.1) to (B.16), as derived earlier. For instance, let the term $\Delta\hat{x}\Delta\hat{p_x}$ can be written as :

$$\begin{aligned} \Delta\hat{x}\Delta\hat{p_x} &= \frac{1}{2}(2\Delta\hat{x}\Delta\hat{p_x}) \\ &= \frac{1}{2}(\Delta\hat{x}\Delta\hat{p_x} + \Delta\hat{x}\Delta\hat{p_x}) \end{aligned} \tag{3.9}$$

From (B.2) :

$$\Delta\hat{x}\Delta\hat{p_x} = \Delta\hat{p_x}\Delta\hat{x} + i\text{ƛ} \tag{3.10}$$

Using (3.9) and (3.10) the expression for $\Delta\hat{x}\Delta\hat{p_x}$ becomes :

$$\Delta\hat{x}\Delta\hat{p_x} = \frac{1}{2}(\Delta\hat{x}\Delta\hat{p_x} + \Delta\hat{p_x}\Delta\hat{x} + i\text{ƛ}) \tag{3.11}$$

In a similar manner, all other entries in the matrix (3.8) can be deduced using Eqs. (B.1)

to (B.16) to obtain the following :

$$\Delta\hat{\xi}\Delta\hat{\xi}^T = \begin{bmatrix} \frac{1}{2}(\Delta\hat{x}\Delta\hat{x}+\Delta\hat{x}\Delta\hat{x}) & \frac{1}{2}(\Delta\hat{x}\Delta\hat{p_x}+\Delta\hat{p_x}\Delta\hat{x}+i\lambda) & \frac{1}{2}(\Delta\hat{x}\Delta\hat{y}+\Delta\hat{y}\Delta\hat{x}) & \frac{1}{2}(\Delta\hat{x}\Delta\hat{p_y}+\Delta\hat{p_y}\Delta\hat{x}) \\ \frac{1}{2}(\Delta\hat{p_x}\Delta\hat{x}+\Delta\hat{x}\Delta\hat{p_x}-i\lambda) & \frac{1}{2}(\Delta\hat{p_x}\Delta\hat{p_x}+\Delta\hat{p_x}\Delta\hat{p_x}) & \frac{1}{2}(\Delta\hat{p_x}\Delta\hat{y}+\Delta\hat{y}\Delta\hat{p_x}) & \frac{1}{2}(\Delta\hat{p_x}\Delta\hat{p_y}+\Delta\hat{p_y}\Delta\hat{p_x}) \\ \frac{1}{2}(\Delta\hat{y}\Delta\hat{x}+\Delta\hat{x}\Delta\hat{y}) & \frac{1}{2}(\Delta\hat{y}\Delta\hat{p_x}+\Delta\hat{p_x}\Delta\hat{y}) & \frac{1}{2}(\Delta\hat{y}\Delta\hat{y}+\Delta\hat{y}\Delta\hat{y}) & \frac{1}{2}(\Delta\hat{y}\Delta\hat{p_y}+\Delta\hat{p_y}\Delta\hat{y}+i\lambda) \\ \frac{1}{2}(\Delta\hat{p_y}\Delta\hat{x}+\Delta\hat{x}\Delta\hat{p_y}) & \frac{1}{2}(\Delta\hat{p_y}\Delta\hat{p_x}+\Delta\hat{p_x}\Delta\hat{p_y}) & \frac{1}{2}(\Delta\hat{p_y}\Delta\hat{y}+\Delta\hat{y}\Delta\hat{p_y}-i\lambda) & \frac{1}{2}(\Delta\hat{p_y}\Delta\hat{p_y}+\Delta\hat{p_y}\Delta\hat{p_y}) \end{bmatrix} \tag{3.12}$$

$$= \begin{bmatrix} \frac{1}{2}\{\Delta\hat{x},\Delta\hat{x}\} & \frac{1}{2}\{\Delta\hat{x},\Delta\hat{p_x}\}+\frac{i\lambda}{2} & \frac{1}{2}\{\Delta\hat{x},\Delta\hat{y}\} & \frac{1}{2}\{\Delta\hat{x},\Delta\hat{p_y}\} \\ \frac{1}{2}\{\Delta\hat{p_x},\Delta\hat{x}\}-\frac{i\lambda}{2} & \frac{1}{2}\{\Delta\hat{p_x},\Delta\hat{p_x}\} & \frac{1}{2}\{\Delta\hat{p_x},\Delta\hat{y}\} & \frac{1}{2}\{\Delta\hat{p_x},\Delta\hat{p_y}\} \\ \frac{1}{2}\{\Delta\hat{y},\Delta\hat{x}\} & \frac{1}{2}\{\Delta\hat{y},\Delta\hat{p_x}\} & \frac{1}{2}\{\Delta\hat{y},\Delta\hat{y}\} & \frac{1}{2}\{\Delta\hat{y},\Delta\hat{p_y}\}+\frac{i\lambda}{2} \\ \frac{1}{2}\{\Delta\hat{p_y},\Delta\hat{x}\} & \frac{1}{2}\{\Delta\hat{p_y},\Delta\hat{p_x}\} & \frac{1}{2}\{\Delta\hat{p_y},\Delta\hat{y}\}-\frac{i\lambda}{2} & \frac{1}{2}\{\Delta\hat{p_y},\Delta\hat{p_y}\} \end{bmatrix} \tag{3.13}$$

In matrix (3.13), $\{\cdot\}$ denotes the anti-commutator brackets, such that $\{\hat{A},\hat{B}\} = \hat{A}\hat{B} + \hat{B}\hat{A}$ for any two operators $\hat{A}$ and $\hat{B}$. Furthermore, the diagonal entries in the matrix (3.13) can be simplified which leads to :

$$\Delta\hat{\xi}\Delta\hat{\xi}^T = \begin{bmatrix} \Delta\hat{x}^2 & \frac{1}{2}\{\Delta\hat{x},\Delta\hat{p_x}\}+\frac{i\lambda}{2} & \frac{1}{2}\{\Delta\hat{x},\Delta\hat{y}\} & \frac{1}{2}\{\Delta\hat{x},\Delta\hat{p_y}\} \\ \frac{1}{2}\{\Delta\hat{p_x},\Delta\hat{x}\}-\frac{i\lambda}{2} & \Delta\hat{p_x}^2 & \frac{1}{2}\{\Delta\hat{p_x},\Delta\hat{y}\} & \frac{1}{2}\{\Delta\hat{p_x},\Delta\hat{p_y}\} \\ \frac{1}{2}\{\Delta\hat{y},\Delta\hat{x}\} & \frac{1}{2}\{\Delta\hat{y},\Delta\hat{p_x}\} & \Delta\hat{y}^2 & \frac{1}{2}\{\Delta\hat{y},\Delta\hat{p_y}\}+\frac{i\lambda}{2} \\ \frac{1}{2}\{\Delta\hat{p_y},\Delta\hat{x}\} & \frac{1}{2}\{\Delta\hat{p_y},\Delta\hat{p_x}\} & \frac{1}{2}\{\Delta\hat{p_y},\Delta\hat{y}\}-\frac{i\lambda}{2} & \Delta\hat{p_y}^2 \end{bmatrix}$$

$$= \begin{bmatrix} \Delta\hat{x}^2 & \frac{1}{2}\{\Delta\hat{x},\Delta\hat{p_x}\} & \frac{1}{2}\{\Delta\hat{x},\Delta\hat{y}\} & \frac{1}{2}\{\Delta\hat{x},\Delta\hat{p_y}\} \\ \frac{1}{2}\{\Delta\hat{p_x},\Delta\hat{x}\} & \Delta\hat{p_x}^2 & \frac{1}{2}\{\Delta\hat{p_x},\Delta\hat{y}\} & \frac{1}{2}\{\Delta\hat{p_x},\Delta\hat{p_y}\} \\ \frac{1}{2}\{\Delta\hat{y},\Delta\hat{x}\} & \frac{1}{2}\{\Delta\hat{y},\Delta\hat{p_x}\} & \Delta\hat{y}^2 & \frac{1}{2}\{\Delta\hat{y},\Delta\hat{p_y}\} \\ \frac{1}{2}\{\Delta\hat{p_y},\Delta\hat{x}\} & \frac{1}{2}\{\Delta\hat{p_y},\Delta\hat{p_x}\} & \frac{1}{2}\{\Delta\hat{p_y},\Delta\hat{y}\} & \Delta\hat{p_y}^2 \end{bmatrix} + \begin{bmatrix} 0 & \frac{i\lambda}{2} & 0 & 0 \\ -\frac{i\lambda}{2} & 0 & 0 & 0 \\ 0 & 0 & 0 & \frac{i\lambda}{2} \\ 0 & 0 & -\frac{i\lambda}{2} & 0 \end{bmatrix}$$

$$= \begin{bmatrix} \Delta\hat{x}^2 & \frac{1}{2}\{\Delta\hat{x},\Delta\hat{p_x}\} & \frac{1}{2}\{\Delta\hat{x},\Delta\hat{y}\} & \frac{1}{2}\{\Delta\hat{x},\Delta\hat{p_y}\} \\ \frac{1}{2}\{\Delta\hat{p_x},\Delta\hat{x}\} & \Delta\hat{p_x}^2 & \frac{1}{2}\{\Delta\hat{p_x},\Delta\hat{y}\} & \frac{1}{2}\{\Delta\hat{p_x},\Delta\hat{p_y}\} \\ \frac{1}{2}\{\Delta\hat{y},\Delta\hat{x}\} & \frac{1}{2}\{\Delta\hat{y},\Delta\hat{p_x}\} & \Delta\hat{y}^2 & \frac{1}{2}\{\Delta\hat{y},\Delta\hat{p_y}\} \\ \frac{1}{2}\{\Delta\hat{p_y},\Delta\hat{x}\} & \frac{1}{2}\{\Delta\hat{p_y},\Delta\hat{p_x}\} & \frac{1}{2}\{\Delta\hat{p_y},\Delta\hat{y}\} & \Delta\hat{p_y}^2 \end{bmatrix} + \frac{i\lambda}{2}\begin{bmatrix} 0 & 1 & 0 & 0 \\ -1 & 0 & 0 & 0 \\ 0 & 0 & 0 & 1 \\ 0 & 0 & -1 & 0 \end{bmatrix} \tag{3.14}$$

The above expression, with the substitutions,

1. $\begin{bmatrix} 0 & 1 & 0 & 0 \\ -1 & 0 & 0 & 0 \\ 0 & 0 & 0 & 1 \\ 0 & 0 & -1 & 0 \end{bmatrix} = \beta$ (recollecting from Eqn. (3.5)) and

2. $\begin{bmatrix} \Delta\hat{x}^2 & \frac{1}{2}\{\Delta\hat{x}, \Delta\hat{p_x}\} & \frac{1}{2}\{\Delta\hat{x}, \Delta\hat{y}\} & \frac{1}{2}\{\Delta\hat{x}, \Delta\hat{p_y}\} \\ \frac{1}{2}\{\Delta\hat{p_x}, \Delta\hat{x}\} & \Delta\hat{p_x}^2 & \frac{1}{2}\{\Delta\hat{p_x}, \Delta\hat{y}\} & \frac{1}{2}\{\Delta\hat{p_x}, \Delta\hat{p_y}\} \\ \frac{1}{2}\{\Delta\hat{y}, \Delta\hat{x}\} & \frac{1}{2}\{\Delta\hat{y}, \Delta\hat{p_x}\} & \Delta\hat{y}^2 & \frac{1}{2}\{\Delta\hat{y}, \Delta\hat{p_y}\} \\ \frac{1}{2}\{\Delta\hat{p_y}, \Delta\hat{x}\} & \frac{1}{2}\{\Delta\hat{p_y}, \Delta\hat{p_x}\} & \frac{1}{2}\{\Delta\hat{p_y}, \Delta\hat{y}\} & \Delta\hat{p_y}^2 \end{bmatrix} = \frac{1}{2}\{\Delta\hat{\xi_i}, \Delta\hat{\xi_j}\}$

becomes:

$$\Delta\hat{\xi}\Delta\hat{\xi}^{\mathbf{T}} = \frac{1}{2}\{\Delta\hat{\xi_i}, \Delta\hat{\xi_j}\} + \frac{i\hbar}{2}\beta_{ij}. \tag{3.15}$$

where, i, j both go from 1 to 4.

On taking the ensemble average on both sides of Eqn. (3.15), the following equations are reached at :

$$\langle\Delta\hat{\xi}\Delta\hat{\xi}^{\mathbf{T}}\rangle = \frac{1}{2}\langle\{\Delta\hat{\xi}, \Delta\hat{\xi}\}\rangle + \frac{i\hbar}{2}\beta \tag{3.16}$$

The term $\frac{1}{2}\langle\{\Delta\hat{\xi_i}, \Delta\hat{\xi_j}\}\rangle$ in (3.16) is nothing but the variance matrix V. Therefore, (3.16) is written as :

$$\langle\Delta\hat{\xi}\Delta\hat{\xi}^{\mathbf{T}}\rangle = V + \frac{i\hbar}{2}\beta \tag{3.17}$$

In the next section, the evaluation of V in the above expression for the case of a monochromatic, scalar, paraxial beam has been done.

3.2.2 Calculation of V for a Monochromatic, Scalar, Paraxial Beam

A monochromatic scalar beam (or wave-field) propagating along the z direction (paraxially) can be expressed as a complex-valued function,

$$\Psi(x, y, z) = \psi(x, y, z)e^{-2\pi i\nu t} \tag{3.18}$$

where $\psi(x, y, z)$ specifies the transverse spatial dependence of the wave-field for a given z, and ν its frequency. The transverse space-dependent part for a given z, denoted by

$\psi(x, y)$, can be written as :

$$\psi(x, y) = A(x, y)e^{i\phi(x,y)}. \tag{3.19}$$

where, $A(x, y)$ denotes the real, amplitude part of the beam, and $\phi(x, y)$, the phase. Both amplitude and phase are functions of x and y. It should be noted that the intensity of this beam is calculated as:

$$\begin{aligned} I(x, y) &= \psi(x, y)^* \psi(x, y) \\ &= \left(A(x, y)e^{i\phi(x,y)}\right)^* A(x, y)e^{i\phi(x,y)} \\ &= A(x, y)e^{-i\phi(x,y)} A(x, y)e^{i\phi(x,y)} \\ &= \left(A(x, y)\right)^2 \end{aligned}$$

$A(x, y)^* = A(x, y)$ because $A(x, y)$ is real. Also, from the above, the following can be inferred:

1. The amplitude and intensity are related as :

$$A(x, y) = \pm\sqrt{I(x, y)} \tag{3.20}$$

2. Partial differentiation of intensity with respect to x and y is given as :

$$\frac{\partial I(x, y)}{\partial x} = \frac{\partial(A^2(x, y))}{\partial x} = 2A(x, y)\frac{\partial A(x, y)}{\partial x} \tag{3.21}$$

$$\frac{\partial I(x, y)}{\partial y} = \frac{\partial(A^2(x, y))}{\partial y} = 2A(x, y)\frac{\partial A(x, y)}{\partial x} \tag{3.22}$$

Recall that the variance matrix (V) (3.16) is given as follows :

$$V = \begin{bmatrix} \langle(\Delta\hat{x})^2\rangle & \frac{1}{2}\langle\{\Delta\hat{x}, \Delta\hat{p_x}\}\rangle & \langle\Delta\hat{x}\Delta\hat{y}\rangle & \langle\Delta\hat{x}\Delta\hat{p_y}\rangle \\ \frac{1}{2}\langle\{\Delta\hat{p_x}, \Delta\hat{x}\}\rangle & \langle(\Delta\hat{p_x})^2\rangle & \langle\Delta\hat{p}_x\Delta\hat{y}\rangle & \langle\Delta\hat{p_x}\Delta\hat{p_y}\rangle \\ \langle\Delta\hat{y}\Delta\hat{x}\rangle & \langle\Delta\hat{y}\Delta\hat{p}_x\rangle & \langle(\Delta\hat{y})^2\rangle & \frac{1}{2}\langle\{\Delta\hat{y}, \Delta\hat{p_y}\}\rangle \\ \langle\Delta\hat{p_y}\Delta\hat{x}\rangle & \langle\Delta\hat{p_y}\Delta\hat{p}_x\rangle & \frac{1}{2}\langle\{\Delta\hat{p_y}, \Delta\hat{y}\}\rangle & \langle(\Delta\hat{p_y})^2\rangle \end{bmatrix} \tag{3.23}$$

Each element of V is now simplified in the manner shown in APPENDIX B.2 and V can now be written as,

$$V = \begin{bmatrix} \langle(\Delta\hat{x})^2\rangle & \frac{1}{2}\langle\{\Delta\hat{x},\Delta\hat{p_x}\}\rangle & \langle\Delta\hat{x}\Delta\hat{y}\rangle & \langle\Delta\hat{x}\Delta\hat{p_y}\rangle \\ \frac{1}{2}\langle\{\Delta\hat{p_x},\Delta\hat{x}\}\rangle & \langle(\Delta\hat{p_x})^2\rangle & \langle\Delta\hat{p}_x\Delta\hat{y}\rangle & \langle\Delta\hat{p_x}\Delta\hat{p_y}\rangle \\ \langle\Delta\hat{y}\Delta\hat{x}\rangle & \langle\Delta\hat{y}\Delta\hat{p}_x\rangle & \langle(\Delta\hat{y})^2\rangle & \frac{1}{2}\langle\{\Delta\hat{y},\Delta\hat{p_y}\}\rangle \\ \langle\Delta\hat{p_y}\Delta\hat{x}\rangle & \langle\Delta\hat{p_y}\Delta\hat{p_x}\rangle & \frac{1}{2}\langle\{\Delta\hat{p_y},\Delta\hat{y}\}\rangle & \langle(\Delta\hat{p_y})^2\rangle \end{bmatrix}$$

$$= \begin{bmatrix} \langle(\hat{x})^2\rangle - c_1^2 & \frac{1}{2}\langle\{\hat{x},\hat{p_x}\}\rangle - c_1c_3 & \langle\hat{x}\hat{y}\rangle - c_1c_2 & \langle\hat{x}\hat{p_y}\rangle - c_1c_4 \\ \frac{1}{2}\langle\{\hat{p_x},\hat{x}\}\rangle - c_1c_3 & \langle(\hat{p_x})^2\rangle - c_3^2 & \langle\hat{p}_x\hat{y}\rangle - c_3c_2 & \langle\hat{p_x}\hat{p_y}\rangle - c_3c_4 \\ \langle\hat{y}\hat{x}\rangle - c_1c_2 & \langle\hat{y}\hat{p}_x\rangle - c_2c_3 & \langle(\hat{y})^2\rangle - c_2^2 & \frac{1}{2}\langle\{\hat{y},\hat{p_y}\}\rangle - c_2c_4 \\ \langle\hat{p_y}\hat{x}\rangle - c_1c_4 & \langle\hat{p_y}\hat{p_x}\rangle - c_3c_4 & \frac{1}{2}\langle\{\hat{p_y},\hat{y}\}\rangle - c_2c_4 & \langle(\hat{p_y})^2\rangle - c_4^2 \end{bmatrix}$$

$$= \begin{bmatrix} \langle(\hat{x})^2\rangle & \frac{1}{2}\langle\{\hat{x},\hat{p_x}\}\rangle & \langle\hat{x}\hat{y}\rangle & \langle\hat{x}\hat{p_y}\rangle \\ \frac{1}{2}\langle\{\hat{p_x},\hat{x}\}\rangle & \langle(\hat{p_x})^2\rangle & \langle\hat{p}_x\hat{y}\rangle & \langle\hat{p_x}\hat{p_y}\rangle \\ \langle\hat{y}\hat{x}\rangle & \langle\hat{y}\hat{p}_x\rangle & \langle(\hat{y})^2\rangle & \frac{1}{2}\langle\{\hat{y},\hat{p_y}\}\rangle \\ \langle\hat{p_y}\hat{x}\rangle & \langle\hat{p_y}\hat{p_x}\rangle & \frac{1}{2}\langle\{\hat{p_y},\hat{y}\}\rangle & \langle(\hat{p_y})^2\rangle \end{bmatrix} - \begin{bmatrix} c_1^2 & c_1c_3 & c_1c_2 & c_1c_4 \\ c_1c_3 & c_3^2 & c_3c_2 & c_3c_4 \\ c_1c_2 & c_2c_3 & c_2^2 & c_2c_4 \\ c_1c_4 & c_3c_4 & c_2c_4 & c_4^2 \end{bmatrix} \tag{3.24}$$

In the next section, a discussion on some properties of the above generated V have been given. Also, the calculation of some measurable quantities of physical significance, from this matrix has been shown.

3.2.3 Uncertainty Principle and the Variance Matrix

In the block representation, V (3.16) can be written as,

$$V_{ij} = \begin{bmatrix} V_{11} & V_{12} \\ V_{21} & V_{22} \end{bmatrix} \tag{3.25}$$

where,

$$V_{11} = \begin{bmatrix} \langle \Delta\hat{x}^2 \rangle & \frac{1}{2}\langle \{\Delta\hat{x}, \Delta\hat{p_x}\} \rangle \\ \frac{1}{2}\langle \{\Delta\hat{x}, \Delta\hat{p_x}\} \rangle & \langle \Delta\hat{p_x}^2 \rangle \end{bmatrix} \tag{3.26}$$

$$V_{12} = V_{21}^{\mathbf{T}} = \begin{bmatrix} \langle \Delta\hat{x}\Delta\hat{y} \rangle & \langle \Delta\hat{x}\Delta\hat{p_y} \rangle \\ \langle \Delta\hat{p_x}\Delta\hat{y} \rangle & \langle \Delta\hat{p_x}\Delta\hat{p_y} \rangle \end{bmatrix} \tag{3.27}$$

$$V_{22} = \begin{bmatrix} \langle \Delta\hat{y}^2 \rangle & \frac{1}{2}\langle \{\Delta\hat{y}, \Delta\hat{p_y}\} \rangle \\ \frac{1}{2}\langle \{\Delta\hat{y}, \Delta\hat{p_y}\} \rangle & \langle \Delta\hat{p_y}^2 \rangle \end{bmatrix} \tag{3.28}$$

The 2×2 matrices V_{11} and V_{22} can be recognized individually as variance matrices for the variables, $\Delta\hat{x}$ and $\Delta\hat{y}$ or the matrices for two separate single modes. For V_{11},

$$V_{11} = \begin{pmatrix} \langle \Delta\hat{x}^2 \rangle & \frac{1}{2}\langle \{\Delta\hat{x}, \Delta\hat{p_x}\} \rangle \\ \frac{1}{2}\langle \{\Delta\hat{x}, \Delta\hat{p_x}\} \rangle & \langle \Delta\hat{p_x}^2 \rangle \end{pmatrix}$$

thus,

$$\begin{aligned} detV_{11} &= \langle \Delta\hat{x}^2 \rangle \langle \Delta\hat{p_x}^2 \rangle - \frac{1}{4}\left(\langle \{\Delta\hat{x}, \Delta\hat{p_x}\} \rangle\right)^2 \\ &= \langle \Delta\hat{x}^2 \rangle \langle \Delta\hat{p_x}^2 \rangle - \frac{1}{4}|\langle \{\Delta\hat{x}, \Delta\hat{p_x}\} \rangle|^2 \end{aligned} \tag{3.29}$$

It should be noted that for two hermitian operators $\Delta\hat{x}$ and $\Delta\hat{p_x}$,

1. $\{\Delta\hat{x}, \Delta\hat{p_x}\}$ is always hermitian i.e.,

$$\{\Delta\hat{x}, \Delta\hat{p}_x\}^\dagger = \{\Delta\hat{x}, \Delta\hat{p}_x\} \tag{3.30}$$

2. $[\Delta\hat{x}, \Delta\hat{p}_x]$ is always anti-hermitian i.e.,

$$[\Delta\hat{x}, \Delta\hat{p}_x]^\dagger = -[\Delta\hat{x}, \Delta\hat{p}_x] \tag{3.31}$$

The proof for the uncertainty principle for the above mentioned operators, derived by using the Schwarz inequality has been given in APPENDIX B.3. From Eqs. (3.29) and (B.31) now, it is evident that :

$$det(V_{11}) \geq \frac{\text{ƛ}^2}{4} \tag{3.32}$$

Similarly, by the same arguments, for the single mode variance matrix, V_{22}, $det(V_{22}) \geq \frac{\text{ƛ}^2}{4}$. Or so to say, any physically realizable variance matrix of a state is bound to obey this basic condition.

It is worth noticing that when the 2×2 matrix $V_{11/22}$ (V_{11} or V_{22}) has a (canonical) diagonal form,

$$V_{11/22} = \begin{bmatrix} \kappa & 0 \\ 0 & \kappa \end{bmatrix} \tag{3.33}$$

then the statement of uncertainty principle takes the following form :

$$\begin{aligned} det\left(V_{11/22}\right) &\geq \frac{\text{ƛ}^2}{4} \\ \Longrightarrow \kappa^2 &\geq \frac{\text{ƛ}^2}{4} \\ \Longrightarrow \kappa &\geq \frac{\text{ƛ}}{2} \end{aligned} \tag{3.34}$$

Remark 3.1. *From Eqn.* (3.34)*, one gets the following equivalent statement for the uncertainty principle:*

$$\kappa - \frac{\text{ƛ}}{2} \geq 0 \tag{3.35}$$

3.2.4 Computation of Physically Significant Parameters from V

In the present subsection, the calculation of physically significant parameters such as symplectic eigen-values and twist from the given variance matrix (V) has been discussed. Also a distance measurement criterion between two variance matrices has been proposed.

3.2.4.1 *(i) Symplectic Eigen-values*

A real linear transformation on the variables $\hat{\xi}$ with a 4×4 real matrix S such that,

$$\hat{\xi} \to \hat{\xi}' = S\hat{\xi} \tag{3.36}$$

is considered. This transformation Eqn. (3.36) is canonical iff $\hat{\xi}'$ obeys the same commutation relationships as do $\hat{\xi}$. This restriction amounts to saying,

$$\beta = S\beta S^T \tag{3.37}$$

where, $S \in Sp(2n, R)$. Since, $n = 2$ is being considered here, $S \in Sp(4, R)$.

Eqn. (3.37) is the defining property for elements of the real symplectic group, $Sp(4, R)$. The symmetric symplectic transform of the 4×4 matrix V under such S is as follows :

$$V^{'} = SVS^{T} \tag{3.38}$$

If a given V is physically realizable, then so is its symplectic transform $V^{'}$ and the invertibility of S also guarantees the opposite statement. Therefore, in order to check realizability of a variance matrix, one needs to check the feasibility of the Symplectic transform of V. A simple (canonical) form for the same with only diagonal entries is guaranteed by the following *Williamson's Theorem*:

For any real symmetric positive-definite $2n \times 2n$ *matrix* V*, there exists an* $S \in Sp(2n, \mathbb{R})$ *such that the Symplectic transform of V by S has the canonical scaled diagonal form, unique upto the ordering of* κ_j*.*

For $n = 2$ case,

$$\begin{aligned} V^{''} &= SVS^{T} \\ &= \begin{bmatrix} \kappa_1 & 0 & 0 & 0 \\ 0 & \kappa_1 & 0 & 0 \\ 0 & 0 & \kappa_2 & 0 \\ 0 & 0 & 0 & \kappa_2 \end{bmatrix} \end{aligned} \tag{3.39}$$

Here, κ_1 and κ_2 are referred to as the *symplectic eigen values* of V.

The transformation expressed in Eqn. (3.39) is not a similarity transformation, hence, the eigen values of $V^{''}$ are not in general the eigen values of V. But the transformation :

$$\begin{aligned} \left(V^{''}\beta\right)^2 &= S\left(V\beta\right)^2 S^{-1} \\ &= -diag(\kappa_1^2,\, \kappa_1^2,\, \kappa_2^2,\, \kappa_2^2) \end{aligned} \tag{3.40}$$

is a similarity transformation, and so, the eigen values of $\left(V\beta\right)^2$ are the same as those for $\left(V^{''}\beta\right)^2$ or, $-\left(V\beta\right)^2 = -\left(V\beta\right)\left(V\beta\right)$ has a spectrum (of eigen values) i.e. $\kappa_1^2,\, \kappa_1^2,\, \kappa_2^2,\, \kappa_2^2$. Thus,one can evaluate the eigen values of $-\left(V\beta\right)^2$ in order to calculate the Symplectic eigen values.

Remark 3.2. *It can be seen in Eqn.* (3.39) *that the matrix* $V^{''}$ *is composed of two* 2×2

diagonal matrices, $\begin{bmatrix} \kappa_1 & 0 \\ 0 & \kappa_1 \end{bmatrix}$ *and* $\begin{bmatrix} \kappa_2 & 0 \\ 0 & \kappa_2 \end{bmatrix}$ *, which one can handle independently. Recalling Eqn.* (3.33)*, it is straightforward to see that for these diagonal matrices, one gets the following condition :*

$$\kappa_1, \kappa_2 \geq \frac{\lambda\!\!\!^{-}}{2} \tag{3.41}$$

The inequality (3.41) *is the uncertainty principle, which is the condition for physical possibility of* $V^{''}$ *and hence* V*.*

Remark 3.3. *The matrix* $V^{''} + i\frac{\lambda\!\!\!^{-}\beta}{2} = \begin{bmatrix} \kappa_1 & i\frac{\lambda\!\!\!^{-}}{2} & 0 & 0 \\ -i\frac{\lambda\!\!\!^{-}}{2} & \kappa_1 & 0 & 0 \\ 0 & 0 & \kappa_2 & i\frac{\lambda\!\!\!^{-}}{2} \\ 0 & 0 & -i\frac{\lambda\!\!\!^{-}}{2} & \kappa_2 \end{bmatrix}$ *has a spectrum of eigen values* $\kappa_j \pm \frac{\lambda\!\!\!^{-}}{2}$*, with* $j = 1, 2$*.*

From Eqn. (3.41)*,* $\kappa_1,\ \kappa_2 \geq \frac{\lambda\!\!\!^{-}}{2}$*. This implies,* $\kappa_1 \pm \frac{\lambda\!\!\!^{-}}{2},\ \kappa_2 \pm \frac{\lambda\!\!\!^{-}}{2} \geq 0$*. Therefore, the matrix* $V^{''} + i\frac{\lambda\!\!\!^{-}\beta}{2}$ *is positive semidefinite. It is known that, for the relation* $V^{''} + i\frac{\lambda\!\!\!^{-}\beta}{2} = S\left(V + i\frac{\lambda\!\!\!^{-}\beta}{2}\right)S^T$*, the positive semi-definiteness of* $V^{''} + i\frac{\lambda\!\!\!^{-}\beta}{2}$ *implies the positive semi-definiteness of* $V + i\frac{\lambda\!\!\!^{-}\beta}{2}$*. Therefore, the statement of the uncertainty principle, expressed in Eqn.* (3.41) *can also be written as:*

"A real symmetric positive-definite $2n \times 2n$ *matrix* V *(with,* $n = 2$ *for our case), is a bonafide variance matrix if and only if the Hermitian matrix* $V + i\frac{\lambda\!\!\!^{-}\beta}{2}$ *is positive semidefinite i.e.:* $V + i\frac{\lambda\!\!\!^{-}\beta}{2} \geq 0$*."*

3.2.4.2 *(ii) Twist parameter* (τ)

The twist parameter is defined as:

$$\tau = \frac{1}{\lambda\!\!\!^{-}}\left(\langle \hat{x}\hat{p_y}\rangle - \langle \hat{y}\hat{p_x}\rangle\right) \tag{3.42}$$

So that when the variance matrix has been defined with the variables $\Delta\hat{x} = \hat{x} - \langle\hat{x}\rangle$ and $\Delta\hat{p_x} = \hat{p_x} - \langle\hat{p_x}\rangle$, as is for the above discussed case, the twist parameter is defined as:

$$\tau = \frac{1}{\lambda\!\!\!^{-}}\left(\langle \Delta\hat{x}\Delta\hat{p_y}\rangle - \langle \Delta\hat{y}\Delta\hat{p_x}\rangle\right) \tag{3.43}$$

3.2.4.3 *(iii) Distance Measure between two Variance Matrices*

The inspiration defining the distance measure between two variance matrices, is drawn from already known *measure of non-Gaussian character of a quantum state*, defined in *Genoni et al. (2007)* as:

$$\begin{aligned} \delta &= \frac{Tr\left[(\rho-\tau)^2\right]}{2Tr\left(\rho^2\right)} \\ &= \frac{\frac{Tr\left[(\rho-\tau)^2\right]}{2}}{\frac{Tr(\rho^2)+Tr(\rho^2)}{2}} \end{aligned} \tag{3.44}$$

In (3.44), $\frac{Tr\left[(\rho-\tau)^2\right]}{2}$ denotes the square Hilbert-Schmidt distance between two Gaussian states (ρ and τ). Further, $Tr(\rho^2)$ represents the purity of the Gaussian state ρ.

Along similar lines, a distance (V_δ) between two given variance matrices V_1 and V_2 is defined as follows:

$$V_\delta = \frac{\frac{Tr\left[(V_1-V_2)^2\right]}{2}}{\frac{Tr\left(V_1^2\right)+Tr\left(V_2^2\right)}{2}} = \frac{Tr\left[(V_1-V_2)^2\right]}{Tr(V_1)^2+Tr(V_2)^2} \tag{3.45}$$

Here, $\frac{Tr\left[(V_1-V_2)^2\right]}{2}$ has been normalized with the average, $\frac{Tr(V_1)^2+(V_2)^2}{2}$.

It must be noted that either V_1 and V_2 are two separate 4×4 variance matrices or $V_1 = V_{11}$ and $V_2 = V_{22}$ as defined in Eqs. (3.26) and (3.28).

The importance of the proposed distance measure (V_δ) can be realized in the following manner:

1. The quantity V_δ can be used, to compare two wave-fields at the level of the second moments. If the two wave-fields are identical, then $V_\delta = 0$, and if the two wave-fields are not identical, then $0 \leq V_\delta \leq 1$.

2. The asymmetry measurement criterion: Assuming $V_1 = V_{11}$ and $V_2 = V_{22}$, $V_\delta \equiv V_{as}$ can also be used to capture the asymmetry of a wave-field in the x and y variables in the following manner:

   - If the wave-field in consideration is symmetric, one gets $V_{as} = 0$.
   - If the wave-field is asymmetric in variables x and y, then $0 \leq V_{as} < 1$.

In the upcoming section now, the details of our experiment done have been given. The

estimation of Variance matrices and other derivable quantities (mentioned in the previous Section) of a wave-field that has propagated either once (single passage) or twice (double passage) through a PRPP is done by using the Shack-Hartmann-Wavefront-Sensor (SHWFS). The experimental details are preceded by a description of the SHWFS.

3.3 Details of the Experiments

The Variance matrix calculations and also the changes in derivable physical quantities mentioned previously are done for two cases :

1. A free propagating beam.

2. A beam which has propagated either once or twice through the PRPP.

For both the above mentioned cases, the Variance matrix calculations are performed at various propagation distances and the achieved results are studied. The detecting system used for the purpose (i.e the SHWFS) is first described in the next Section and then the experimental details are presented.

3.3.1 The Shack-Hartman-Wavefront-Sensor

The Shack-Hartman-Wavefront-Sensor (SHWFS) Figure 3.1 is a widely used device for indirect wavefront measurements *Geary (1995)*. Originally conceived for imaging of astronomical objects through Earth's atmosphere, it has proved its worth in measuring wavefront aberrations introduced by many optical media in the path of propagating beams. SHWFS can optimize the wavefronts of laser sources dynamically. It also has the capability of characterizing the wavefront distortions if any in the incoming wave-field and can be used to provide real-time feedback for the control of adaptive optics.

A SHWFS usually consists of a CCD camera coupled in front with a lenslet array made up of converging microlenses. This array is designed such that the focal length of all the lenses forming the array is equal. The CCD surface is placed right at their focal point.

Figure 3.2 shows the 2D view of the layer of lenslet array and the CCD surface. In this figure, the diagram to the left shows an incoming ideal plane wavefront impinging

Figure 3.1: A Thorlabs Shack-Hartman-Wavefront-Sensor

on the CCD surface and that to the right shows an incoming distorted wavefront. The shift of the focal points from their ideal positions is apparent.

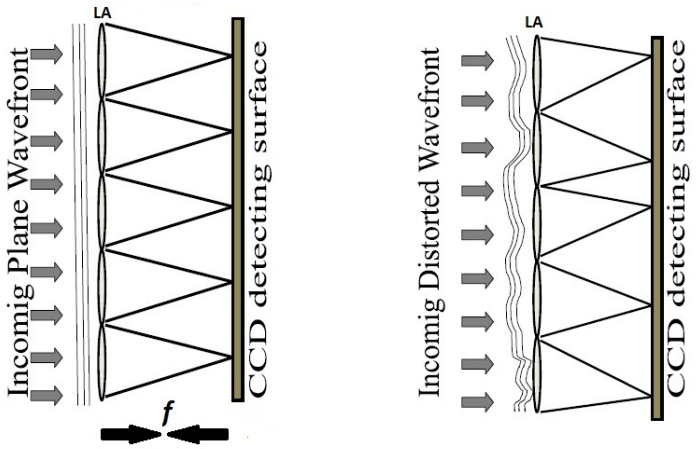

Figure 3.2: 2D View of a Layer of Lenslet Array (LA) and the CCD Surface

Figure 3.3 on the other hand shows, a single lenslet. The position shift of the spot from ideal plane wavefront spot is measured as $x_c - x_r$ where x_c and x_r are to be understood as any of x or y coordinates and the subscripts c and r indicate centroid and the reference respectively, in which case $\frac{x_c - x_r}{f}$ gives the angle β or the slope/gradient of the incoming distorted wavefront. Also, Figure 3.4 shows the pixelated CCD surface which gets divided into domains according to the size of the lenslets. Frame (a) in this figure shows the intensity spot pattern distribution from an impinging ideal plane beam

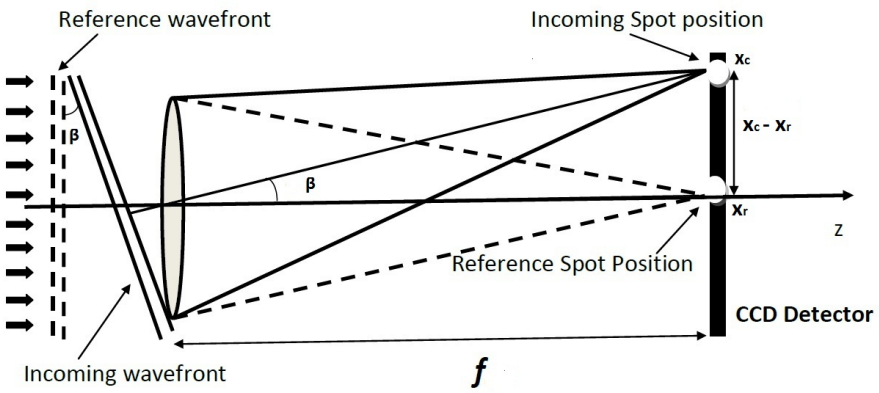

Figure 3.3: One Lenslet

with a plane wavefront and frame (b) shows that from a distorted beam.

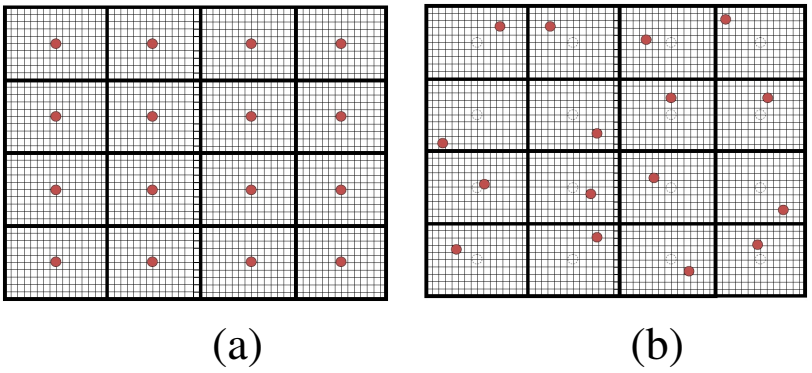

Figure 3.4: CCD Surface Divided into Domains

When an incoming ideal plane beam impinges on the lenslet array system, an array of spots is formed on the CCD surface (one in each domain). The spot centroid of each spot is located right into the middle of each domain. If the incoming wavefront on the other hand, is distorted, the spot centroids shift from their ideal positions in their respective domains (Figure 3.4). This shift is actually the wavefront slope/gradient corresponding to the wavefront portion seen in that domain and can be subsequently determined by subtracting the ideal reference spot position from the shifted spot position and further dividing the result by focal length of the microlenses. In order to reconstruct the wavefront, these gradients (calculated in each domain for both transverse coordinates) can be integrated in the 2 dimensions. Thus, the working principle of this instrument is based on the fact that spot deviations or displacements from ideal spot positions are a measure of wavefront slope or gradient of incoming wavefront.

Figure 3.5 now, sums up the working principle of a SHWFS *Courtesy (2011)*. The first undulating red layer in the Figure represents a distorted incoming wavefront impinging on the second layer of lenslet array system made up of plano convex lenses. This lenslet array system (or the microlens array (MLA)) divides the incoming wavefront and the total intensity into small domains, each of size equal to one lenslet and acts to collect and focus the respective local intensities into spots in each domain as has been shown in the third layer. The zoomed in version of one single domain has been shown in the figure to the right, wherein the shift of spot (to coordinates x_c, y_c) from its ideal coordinates x_r,y_r has been shown. The slope is measured as angle β. The fourth or the last layer (in the left diagram) shows the intensity distribution in one of the domains.

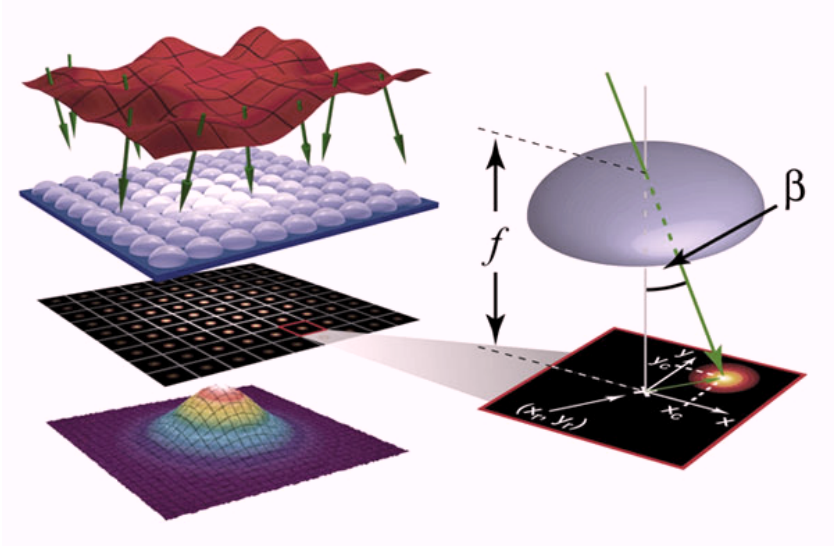

Figure 3.5: Working Principle of a Shack-Hartman-Wavefront-Sensor

For the present experimental purpose, a Thorlabs Shack-Hartmann-Wavefront-Sensor WFS150-5C has been used. In WFS150-5C, each lenslet is of size $150\,\mu m$. The lenslet array system is collectively referred to as the microlens array MLA. The gap between two microlenses is covered with a chrome mask, which prevents light going in between the microlenses directly to the CCD detector. This arrangement is done to increase the image contrast of the detected spot pattern and to improve the instrument accuracy, especially in case of strong wavefront deformations Figure 3.4.

According to the manufacturer (Thorlabs) *Thorlabs (2010)*, the lenslets used in WFS 150-5C, have been made from fused silica for transmission characteristics from the deep UV to IR and have a plano-convex shape, that allows nearly refraction limited spots. The lenses have been formed using photolithographic techniques based on semi-

conductor processing technology, which allows for excellent uniformity in the shape and position of each microlens. The MLA150-5C has a chrome mask that blocks light from being transmitted unless it goes through a microlens and therefore increases image contrast.

In Figure 3.6, a lenslet array, from microscopic view to the naked eye view (mounted in a SHWFS) has been shown sequence wise. The first frame in Figure 3.6 shows the mechanism of focusing done by the microlens array MLA150-5C, the next frame towards the right shows an unmounted microlens array, then further frames towards the right respectively show the mounted microlens array, in a specially designed mount and then inside SHWFS.

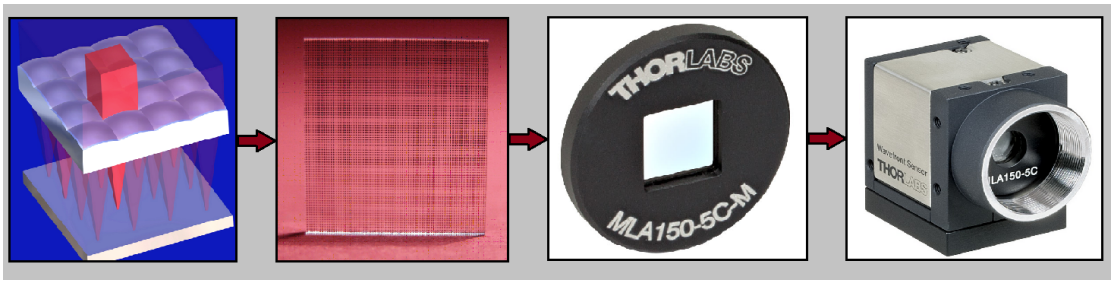

Figure 3.6: Microlens Array Unmounted and Mounted

The specifications for the Camera and the microlens array of MLA150-5C have been shown in the tables (D.1) and (D.2) *Thorlabs (2010)* in APPENDIX D.

In SHWFS, the spot intensity measurements in each domain are done by calculating the summation of intensity over all pixels present in that domain. Say, if each domain is labeled by indices i, j, then a pixel in that domain can be labeled by k. Therefore, the spot intensity in that domain would be:

$$\sum_{k} N_{ij}^{k} = I_{ij} \tag{3.46}$$

where, k is the pixel index of $(i,j)^{th}$ domain going from 1 to the total pixel number in that domain and N is the intensity value stored by the SHWFS in k^{th} pixel of $(i,j)^{th}$ domain. Figure 3.7 shows, a portion of the pixelated CCD surface divided into domains (in accordance with the MLA used). The top left domain shows the displaced spot centroid with local coordinates (x_c, y_c) shown with respect to the ideal plane wavefront spot centroid coordinates, (x_r, y_r). As can be seen, the domains are labeled in terms of

i, j with both i and j going from 1 to 31. The domain labeling in terms of indices i, j has been shown in the picture. Each pixel in one domain contributes to the calculation of the detected spot's intensity in that domain and is labeled as k, with k going from 1 to total pixel number in that domain.

It should be noted that the conventional x direction in Euclidean coordinate system coincides with the increasing j index or column index in SHWFS CCD grid and similarly, the conventional y direction coincides with the decreasing row index in the grid.

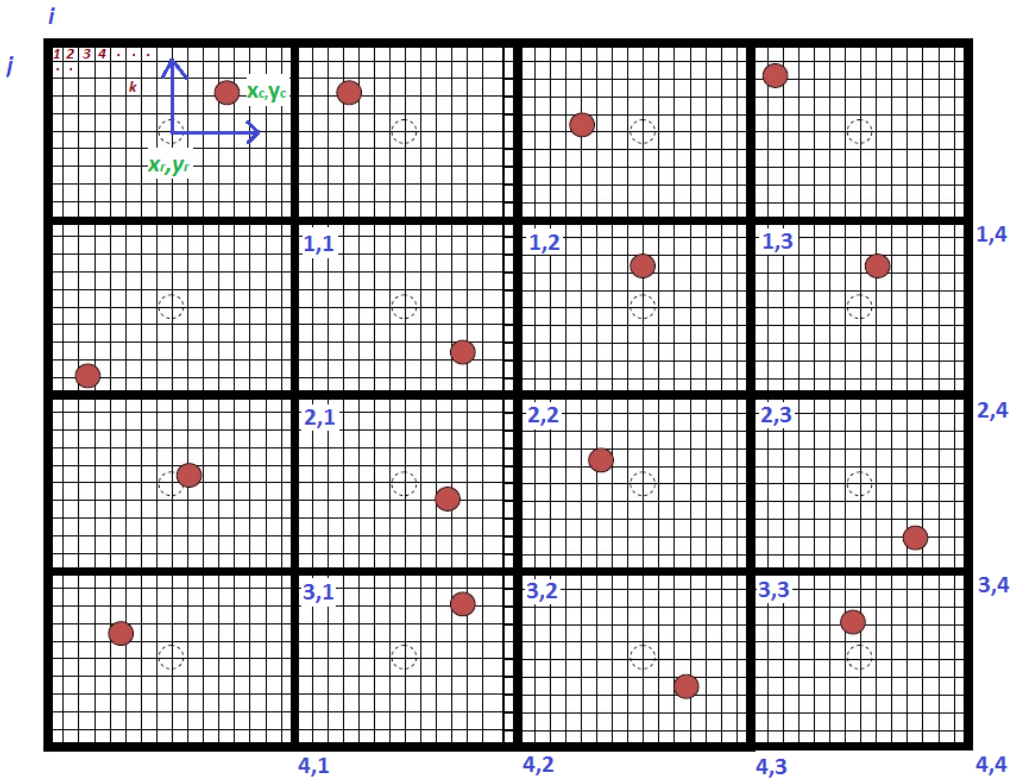

Figure 3.7: SHWFS Grid

The area of the detectable spots in Thorlabs SHWFS is selectable as has been shown in fig. 3.8. Out of 39×31 available domains, a 31×31 square domain grid has been selected, so that in the present case, $i, j = 1$ to 31. Figure 3.8 shows the (selectable) available detection surface areas in Thorlabs SHWFS (MLA150-5C). 1024×1024 pixels corresponding to 4.76×4.76 mm area has been selected. Thus, the used domains have been restricted to 31×31 as against the maximum available 39×31 corresponding to 5.95×4.76 mm area.

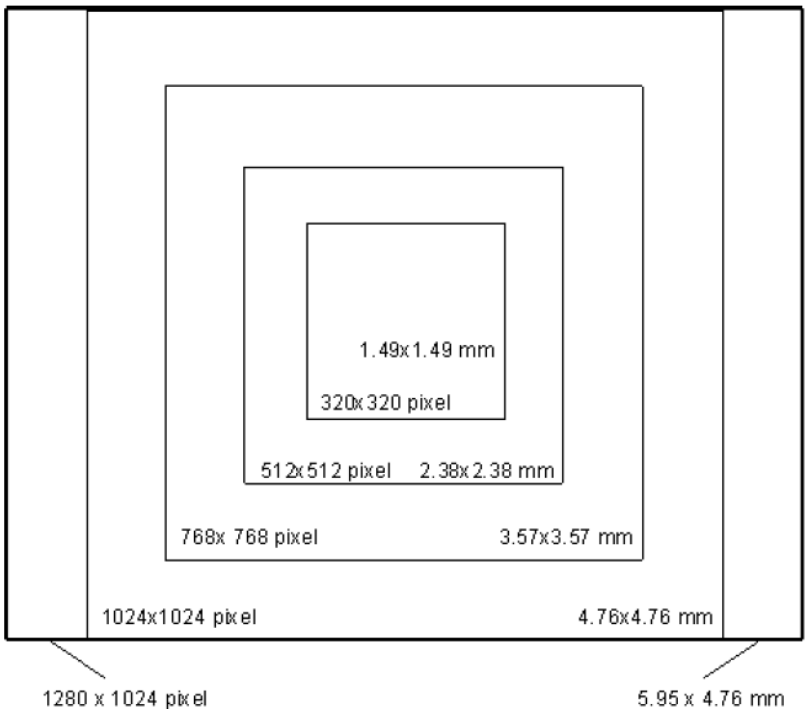

Figure 3.8: Selectable Detection Areas in Thorlabs SHWFS (MLA150-5C)

The slope or gradient of wavefront is related to the spot shift in one particular domain as:

$$\begin{aligned} \frac{x_{c_{ij}} - x_{r_{ij}}}{f} &= \lambda\!\!\!^{-}\frac{\partial\phi(x,y)}{\partial x}\,, \\ \frac{y_{c_{ij}} - y_{r_{ij}}}{f} &= \lambda\!\!\!^{-}\frac{\partial\phi(x,y)}{\partial y}\,, \end{aligned} \tag{3.47}$$

Schäfer and Mann (2002) where, $\lambda\!\!\!^{-}$ is $\frac{\lambda}{2\pi}$ with $\lambda = 633\,\mathrm{nm}$. In order to make a global coordinate system, for the calculation of slopes, both the coordinate axis are appropriately translated and rotated so that the center of the selected 31×31 CCD grid is the coordinate $(0, 0)$, with all pixel units converted to millimeters and the focal length f is the effective focal length i.e. 3.7 mm of MLA.

Also, the centroid coordinates of the ideal plane beam, $x_{r_{ij}}, y_{r_{ij}}$ are calculated using the fact that for ideal plane beam, these lie at exact centre of their respective domains. Knowing all this, the slope of the impinging distorted wavefront with respect to the ideal plane wavefront is effectively calculated.

Using the expressions in Eqs. (3.47), the modified entries of the Variance matrix are calculated. These have been given in APPENDIX C in Section C.2. The experiment

performed for Variance matrix estimation in different situations using the SHWFS has been presented in the following section.

3.3.2 Experiment for Single Passage through PRPP

The schematic of Figure (3.9) shows the single passage geometry of the experiment. It has been performed in two procedures. In the first procedure or Procedure A, a TEM_{00} wave-field of wavelength 633 nm and $12\,\mathrm{mW}$ power from a He-Ne laser source is attenuated using three neutral density filters and is then allowed to propagate for a distance d before getting detected by SHWFS. The distance d is varied from 34 to $74\,\mathrm{cm}$ at an interval of $2.5\,\mathrm{cm}$, and the Variance matrix, estimated for more than 300 wave-field samples of this wave-field at each distance.

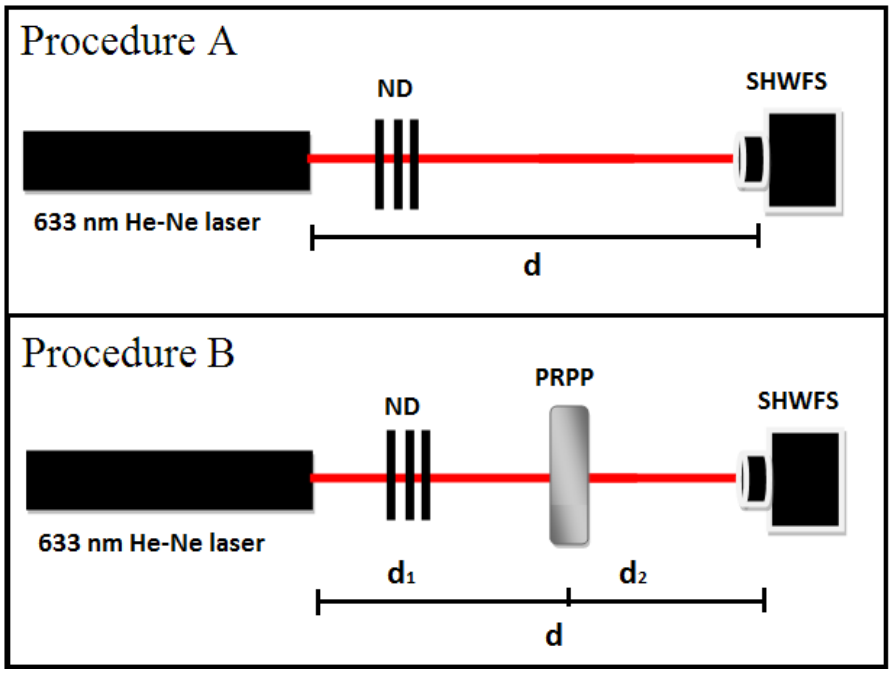

Figure 3.9: The Experimental Scheme for Single Passage

In the second procedure or Procedure B, PRPP (PRPP_2) is introduced at a distance $d_1 = 24\,\mathrm{cm}$ from the laser source and as in the first procedure, the SHWFS is placed at a distance d from the laser source, and the Variance matrices of the wave-field samples are estimated at each distance. Note that the distance of the SHWFS from PRPP denoted by d_2 in Figure (3.9) is such that $d_1 + d_2 = d$. To generate the wave-field samples, the inserted PRPP is rotated at a speed of 0.0104 rotations per second, and the recordings are made with the SHWFS exposure time set at $0.079\,\mathrm{msec.}$ with a maximum frame rate

of $15\,\mathrm{Hz}$.. The second sample reading for beam centroids and intensities from SHWFS is collected at $66.779\,\mathrm{msec.}$ after the first one. And, for all practical purposes, the PRPP is deemed stationary with regard to the SHWFS measuring time scales.

Of the measured Variance matrices, not all of them are found to obey the uncertainty principle listed in Eqn. (B.28). This may be attributed to the discretisation of the measured moments Eqs. (C.15)-(C.25). Only the Variance matrices which obey the uncertainty principle are taken into account.

From the Variance matrix calculations at different distances, the Twist parameter Eqn. (3.43), the Symplectic eigen values Eqn. (3.39) and the distance measure between two Variance matrices Eqn. (3.45) is calculated. The results obtained have been presented in the following subsection.

3.3.3 Results and Analysis

In Figure (3.10), in frame (a), the values of Twist parameter measured at distance $d = 64\,\mathrm{cm}$ for 300 samples have been shown. Frame (a) shows the measured values of the Twist parameter (at $d = 64\,\mathrm{cm}$) in black color for the first part of the experimental procedure, in which the PRPP was not inserted in the laser wave-field path. The measured Twist values for the second part of the experimental procedure wherein the PRPP was inserted at $d_1 = 24\,\mathrm{cm}$ have been shown in red color. Clearly, there is noticeable enhancement in the values of Twist for the second case. This has been illustrated

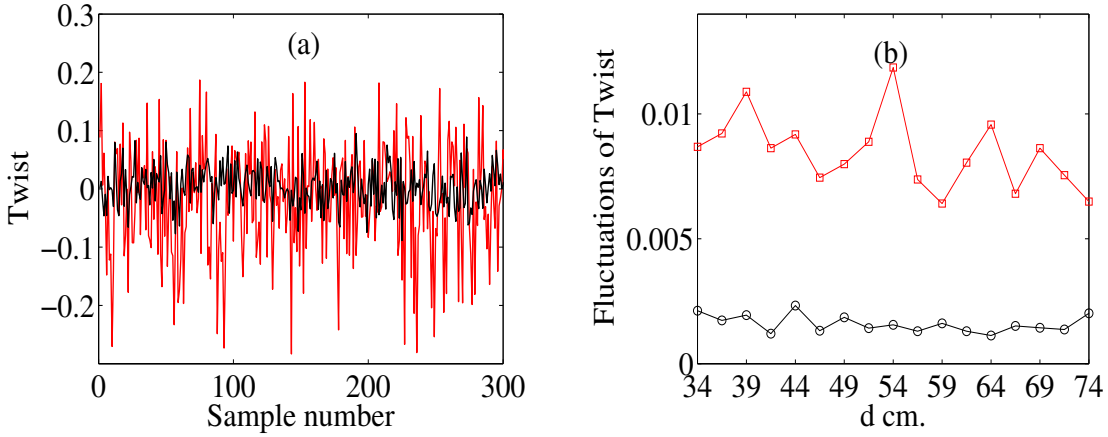

Figure 3.10: Results for Twist Parameter in the Single Passage Experiment

in Frame (b), which shows the plot of fluctuations of Twist with respect to mean val-

ues [1] for 300 samples at each d at an interval of $2.5\,\mathrm{cm}$, starting from $d = 34\,\mathrm{cm}$ for both the procedures of the experiment, i.e., with and without the insertion of the PRPP. Fluctuations of Twist with the insertion of PRPP at $d_1 = 24\,\mathrm{cm}$ are represented by $\square$, colored red and connected with red lines, and fluctuations of Twist without the insertion of PRPP are represented by $\circ$, colored black and connected by black lines. In a similar fashion, the smaller and larger Symplectic eigenvalues κ_1 and κ_2 have been analyzed in Figure (3.11).

Frames (a), (b) and (c) correspond to the smaller Symplectic eigenvalues κ_1, while frames (d), (e) and (f) correspond to the larger Symplectic eigenvalues κ_2. In frames (a) and (d), the Symplectic eigenvalues κ_1 and κ_2 have been plotted against the sample number (total 300 samples). These have been shown for $d = 64\,\mathrm{cm}$, and λ here has been set to 1. While frame (a) corresponds to the smaller Symplectic eigenvalue κ_1, (without and with the insertion of PRPP at $d_1 = 24\,\mathrm{cm}$), frame (d) corresponds to the larger Symplectic eigenvalue κ_2, (again without and with the insertion of the PRPP at $d_1 = 24\,\mathrm{cm}$). In both frames (a) and (d), the case where PRPP was not inserted has been shown in black and that where PRPP was inserted at $d_1 = 24\,cm$ from laser source has been shown in red.

The line $\kappa_1 = \frac{1}{2}$ in frame (a), and the line $\kappa_2 = \frac{1}{2}$ in frame (d), saturates the uncertainty principle. It can be seen from frames (a) and (d) that κ_1 and κ_2 are well above the saturating value $\frac{1}{2}$ (refer Eq. (3.34)), indicating the presence of higher order modes *Simon and Mukunda (2000)*, and this is even without the insertion of the PRPP. Also, clearly, there is an increase in fluctuations in the measured values of κ_1 and κ_2 with the insertion of the PRPP, and this has been captured in frames (b) and (e), where the fluctuations of κ_1 and κ_2 with increasing d have been plotted.

Here also, 300 samples were considered at each d at an interval of $2.5\,\mathrm{cm}$ starting from $d = 34\,\mathrm{cm}$. Fluctuations of κ_1 or κ_2 with the insertion of the PRPP, have been represented by $\square$, colored red (connected by red lines) and fluctuations of κ_1 or κ_2 without the insertion of the PRPP are represented by $\circ$, colored black and joined by black lines. In frames (c) and (f) the values of κ_1 and κ_2 estimated from the average Variance matrix evaluated for over 300 samples for each d have been plotted against increasing d (for both with and without the insertion of the PRPP cases).

[1] Fluctuation of a random variable X over N samples is given by $\frac{1}{N}\sum_N \left(X_N - \langle X\rangle\right)^2$, with $\langle X\rangle = \frac{1}{N}\sum_N X_N$

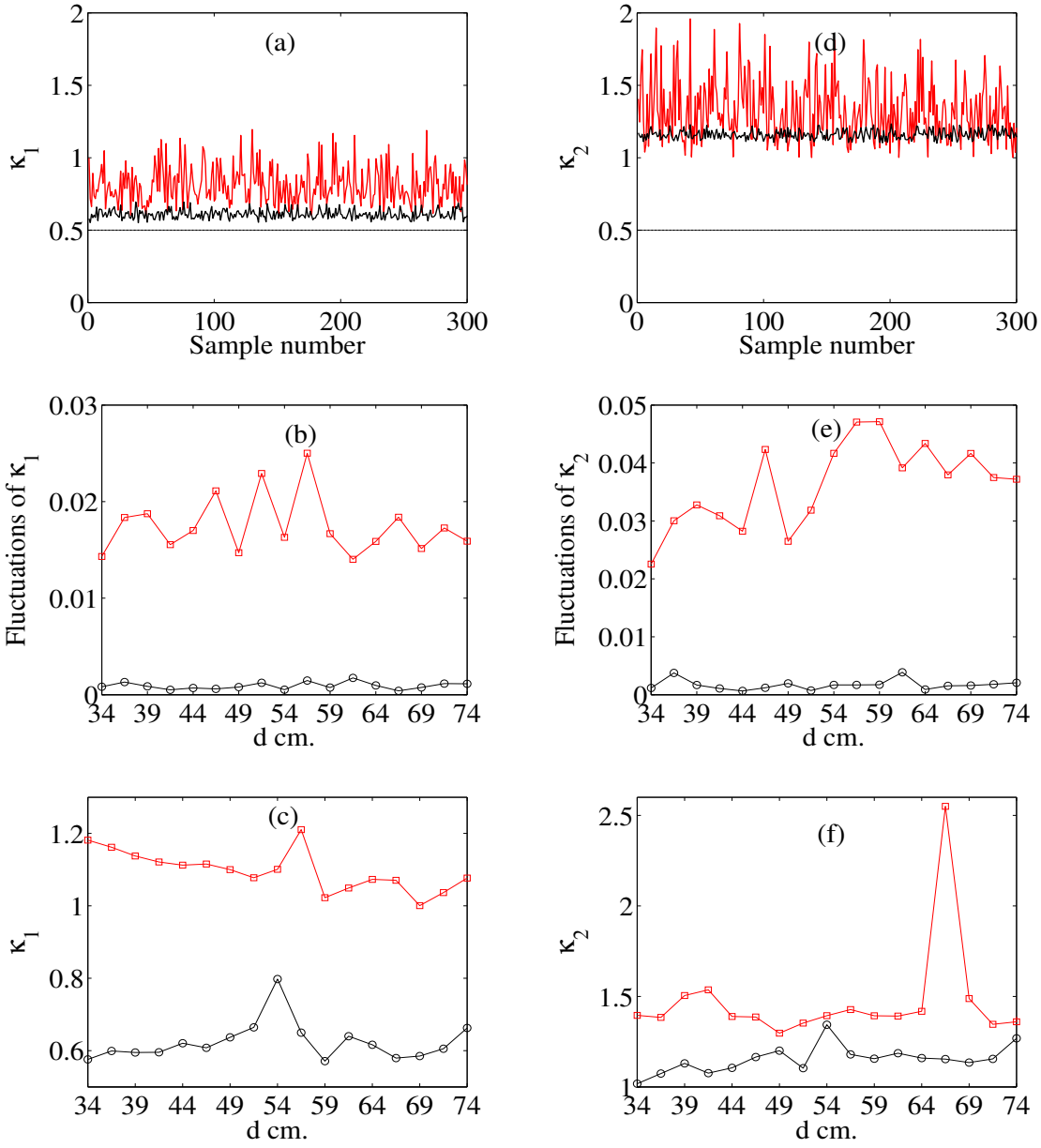

Figure 3.11: Results for κ_1 and κ_2 for Single Passage Experiment

Clearly there is an enhancement of the values of κ_1 and κ_2 on an average with the insertion of the PRPP, which is indicative of the increased presence of higher order modes on an average with the insertion of the PRPP.

Frame (a) of Figure (3.12) now shows the estimated values of the asymmetry parameter V_{as} for distance $d = 64\,\text{cm}$, for 300 samples, for both the cases, i.e. without the insertion of the PRPP, which has been shown in black color, and with the PRPP inserted at $d_1 = 24\,\text{cm}$, shown in red color. Frame (b) on the other hand, plots the fluctuations of V_{as} about its mean for an increasing d for both with and without insertion of the PRPP

at $d_1 = 24\,\mathrm{cm}$. Fluctuations of V_{as}, when the PRPP was not inserted have been represented by black $\circ$ connected with black lines and fluctuations of V_{as} with the insertion of the PRPP at $d_1 = 24\,\mathrm{cm}$ have been represented by red $\square$, connected with red lines. Frame (c) shows the average value of V_{as} estimated for 100 samples each for varying d. Black $\circ$ represents the average value of V_{as} when the PRPP was not inserted, and red $\square$ represents the average value of V_{as} with the insertion of the PRPP at $d_1 = 24\,\mathrm{cm}$.

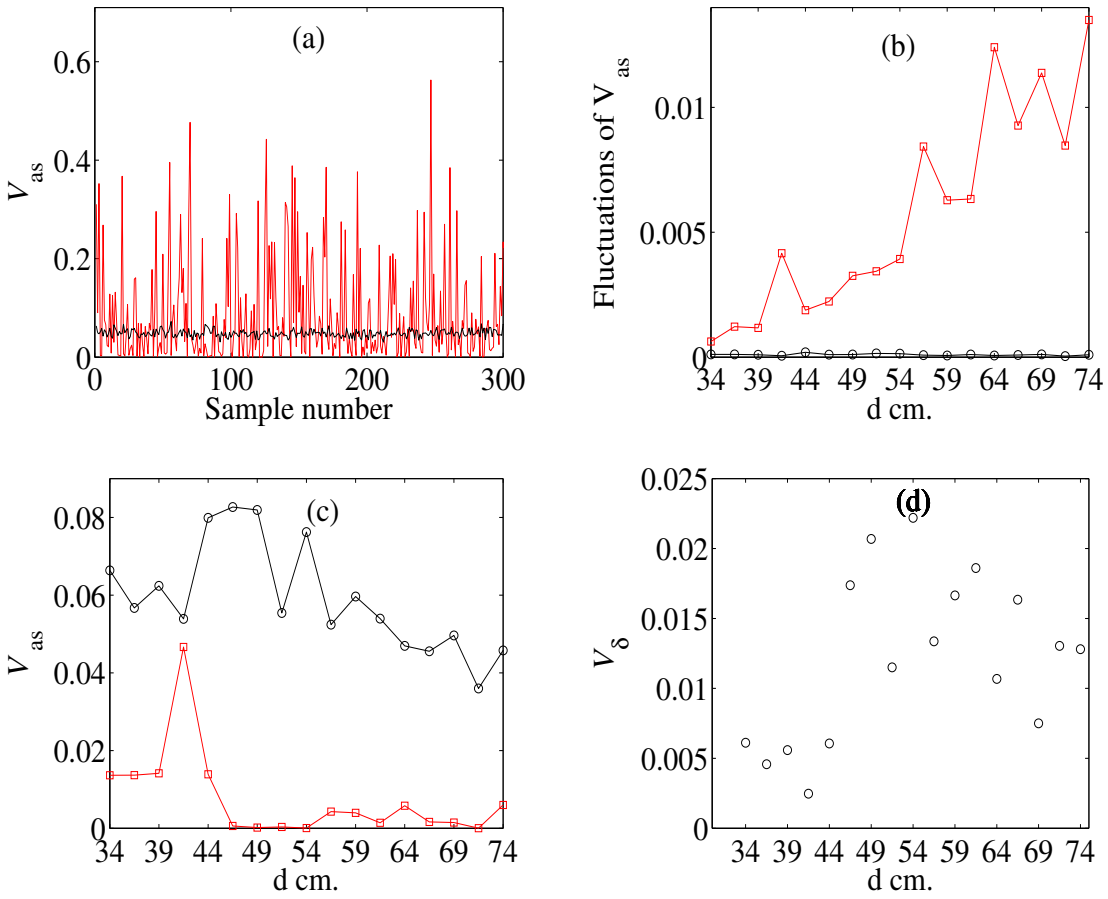

Figure 3.12: Results for V_{as} and V_{δ} in the Single Passage Experiment

An enhancement of fluctuation of wave-field asymmetry with the insertion of the PRPP can be clearly seen. Frame (b) of Figure (3.12), captures this enhancement by plotting the fluctuations of asymmetry parameter V_{as} is for increasing d at an interval of $2.5\,\mathrm{cm}$ starting from $d = 34\,\mathrm{cm}$. It can be seen that the fluctuations of asymmetry parameter are enhanced with increasing d. This may be contrasted with the plot in frame (c) where the V_{as} estimated from an average of 300 Variance matrices for each d has been plotted against increasing d.

Thus it is seen that, on an average, the asymmetry of wave-field decreases with the

insertion of the PRPP (as expected), even though the fluctuations of $V_{\rm as}$ are enhanced with the insertion of the PRPP as seen in frame (b). In frame (d) of Figure 3.12 a comparison of the measured Variance matrices obtained from the first and the second procedures of the experiment using the quantity V_δ has been done. Here V_1 corresponds to the average Variance matrix estimated at a particular distance d without the insertion of the PRPP, and V_2 to the average Variance matrix measured at the same distance d with the insertion of the PRPP at $d_1 = 24\,\mathrm{cm}$. As before d is incremented at an interval of $2.5\,\mathrm{cm}$ starting from $d = 34\,\mathrm{cm}$ and V_δ is calculated each time. The average in each instance is taken over 300 samples. The nonzero value of V_δ suggests that the wave-fields with and without the insertion of the PRPP are qualitatively different.

3.3.4 Experiment for Double passage through PRPP

Drawing inspiration from the interferometric schemes shown in Chapter 2, the Variance matrix calculations are performed for a beam which traverses twice through the PRPP, i.e. *double passage* through PRPP and the results achieved are again compared with those obtained for a free propagating beam.

In Figure 3.13 the experimental schemes for *double passage* geometry used for the said purpose have been shown. As can be seen, this geometry is inspired from the familiar Michelson's geometry with the transmissive arm blocked. Procedure A and Procedure B have been schematically shown in Figure 3.13 along with an equivalent diagram of Procedure B in which the double passage traversed through the PRPP has been shown in the manner of single passage, such that the beam which originally gets reflected by mirror (M), retracing its path is shown in the forward direction with a virtual repetition of components it encounters in its path.

It should be noted that here, the source is now considered at the beam splitter (BS) and the SHWFS is successively kept at distances $(39 + (d = 0))\,\mathrm{cm}$ to $(39 + (d = 20))\,\mathrm{cm}$ (incrementing in steps of $(39 + 2)\,\mathrm{cm}$) from the source, with the distance d being the incremental distance after $39\,\mathrm{cm}$ which is varied in steps of $2\,\mathrm{cm}$. The experiment is performed on similar lines of Section 3.3. The distance of SHWFS this time is incremented in steps of $2\,\mathrm{cm}$ and as usual the invalid Variance matrices are discarded based on uncertainty principle. The results achieved have been shown in the form of plots in the following subsection.

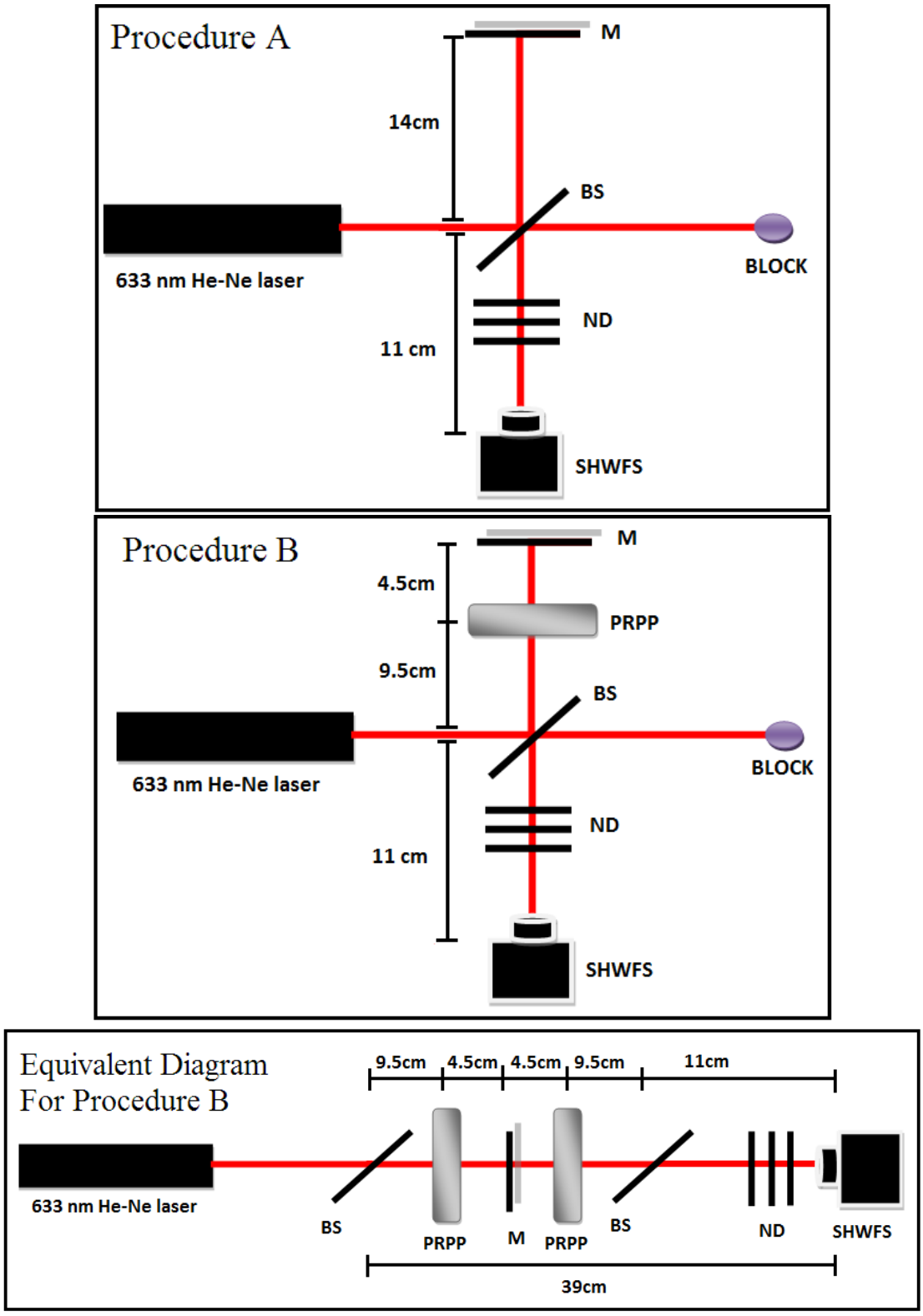

Figure 3.13: Double Passage through PRPP

3.3.5 Results and Analysis

In frame (a) of Figure 3.14, the Twist parameter values for a distance of $(39 + (d = 10))\,\mathrm{cm}$ have been shown. In frame (b) the same have been zoomed in for more visual clarity. The black colored lines in frame (a) and (b) are for the case where PRPP was not inserted in the double passage geometry and the red colored lines are for the case where the PRPP was inserted at a distance of $9.5\,\mathrm{cm}$ from the beam splitter (BS).

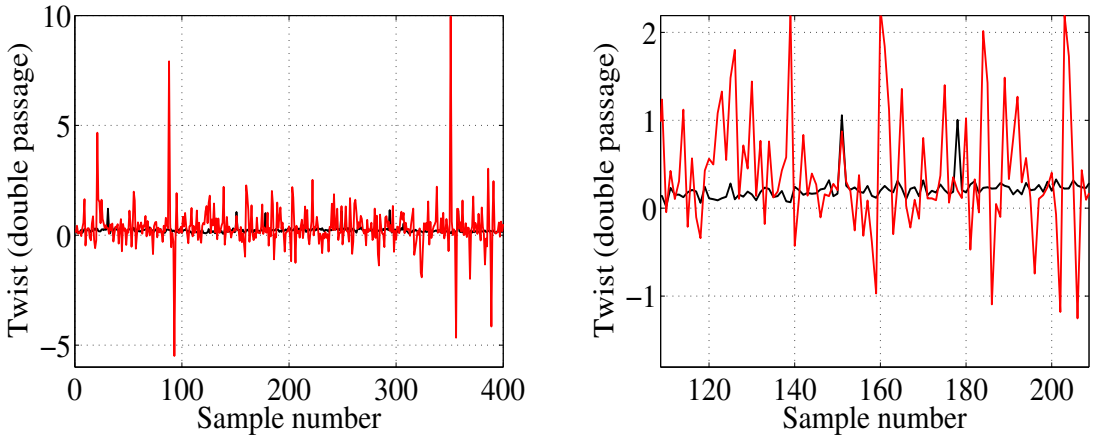

Figure 3.14: Twist parameter at $d = 10\,\mathrm{cm}$ for Double Passage Geometry

It is clear that there is an enhancement in the values of Twist on insertion of PRPP. Also, an offset value for twist (which is greater than zero) can be seen in both the frames (a) and (b). This can be attributed to some component in the experimental geometry (apart from the PRPP), which is providing an overall non-zero rotation to the beam.

Figure 3.15 on the other hand shows the Fluctuations of twist for double passage geometry for all the considered distances. Here, the black $\circ$ (joined by lines of the same color) are for no insertion of PRPP in this case and similarly the red squares $\square$ (joined by dotted lines of the same color) are for the case where the PRPP was inserted in between the source and the detector. The fluctuations of Twist are greater when PRPP is inserted, than when it is not inserted. It would be insightful to compare the Figures 3.14, 3.15 with those presented in Figure 3.10. The minimum and maximum fluctuations in Twist values presented in Figure 3.14 (a) are seen to be higher by more than an order as compared to the maximum and minimum values presented in Figure 3.10 (a). This clearly indicates that on a double passage through the PRPP, the random rotations

become even more pronounced. Similarly, the Fluctuations in Twist values shown in Figure 3.15 are more than 3 orders higher than those seen in Figure 3.14 (b).

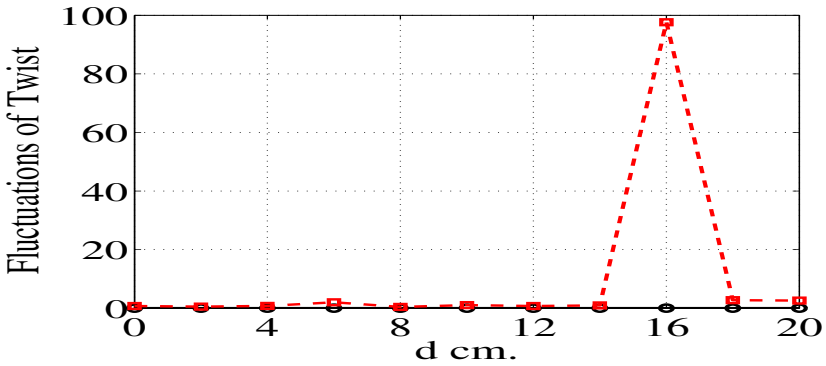

Figure 3.15: Fluctuations of Twist Parameter in the Double Passage Geometry

In Figure 3.16, in frame (a) and frame (b), the smaller and the larger symplectic eigen values, κ_1 and κ_2 respectively have been shown for a distance of $(39 + (d = 10))\,\mathrm{cm}$. The black colored lines in frame (a) and (b) are for the case where PRPP was not inserted and the red colored lines are for the case where the PRPP was inserted at a distance of $9.5\,\mathrm{cm}$ from the beam splitter (BS). In both these frames, the blue colored line drawn at κ_1 , $\kappa_2 = 0.5$, shows the saturating value of κs. It is seen from the above frames that there is a pronounced enhancement in the values of both κ_1 and κ_2 on insertion of PRPP when compared with those obtained when the PRPP was not inserted. A comparison of both these frames with frames (a) and (d) of Figure 3.11 hints towards the enhanced possibility of presence of higher order modes on a double passage through the PRPP.

Frame (c) and frame (d) show the Fluctuations of κ_1 and κ_2 respectively for the double passage geometry for all the considered distances. Here again, the black $\circ$ (joined by lines of the same color) are for no insertion of PRPP and similarly the red squares $\square$ (joined by dotted lines of the same color) are for the case where the PRPP was inserted in between the source and the detector. As expected, these fluctuations are higher when the beam travels twice through the PRPP. The order of fluctuations has increased by one order for κ_1 in comparison to that found in frame (b) of Figure 3.11 and for κ_2, it has jumped by four orders when compared with frame (d) of Figure 3.11.

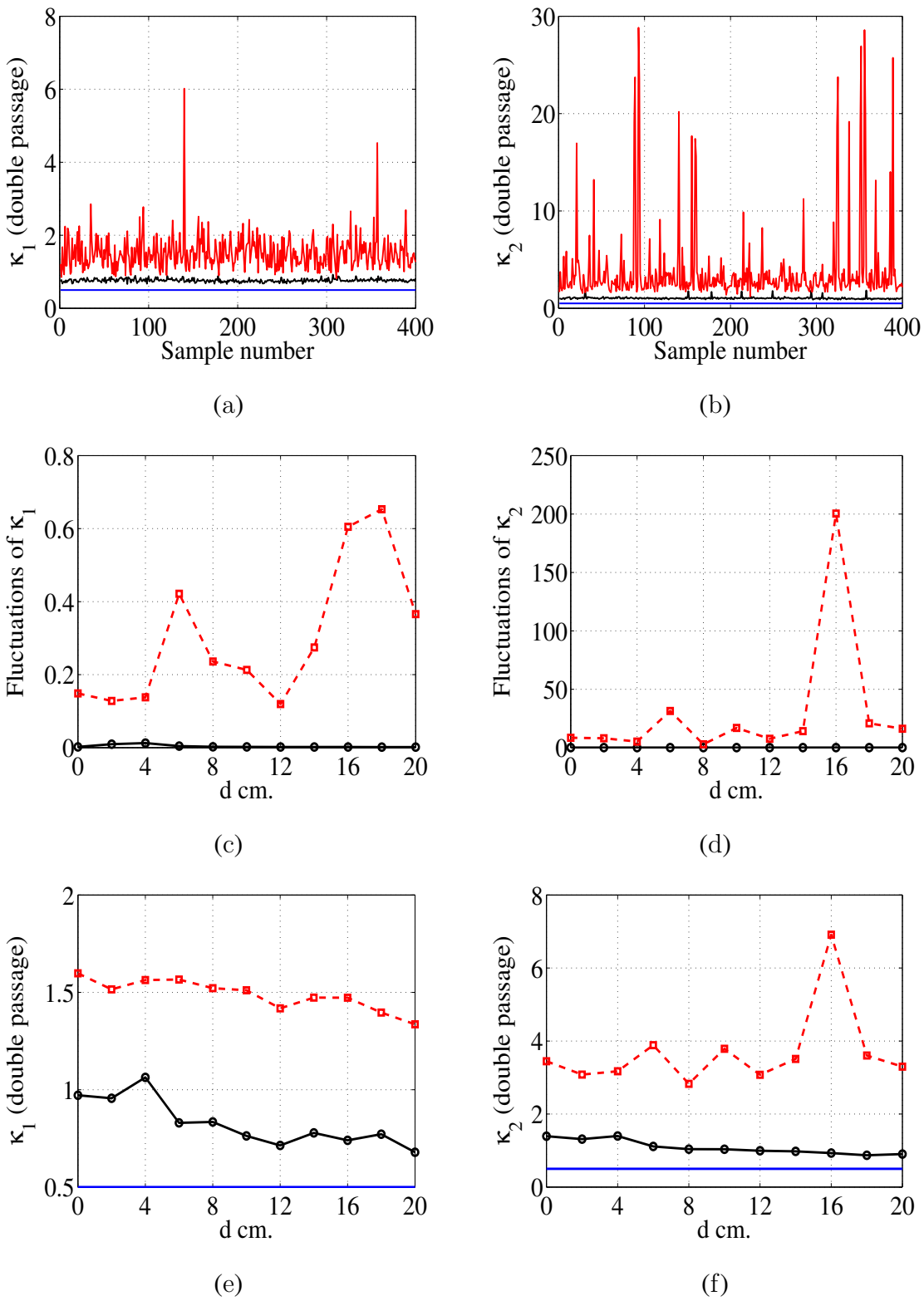

Figure 3.16: Results for κ_1 and κ_2 in the Double Passage Geometry

The two frames (e) and (f) of Figure 3.16, the mean values (calculated from a sample number of 400) of κ_1 and κ_2 respectively for all the considered distances have been shown. Here also, the black $\circ$ (joined by lines of the same color) are for no insertion of PRPP and similarly the red $\square$ (joined by dotted lines of the same color) are for the case where the PRPP was inserted in between the source and the detector. In these frames also, the blue colored line drawn at $\kappa_1,\ \kappa_2\ = 0.5$, shows the saturating value of κs. The mean values themselves (for both κ_1 and κ_2) show a marked increase if compared with those in frames (c) and (f) of Figur 3.11. The presence of higher order modes thus, is more pronounced when the beam traverses the said PRPP twice.

Figures 3.17 and 3.18 explore the distance measures $V_{\rm as}$ and V_δ respectively via the presented plots. Frame (a) of Figure 3.17 shows the calculated $V_{\rm as}$ from 400 Variance matrices for a distance of $(39\ +\ (d\ =\ 10))\,{\rm cm}$, and frame (b) shows the zoomed in version of the same. The color scheme for with and without the insertion of PRPP has not been changed. The pronounced increase in the beam asymmetry on the insertion of PRPP is clear. Frame (c) on the other hand shows the calculated $V_{\rm as}$ for an average of 400 Variance matrices, for both the cases for all distances. As usual the beam asymmetry decreases on an average with the passage through the PRPP. Frame (d) now, shows the Fluctuations of $V_{\rm as}$ calculated with a sample number of 400 Variance matrices at each of the considered distances.

Lastly, V_δ has been calculated with V_1 being the average Variance matrix for 400 samples, for the case where PRPP was inserted and V_2 being the average Variance matrix for 400 samples, for the case where PRPP was not inserted in double passage geometry. This has been shown in Figure 3.18. There is an order increase in the value of V_δ in Figure 3.18, when it is compared with frame (d) of Figure 3.12, i.e. to say, that the distance between two Variance matrices V_1 and V_2 increases further when V_1 represents the average Variance matrix for a beam that has traversed twice through the PRPP.

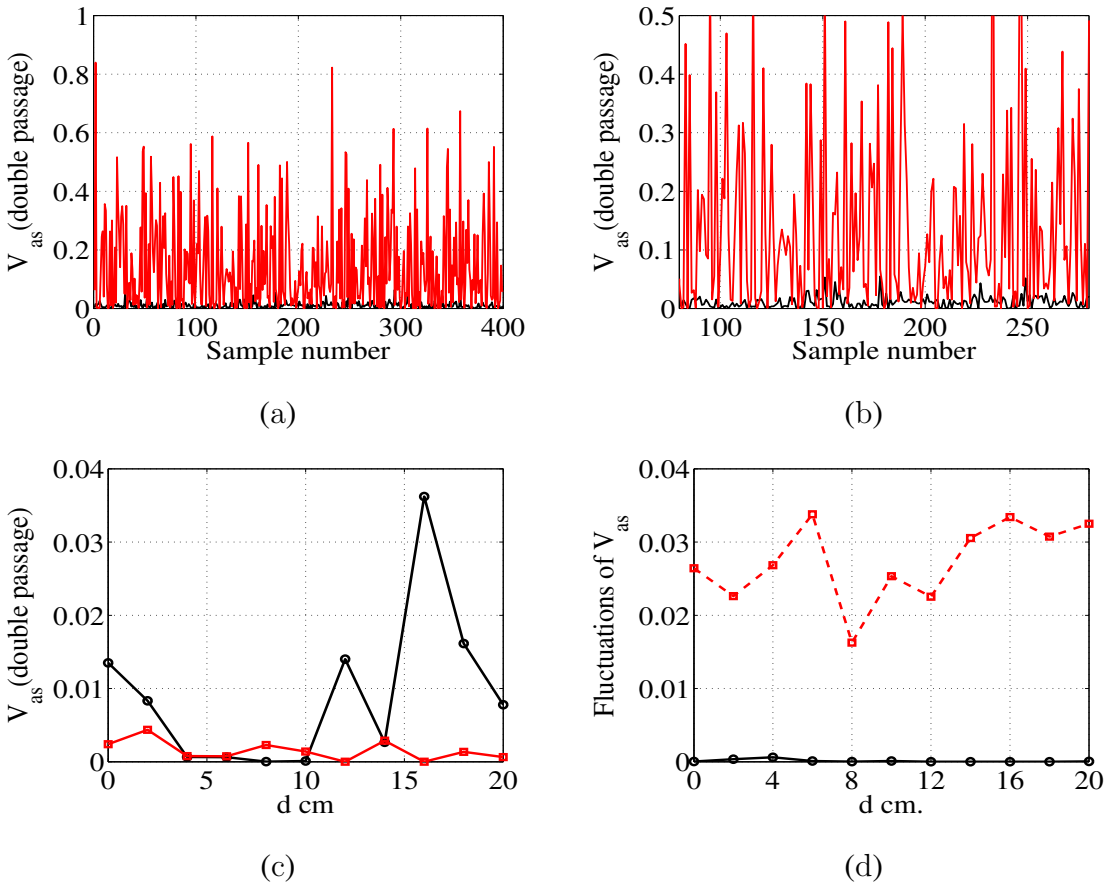

Figure 3.17: Results for V_{as} in Double Passage Geometry

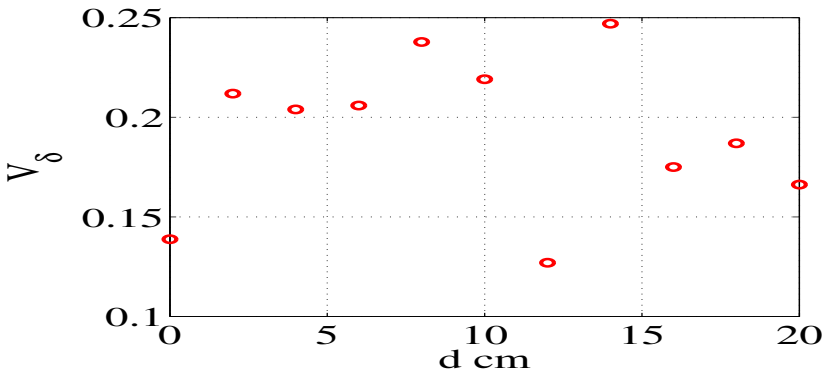

Figure 3.18: V_δ in the Double Passage Geometry

3.4 Summary

To summarize, a coherent wave-field on a single and double passage through a PRPP using the Variance matrix has been studied. The uncertainty principle has been used as a tool for discriminating the data. The quantities of physical interest such as the Twist parameter, the Symplectic eigenvalues, and the distance measure between two Variance matrices have been studied. It is found that there is an enhancement of fluctuations in all these parameters on the insertion of PRPP in both single and double passage cases, the fluctuations being more pronounced in latter case. Nevertheless, it is also seen that the wave-field asymmetry on an average decreases on such passages through PRPP. It is evident that this study can be applied to more general situations such as passage of a wave-field through atmospheric turbulence and other random media.

CHAPTER 4

Characterization of Pseudo-Random-Phase-Plate using Surface Roughness Measurement Parameters

4.1 Introduction

Previously in Chapter 2, the nature of Pseudo-Random-Phase-Plates (PRPPs) was determined by calculating the phase structure function from the extracted phase portions in interferometric experiments. It was also observed therein that the extracted phase portions (refer Figure 2.13 or 2.16) always resemble a rough surface. This motivates one to determine the nature of a PRPP by using *standard statistical parameters*, which are usually used for characterizing surface roughness. For this purpose, one can estimate such statistical parameters for the extracted phases from an interferometric experiment and compare them with those estimated for known, numerically generated Kolmogorov phase screens.

In the present chapter, one of the available PRPPs ($PRPP_2$, as referred in Chapter 2) is considered for such an investigation[1] and an attempt has been made to evaluate the nature of its turbulence regime (i.e. *non-Kolmogorov*) at a wavelength of 633 nm using the *standard statistical parameters*.

4.2 Experimental Procedure and Theory

The retrieved phase profiles of $PRPP_2$, obtained using coherent laser wave-field of 633 nm wavelength in the Mach-Zehnder interferometric set up with an additional $4f$ imaging system, are statistically compared with numerically generated Kolmogorov phase screens. The numerically generated phase screens are obtained using atmospheric structure constants ranging from very weak to very strong turbulence conditions.

[1] Note that the PRPP was characterized as a non-Kolmogorov turbulence simulator at 633 nm in Chapter 2

4.2.1 Experimental Arrangement

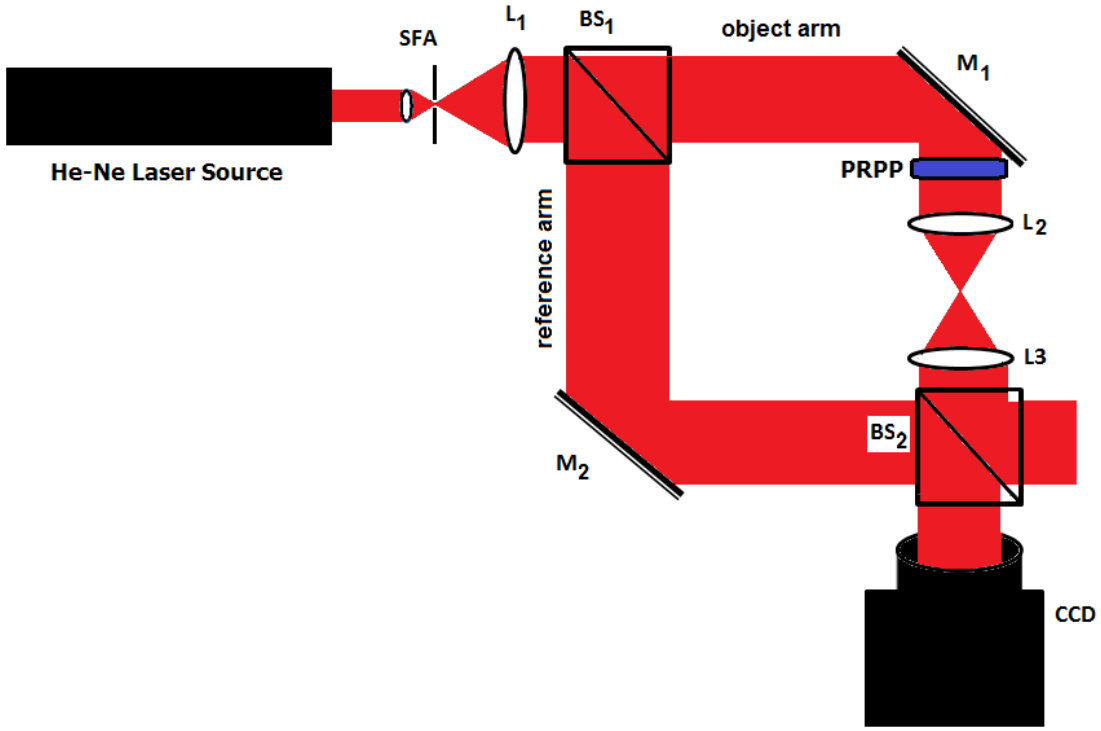

Figure 4.1: Mach-Zehnder Set-up

The experimental arrangement has been illustrated in Figure 4.1. Here, a 633 nm He-Ne laser beam with an output power of $12\,\mathrm{mW}$ is coupled with a spatial filtering assembly (SFA) and a collimating lens (L_1), giving a collimated beam with diameter of approximately $2\,\mathrm{cm}$ at the lens output. This beam further falls on beam-splitter, BS_1, which splits it into two equal intensity beams propagating at an angle of $90°$ with respect to each other. The beam going in line with the propagation direction of the unsplitted beam, is labeled the object beam, and the corresponding arm of the interferometric set up, the object arm (Figure 4.1). Similarly, the beam propagating perpendicular to the unsplitted beam is labeled the reference beam and the corresponding interferometric arm, the reference arm. The mirrors, M_1 and M_2 are both placed at equal distance with respect to the beam-splitter BS_1.

The $4f$ system Figure 2.3 is now inserted in the object arm itself, and the object (PRPP_2) is kept at the first focal plane of lens L_2 (Figure 4.1). This is a slight modification to the previously discussed Mach-Zehnder set up (in Chapter 2). Nevertheless, the phase introduced solely due to PRPP_2 can still be retrieved .

Beam-splitter BS_2 now, acts to recombine the object and the reference beam and the image of interference pattern thus formed is captured in CCD screen placed at the second focal plane of lens L_3. The undistorted fringes (i.e. without the insertion of PRPP_2) are first collected and then the distorted interference fringes (i.e. PRPP_2 inserted in the object arm right at the first focal plane of lens L_2) are collected. PRPP_2, after insertion is rotated such that for all practical purposes, it is *stationary* with regard to the exposure time of the CCD camera.

The phase introduced solely due to PRPP_2 is eventually extracted by point wise subtraction of the unwrapped phase of undistorted fringe images from the unwrapped phase of distorted fringe images (as has been explained in Chapter 2, part 2.3.1.1). Note that here, the phase matrices of size 200×200 could be faithfully retrieved (Figure 4.2) for a further comparison with numerically generated phase screens.

4.2.2 Numerical Generation of Kolmogorov Phase Screens

The retrieved random phase arrays from the above discussed experiment on PRPP_2 (using 633 nm wavelength), are now compared with the numerically generated Kolmogorov random phase screens. These random phase screens are generated using a well known method, outlined in *Knepp (1983); Macaskill and Ewart (1984); Martin and Flatté (1988)*. This method originally involves the simulation of beam propagation through a turbulent medium by successive addition of phases acquired by the beam on propagation through a distance δ_z in the medium, while simultaneously taking care of the diffractive effects by interlacing the phase additions with Fresnel propagation through the same distance. The phase acquired by the beam through propagation of distance δ_z can be numerically computed with the knowledge of the Kolmogorov power spectrum.

In order to compare the phases introduced by the said PRPP with that of a turbulent atmosphere, the random phase obtained from the Kolmogorov power spectral density, (with the diffraction effect ignored) are taken into consideration. The phase spectrum of a random phase screen is related to the Kolmogorov power spectral density as *Tatarskii (1961)* :

$$\Phi_\theta(K) = 2\pi\kappa^2\delta_z\Phi_n(K), \tag{4.1}$$

where $\kappa = \frac{2\pi}{\lambda}$, δ_z is the distance of propagation during which the random phase is

acquired, and

$$\Phi_n(K) = 0.033 C_n^2 K^{\frac{-11}{3}}, \tag{4.2}$$

the Kolmogorov power spectral density, with C_n^2 being the atmospheric structure constant. The strength of atmospheric turbulence is reflected in the value of atmospheric structure constant, C_n^2. A C_n^2 of the order of $10^{-15}\mathrm{m}^{\frac{-2}{3}}$ implies very weak turbulence conditions. As one goes on increasing its order, i.e. from $10^{-15}\mathrm{m}^{\frac{-2}{3}}$ to $10^{-14}\mathrm{m}^{\frac{-2}{3}}$, $10^{-13}\mathrm{m}^{\frac{-2}{3}}$, $10^{-12}\mathrm{m}^{\frac{-2}{3}}$ and $10^{-11}\mathrm{m}^{\frac{-2}{3}}$, the strength of turbulence successively increases from very weak to very strong conditions *Tyson (2010)*. Now, to obtain the phase screen from the spectrum $\Phi_\theta(K)$, a 512×512 grid with entries $(K_x,\ K_y)$ is constructed, with $K_x = i\triangle_K$ and $K_y = j\triangle_K$, so that $K^2 = K_x^2 + K_y^2$. The indices i and j run from 1 to 512, and $\triangle_K = \frac{2\pi}{L}$, where L^2 is the detection area of the wave-field. A 512×512 array of pseudo random complex numbers is then point wise multiplied to the discretized version of the square root of the spectrum $\Phi_\theta(K)$ given by

$$\triangle_K^{-1}\sqrt{\Phi_\theta(i\triangle_K, j\triangle_K)}, \tag{4.3}$$

and the resulting 512×512 matrix is discrete Fourier transformed to obtain the random phase matrix with entries $(\theta_1 + i\theta_2)(\Delta Li, \Delta Lj)$. Either of the 512×512 matrices $(\theta_1(\Delta Li, \Delta Lj))$ or $(\theta_2(\Delta Li, \Delta Lj))$ yields the desired random phase screen $\theta(\Delta L\, i, \Delta Lj)$, where $\Delta L = L/512$. These Kolmogorov phase screens are generated for different values of atmospheric structure constants ranging from very weak to very strong turbulence conditions, the distances δ_z's are also varied accordingly.

4.2.3 Statistical Estimates

To compare the phase of $PRPP_2$ estimated from the above mentioned experiment with that of numerically generated Kolmogorov phase screens, the well known statistical indicators typically used in optical testing to compare the smoothness/roughness of surfaces *Sedlaček et al. (2012); Rhee et al. (2005); Duparre et al. (2002); Gadelmawla et al. (2002); Banat (2003)* are used. Since the measured and numerically generated phases are points on a surface taking the values $\theta_{ij} = \theta(i, j)$ labeled by indices i and j, they can be compared in this manner. In the present context, since the experimentally retrieved phase data is of the form $\theta_{ij}^{\exp}$ with i and j taking values from 1 to 200, and

the phase data obtained numerically, i.e., $\theta_{ij}^{\rm num}$ is of size 512×512, the numerically obtained phase values are clipped to size 200×200 and then the quantities of interest *Gadelmawla et al. (2002)* are evaluated for comparison. The quantities of interest are as follows:

- Mean : The mean value of a surface *Kendall and Yule (1950); Gadelmawla et al. (2002)* specified by the array of values θ_{ij} is given as

$$\langle\theta\rangle = \frac{1}{M \times N}\sum_{i=1}^{M}\sum_{j=1}^{N}\theta_{ij}. \tag{4.4}$$

  In the present context, $M = N = 200$.

- RMS : The RMS or root mean squared value of a surface specified by values θ_{ij} is defined as *Kendall and Yule (1950); Gadelmawla et al. (2002)*

$$\mathrm{RMS}(\theta) = \sqrt{\frac{1}{M \times N}\sum_{i=1}^{M}\sum_{j=1}^{N}\theta_{ij}^2}. \tag{4.5}$$

Both the mean and RMS of a surface give an estimate of the average *height* of the surface.

- $\mathrm{R_a}$: The parameter $\mathrm{R_a}$ denotes the roughness average for a surface and is defined as *Rhee et al. (2005); Gadelmawla et al. (2002)*

$$\mathrm{R_a} = \frac{1}{M \times N}\sum_{i=1}^{M}\sum_{j=1}^{N}|\theta_{ij} - \langle\theta\rangle|. \tag{4.6}$$

  Here $\langle\theta\rangle$ is the mean and $||$ denotes absolute value.

- $\mathrm{R_q}$: The standard deviation from mean of a surface is defined as *Kendall and Yule (1950); Gadelmawla et al. (2002)*

$$\mathrm{R_q} = \sqrt{\frac{1}{M \times N}\sum_{i=1}^{M}\sum_{j=1}^{N}\left(\theta_{ij} - \langle\theta\rangle\right)^2}. \tag{4.7}$$

  Both roughness average, R_a and standard deviation R_q are the measures of fluctuations from the mean value.

- $\mathrm{R_t}$: The peak to valley distance denoted by $\mathrm{R_t}$ for a surface is defined as *Rhee et al. (2005); Gadelmawla et al. (2002)*:

$$\mathrm{R_t} = |\theta_{max} - \langle\theta\rangle| + |\langle\theta\rangle - \theta_{min}|, \tag{4.8}$$

where θ_{max} is the maximum value the phase $\{\theta_{ij}\}$ can take in the $M \times N$ array and θ_{min} similarly is the minimum value, the phase $\{\theta_{ij}\}$ can take in the same array.

The comparison using above parameters has been presented in the following Section.

4.3 Comparison Results

Figure (4.2) shows a sample of interference fringes obtained from the experiment and the corresponding phase array estimated from the interference fringes.

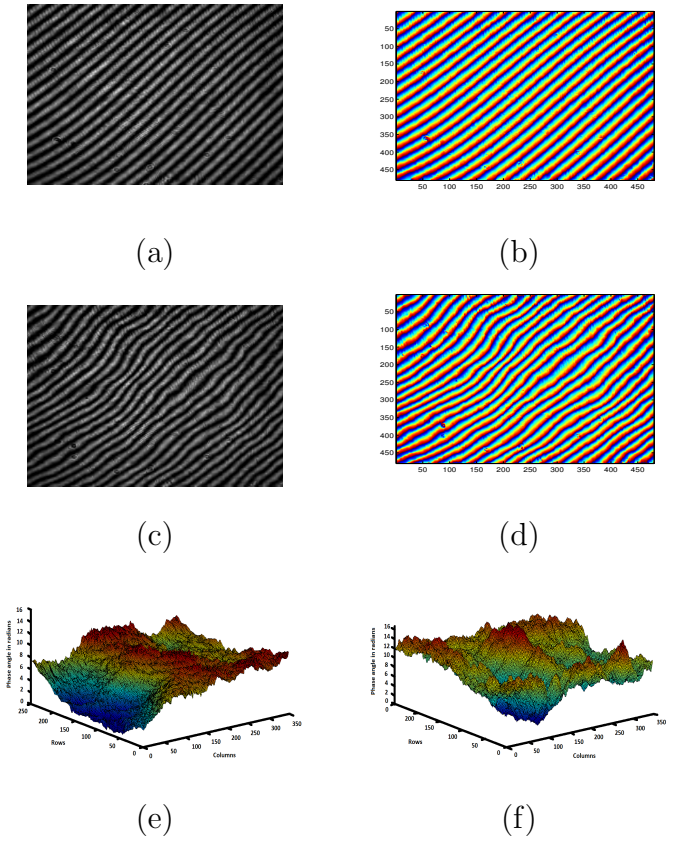

Figure 4.2: Interference Fringes (Distorted and Undistorted) and the Phase Portions (Experimental and Numerical)

In Figure (4.2), frames (a) and (b) show the captured and numerically reconstructed fringes of one of the CCD images for first step of the experimental procedure wherein $PRPP_2$ was not inserted in the Mach-Zehnder interferometric set up. Frames (c) and (d) on the other hand show the captured and reconstructed fringes respectively of one of the images for the second step of experimental procedure in which $PRPP_2$ was inserted at the first focal plane of the lens L_2 (refer Figure (4.1)). Frame (e) shows the unwrapped portion of the phase estimated from the fringes shown in frame (c). Frame (f) shows a numerically generated random phase screen in comparison to frame (e).

Figure (4.3 and 4.4) now, show a comparison between the statistical estimates (of Section 4.2.3), calculated for the experimentally obtained 400 unwrapped phase sample arrays, θ_{ij}^{exp}'s, each of size 200×200 with the numerically generated phase screens θ_{ij}^{num}'s of the same size. While generating the phase screens, the value of atmospheric structure constant, C_n^2 has been kept at $10^{-15} m^{\frac{-2}{3}}$ (i.e. very weak turbulence conditions) and 400 samples have been collected for each δ_z starting from $\delta_z = 50000$ Km to $\delta_z = 200000$ Km, incrementing in steps of 25000 Km.

The first plot (plotted in pink color) in column (a) (in Figure 4.3) is a plot for the calculated Mean values of the 400 experimentally obtained phase sample arrays. The plots that follow downwards (plotted in blue) in column (a) are all for $C_n^2 = 10^{-15} \mathrm{m}^{\frac{-2}{3}}$, with increasing δ_z from 50000 Km to 200000 Km in steps of 25000 Km. It can be seen that the experimentally obtained result for mean values does not match faithfully with any of the numerically produced mean values. Though, on an average, the mean value of 7.6348 for the case of $\delta_z = 75000$ Km looks comparable to experimentally obtained 7.1025 (as can be seen from the marked black lines in the respective graphs), but the fluctuations about this (experimental) value are far more higher than the numerically simulated case.

On similar lines, the RMS values have been compared in column (b) (in Figure 4.3), roughness average, R_a in column (c) (in Figure 4.3), Standard deviation R_q in column (d) (in Figure 4.4) and lastly, peak to valley distance R_t in column (e) (in Figure 4.4).

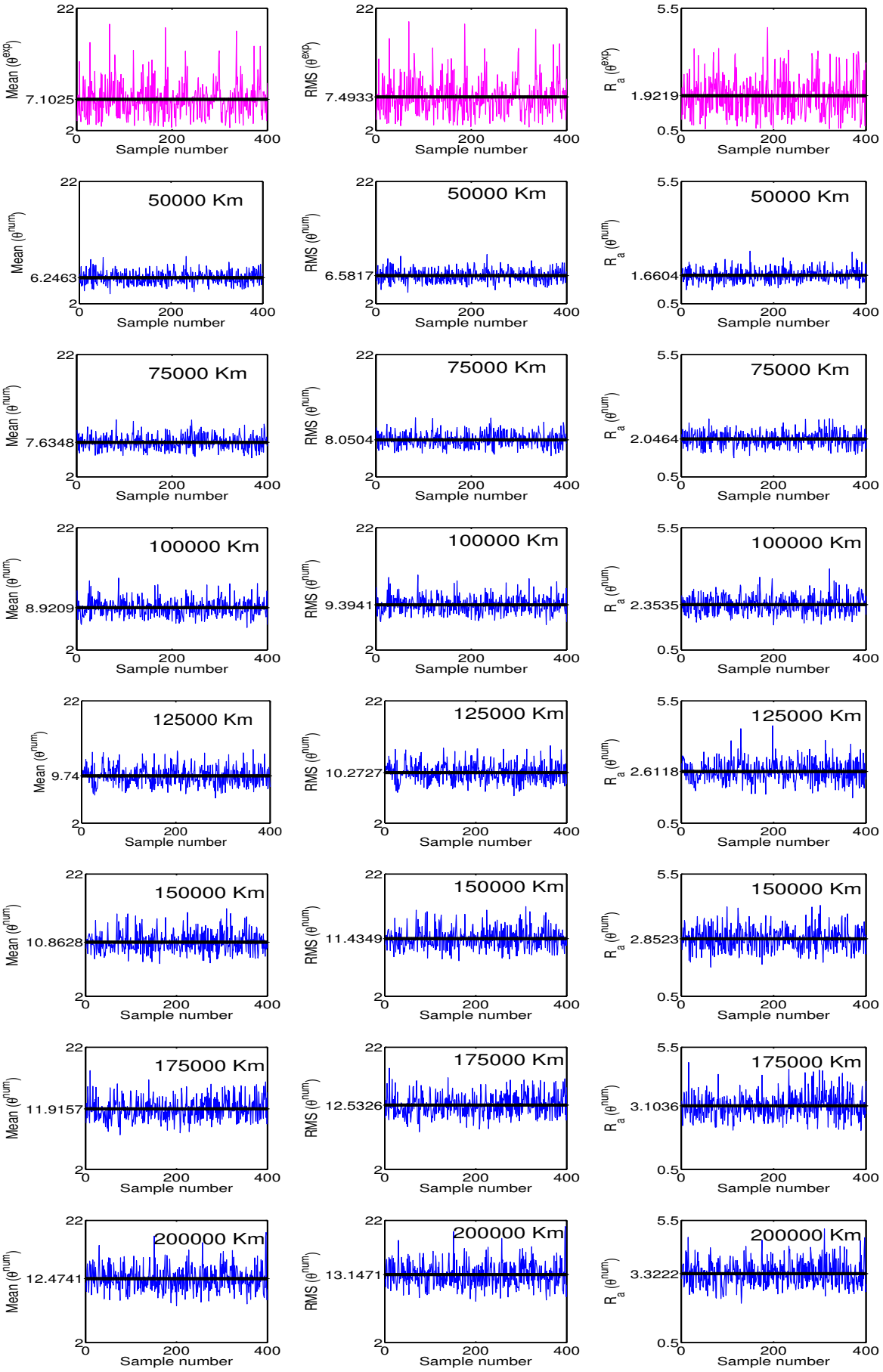

(a) Comparison of Mean (b) Comparison of RMS (c) Comparison of R_a

Figure 4.3: $C_n^2 = 10^{-15} m^{\frac{-2}{3}}$ (Mean, RMS, and Roughness Average)

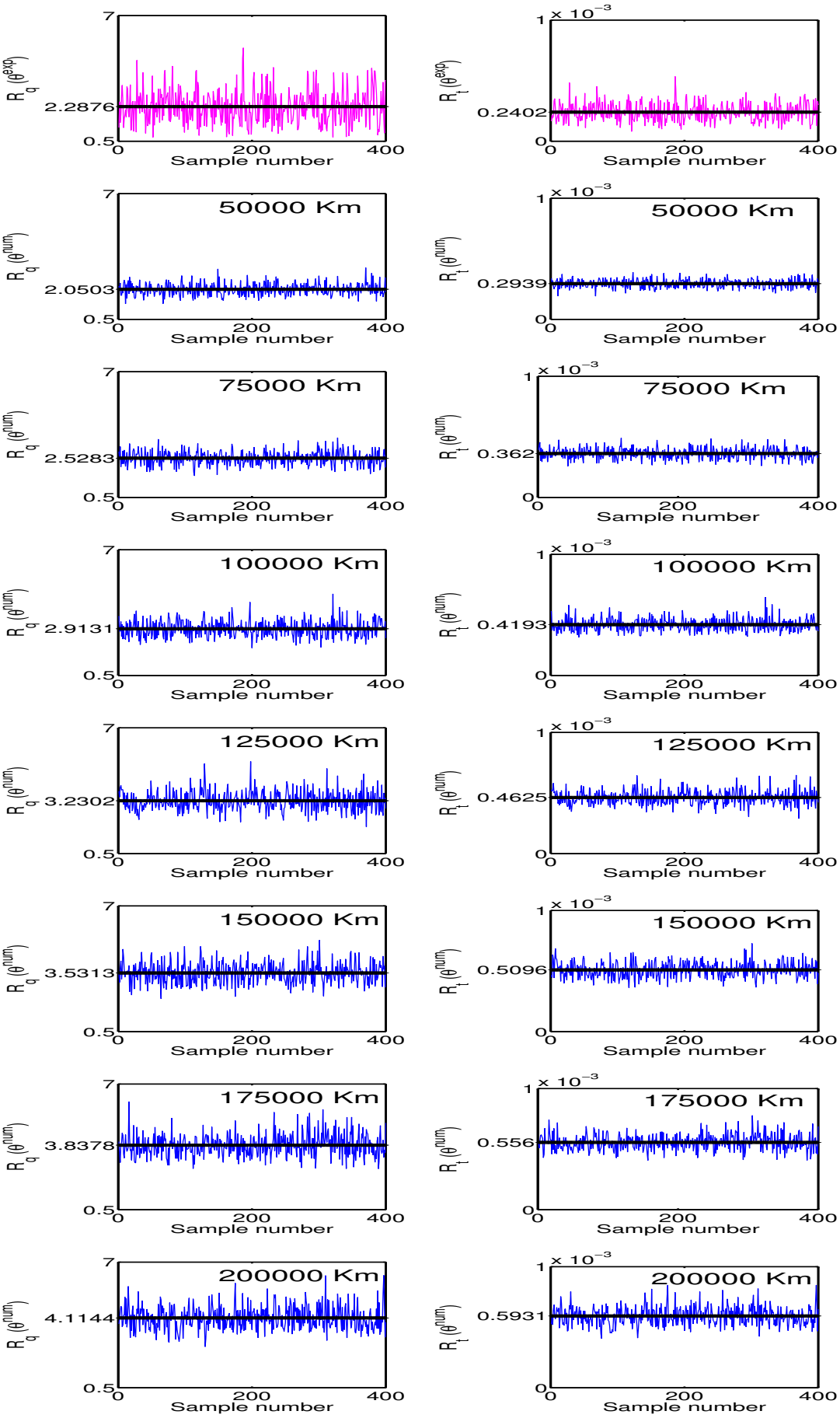

(d) Comparison of R_q (e) Comparison of R_t

Figure 4.4: $C_n^2 = 10^{-15} m^{\frac{-2}{3}}$ (Standard Deviation and Peak to Valley Distance)

It is clear from the comparison presented in these columns that none of the statistical estimates is reproduced faithfully in numerical simulations using Kolmogorov phase screens with $C_n^2 = 10^{-15}\mathrm{m}^{\frac{-2}{3}}$. For higher values of δ_z, the fluctuations about the average values of all statistical estimates increase along with an increase in their average values themselves, which is surely a mismatch as regards the experimental results.

In Figure (4.5 and 4.6), the same exercise of comparing the statistical estimates for experimental and numerical phase arrays has been repeated, keeping again the number of samples, 400 and the size of each sample 200×200, but changing C_n^2 now to $10^{-14}\mathrm{m}^{\frac{-2}{3}}$ and accordingly varying δ_z in steps of 2500 Km starting with $\delta_z = 5000$ Km going uptill $\delta_z = 20000$ Km for numerical simulations. From columns (a) to (c) in Figure 4.5 and columns (d) and (e) in Figure 4.6, statistical estimates calculated for 400 experimentally estimated unwrapped phase sample arrays θ_{ij}^{exp} and the same number of numerically generated phase screens θ_{ij}^{num}, obtained for weak turbulence conditions i.e. $C_n^2 = 10^{-14}\mathrm{m}^{\frac{-2}{3}}$ and increasing δ_z have been compared. Again, the first plot in each column ((a) to (c) in Figure 4.5 and columns (d) and (e) in Figure 4.6) corresponds to the statistical estimate values plotted for experimentally obtained 400 unwrapped phase sample arrays. This is followed downwards in all columns by the plots of the corresponding statistical estimates for 400 sample arrays of numerically generated phase screens for one δ_z at a time (keeping $C_n^2 = 10^{-14}\mathrm{m}^{\frac{-2}{3}}$ constant), incrementing δ_z in steps of 2500 Km, starting with $\delta_z = 5000$ Km. Clearly, again there is a mismatch between calculated statistical estimates in the two cases. Nowhere do the experimental and numerical cases show a faithful correspondence.

Similarly, Figure (4.7 and 4.8); Figure (4.9 and 4.10) and Figure (4.11 and 4.12) show a one by one comparison of all statistical estimates of Section 4.2.3, of numerical cases having $C_n^2 = 10^{-13}m^{\frac{-2}{3}}$; $C_n^2 = 10^{-12}\mathrm{m}^{\frac{-2}{3}}$ and $C_n^2 = 10^{-11}\mathrm{m}^{\frac{-2}{3}}$ respectively with the experimentally retrieved sample phase arrays. The distances δ_z in Figure (4.7) and (4.8) vary from $\delta_z = 500\mathrm{Km}$ to $\delta_z = 1000\mathrm{Km}$ in steps of $250\mathrm{Km}$, whereas in Figure (4.9) and (4.10), i.e. for strong turbulence case, with $C_n^2 = 10^{-12}\mathrm{m}^{\frac{-2}{3}}$, δ_z starts from $50\mathrm{Km}$ and goes till $200\mathrm{Km}$ varying in steps of $25\mathrm{Km}$. Lastly in Figure (4.11) and (4.12), for very strong turbulence, with $C_n^2 = 10^{-11}\mathrm{m}^{\frac{-2}{3}}$, δ_z starts with $5\mathrm{Km}$, goes in steps of $2.5\mathrm{Km}$, and ends with $20\mathrm{Km}$.

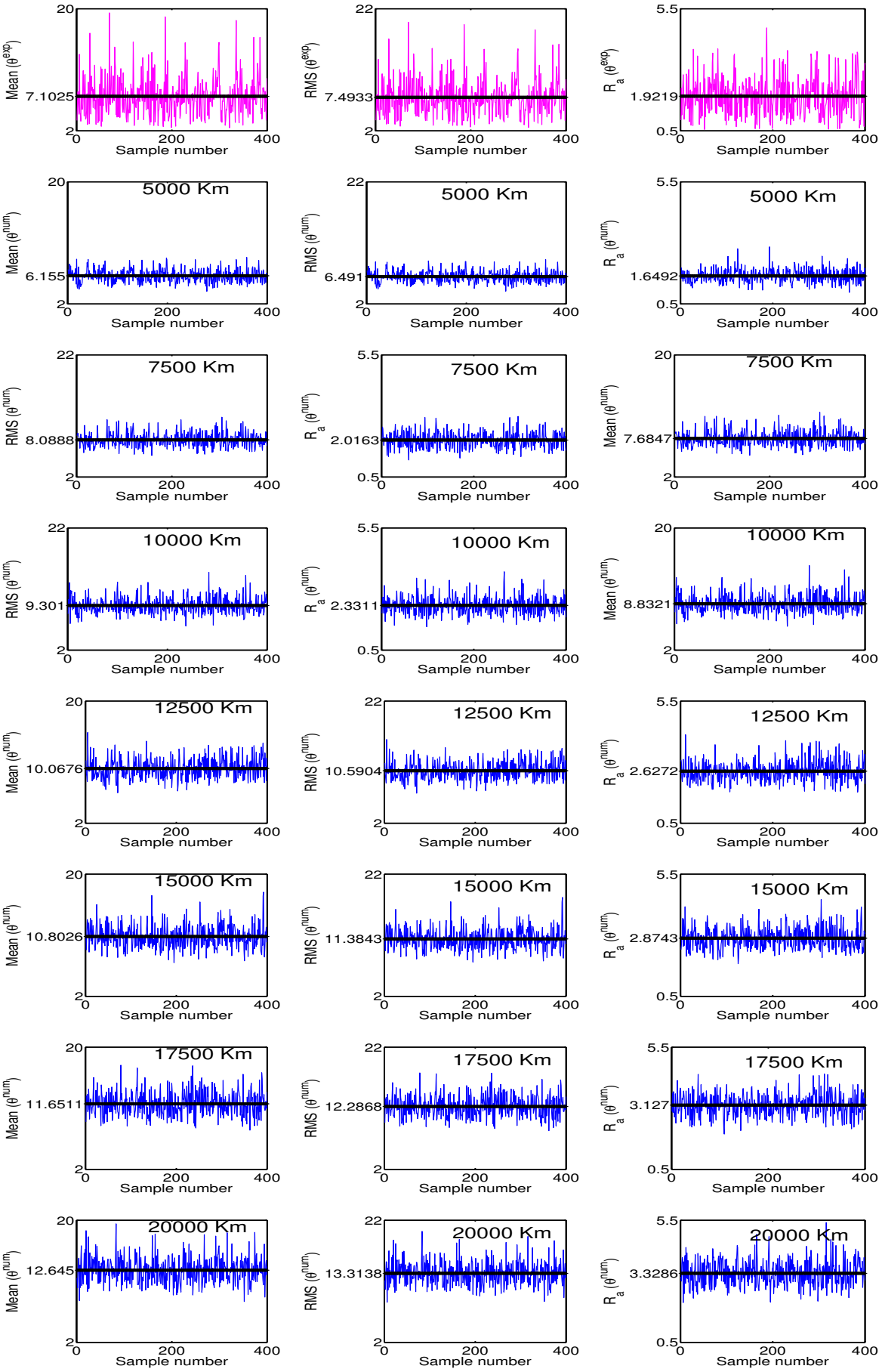

(a) Comparison of Mean (b) Comparison of RMS (c) Comparison of R_a

Figure 4.5: $C_n^2 = 10^{-14} m^{\frac{-2}{3}}$ (Mean, RMS, and Roughness Average)

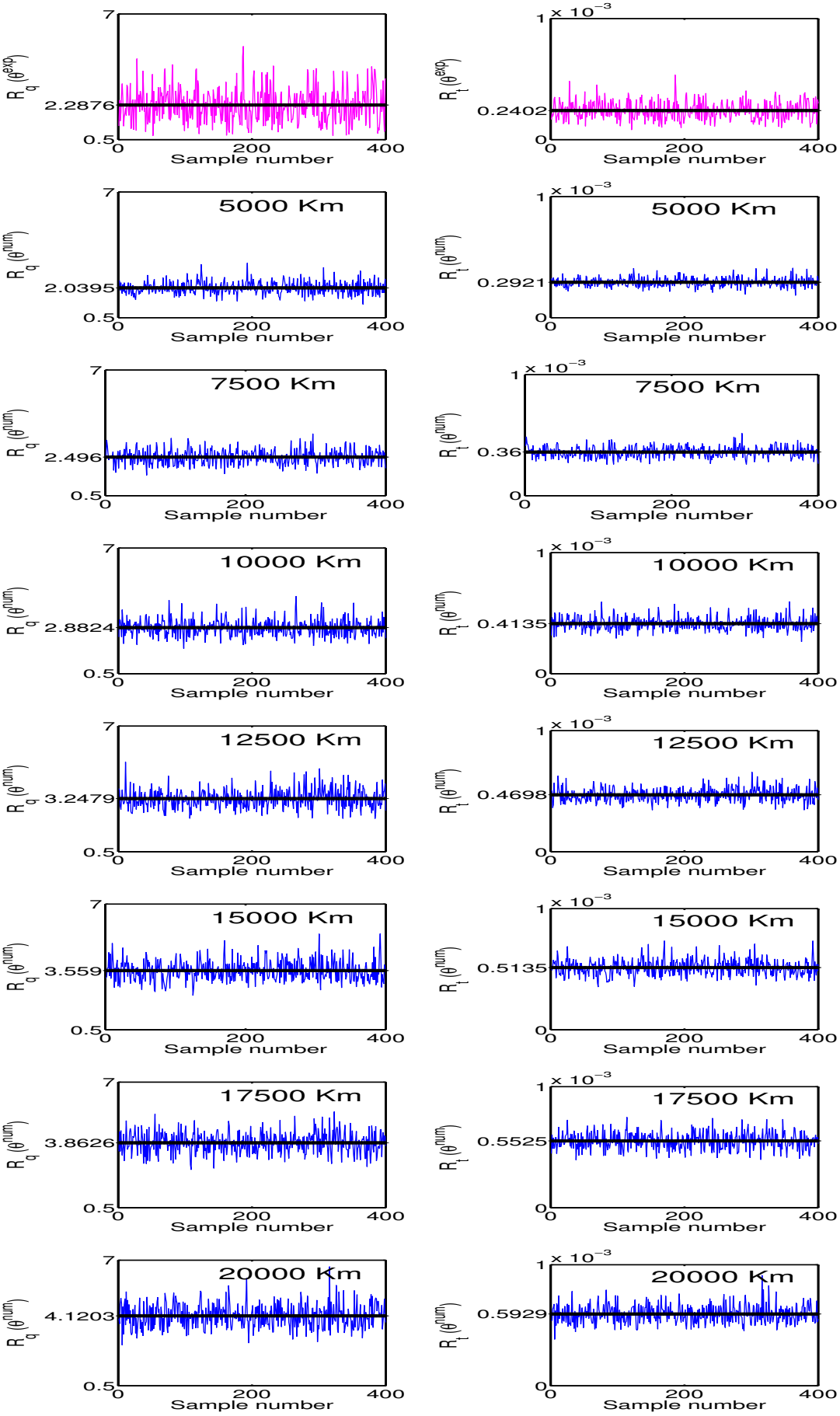

(d) Comparison of R_q (e) Comparison of R_t

Figure 4.6: $C_n^2 = 10^{-14} m^{\frac{-2}{3}}$ (Standard Deviation and Peak to Valley Distance)

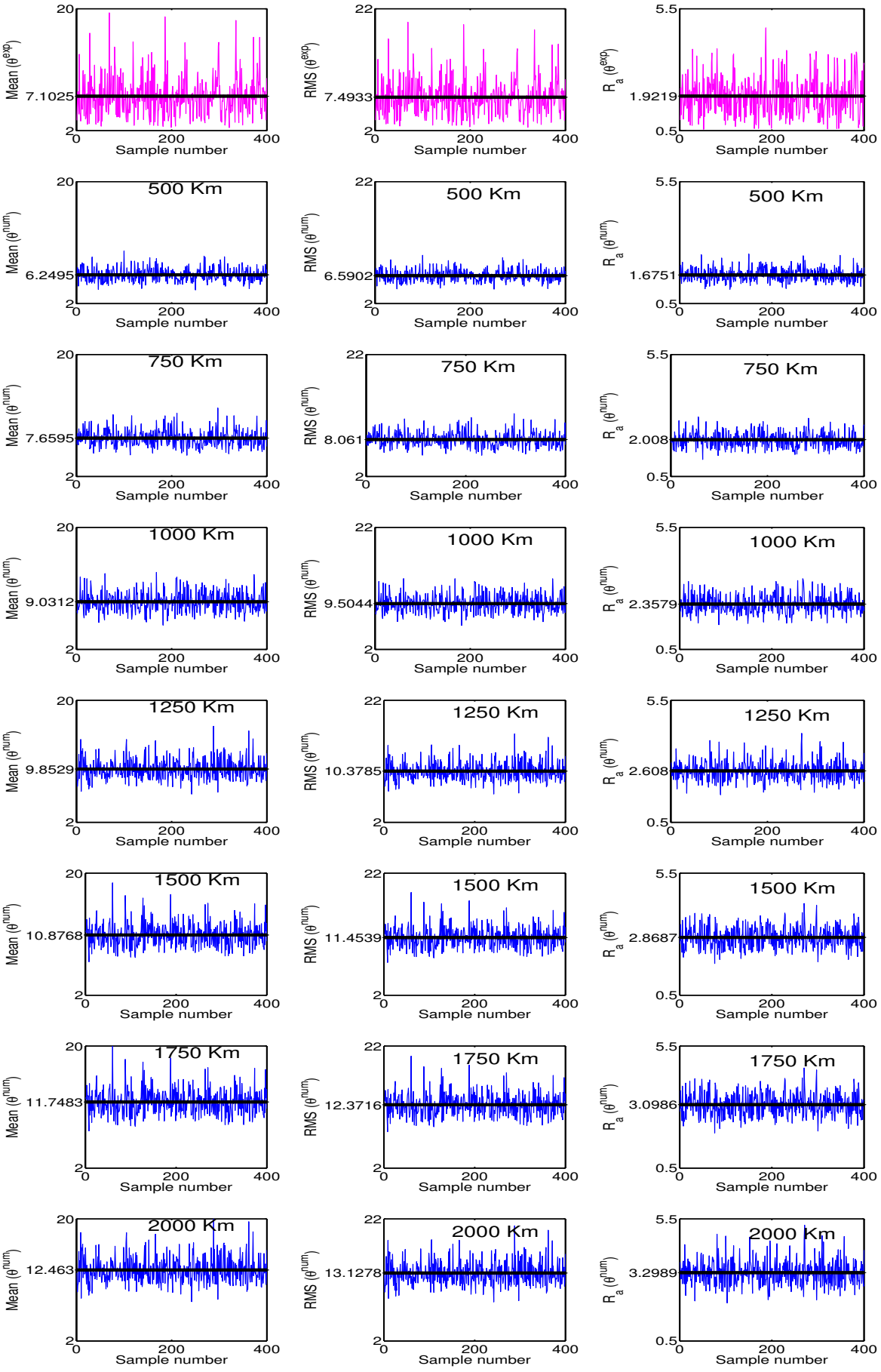

(a) Comparison of Mean (b) Comparison of RMS (c) Comparison of R_a

Figure 4.7: $C_n^2 = 10^{-13} m^{\frac{-2}{3}}$ (Mean, RMS, and Roughness Average)

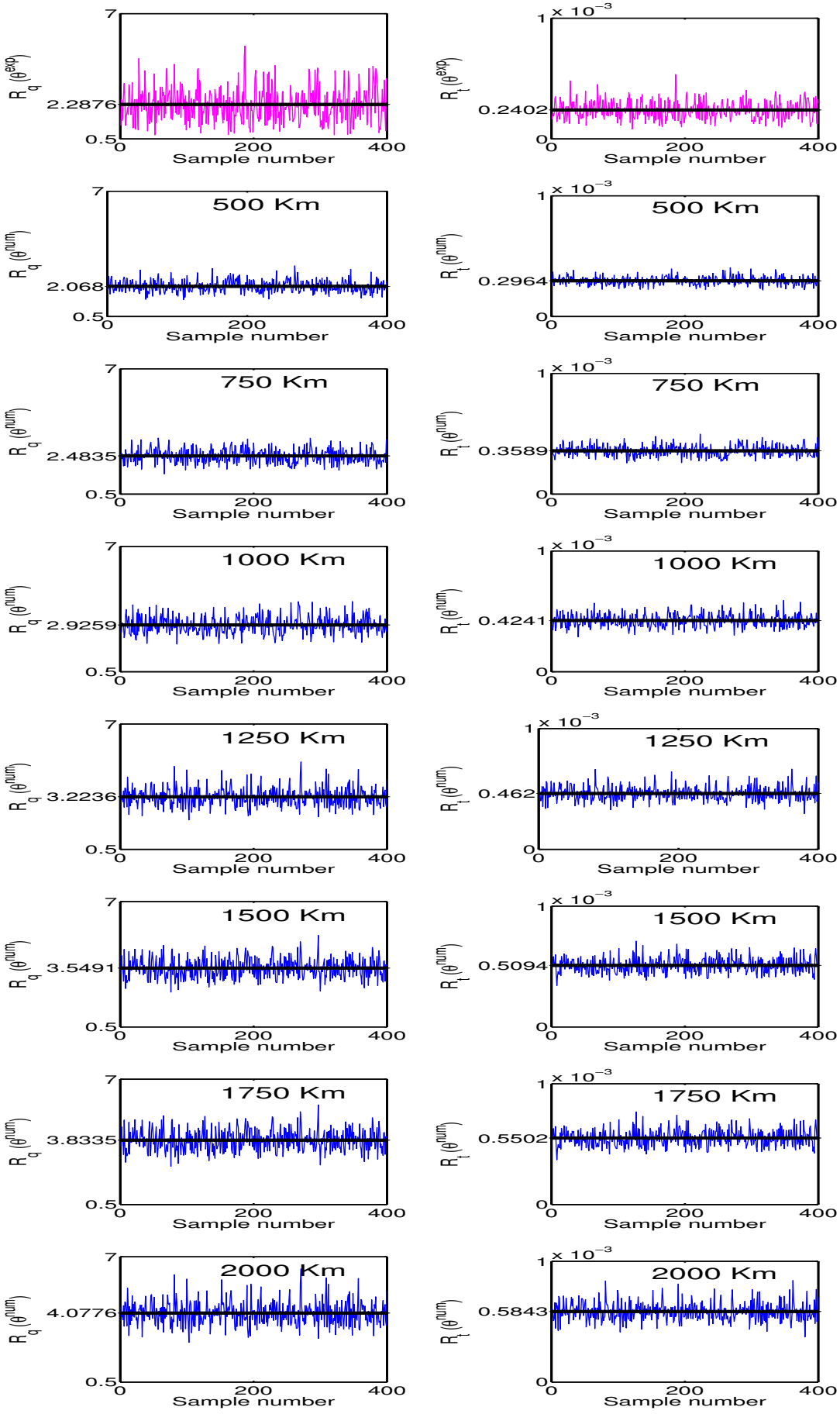

(d) Comparison of R_q (e) Comparison of R_t

Figure 4.8: $C_n^2 = 10^{-13} m^{\frac{-2}{3}}$ (Standard Deviation and Peak to Valley Distance)

From columns (a) to (e) of Figures 4.7 and 4.8, statistical estimates calculated for 400 experimentally estimated unwrapped phase sample arrays θ_{ij}^{exp} and the same number of numerically generated phase screens θ_{ij}^{num}, obtained now for turbulence conditions with $C_n^2 = 10^{-13}\mathrm{m}^{\frac{-2}{3}}$ and increasing δ_z have been compared. The first plot in each column (from (a) to (e) in both the figures) corresponds to the statistical estimate values plotted for experimentally obtained 400 unwrapped phase sample arrays. This is followed downwards in all columns by the plots of the corresponding statistical estimates for 400 sample arrays of numerically generated phase screens for one δ_z at a time (keeping $C_n^2 = 10^{-13}\mathrm{m}^{\frac{-2}{3}}$ constant), incrementing δ_z in steps of 250 Km, starting with $\delta_z = 500$ Km.

Similarly, a comparison of statistical estimates of Section 4.2.3, calculated for 400 experimentally estimated unwrapped phase sample arrays θ_{ij}^{exp} and the same number of numerically generated phase screens θ_{ij}^{num}, obtained for strong turbulence conditions i.e. $C_n^2 = 10^{-12}m^{\frac{-2}{3}}$ and increasing δ_z has been shown in Figures 4.9 and 4.10. The first plot on top in each column (from (a) to (e) in both the figures) again corresponds to the statistical estimate values plotted for experimentally obtained 400 unwrapped phase sample arrays. Further downwards in all columns, the corresponding plots for statistical estimates for 400 sample arrays of numerically generated phase screens for one δ_z at a time (keeping $C_n^2 = 10^{-12}\mathrm{m}^{\frac{-2}{3}}$ constant), incrementing δ_z in steps of 25 Km, starting with $\delta_z = 50$ Km have been shown.

Finally, a comparison of statistical estimates of Section 4.2.3 calculated for 400 experimentally estimated unwrapped phase sample arrays θ_{ij}^{exp} and the same number of numerically generated phase screens θ_{ij}^{num}, obtained for very strong turbulence conditions, i.e. with strength $C_n^2 = 10^{-11}\mathrm{m}^{\frac{-2}{3}}$ has been shown in Figures 4.11 and 4.12. The first plot on top in each column ((a) to (e)) corresponds to the statistical estimate values plotted for experimentally obtained 400 unwrapped phase sample arrays, followed as usual downwards in all columns by plots of the corresponding statistical estimates for 400 sample arrays of numerically generated phase screens with one value of δ_z at a time (keeping $C_n^2 = 10^{-11}\mathrm{m}^{\frac{-2}{3}}$ constant), incrementing δ_z in steps of 2.5 Km, starting with $\delta_z = 5$ Km.

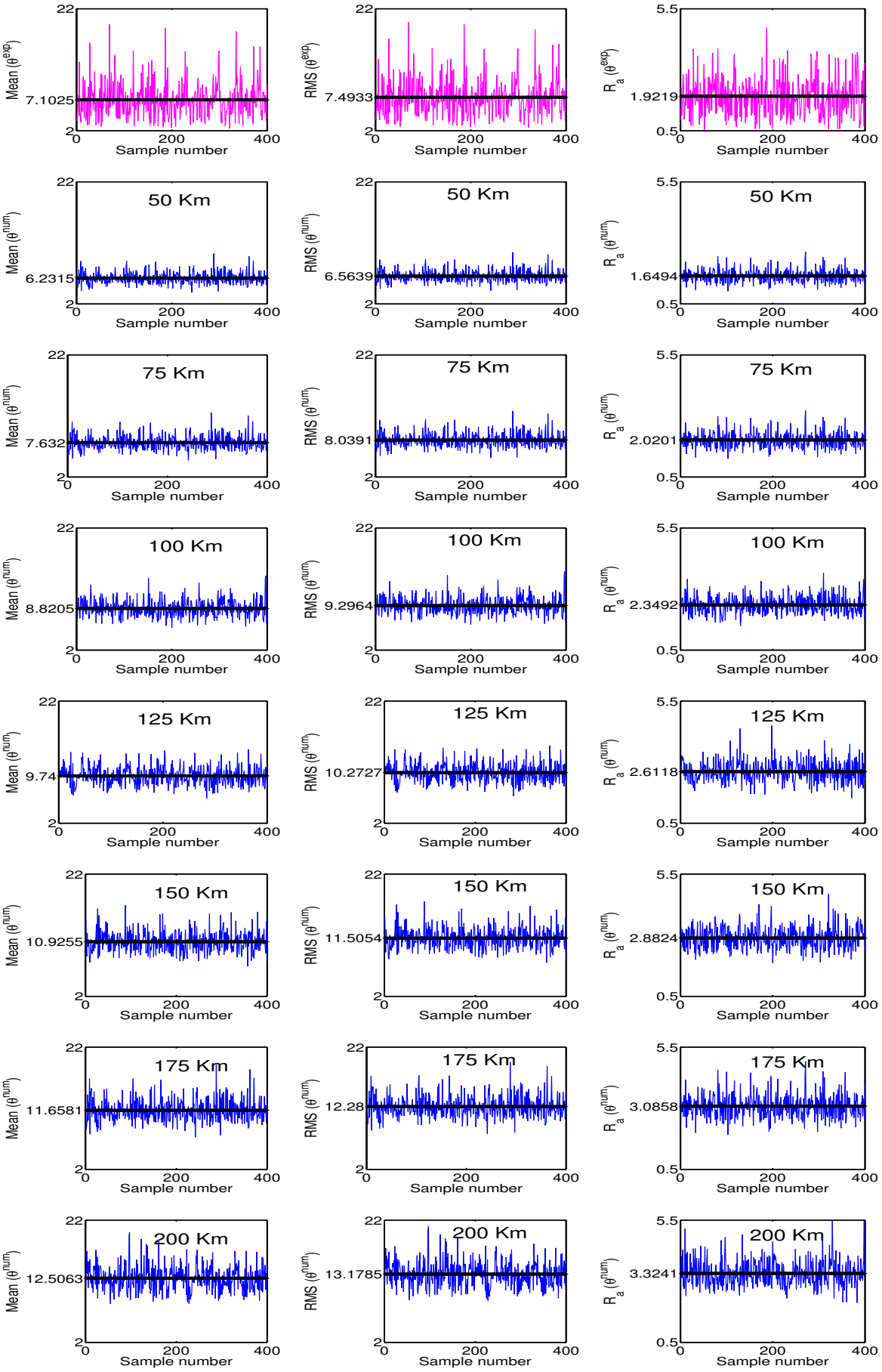

(a) Comparison of Mean (b) Comparison of RMS (c) Comparison of R_a

Figure 4.9: $C_n^2 = 10^{-12} m^{\frac{-2}{3}}$ (Mean, RMS, and Roughness Average)

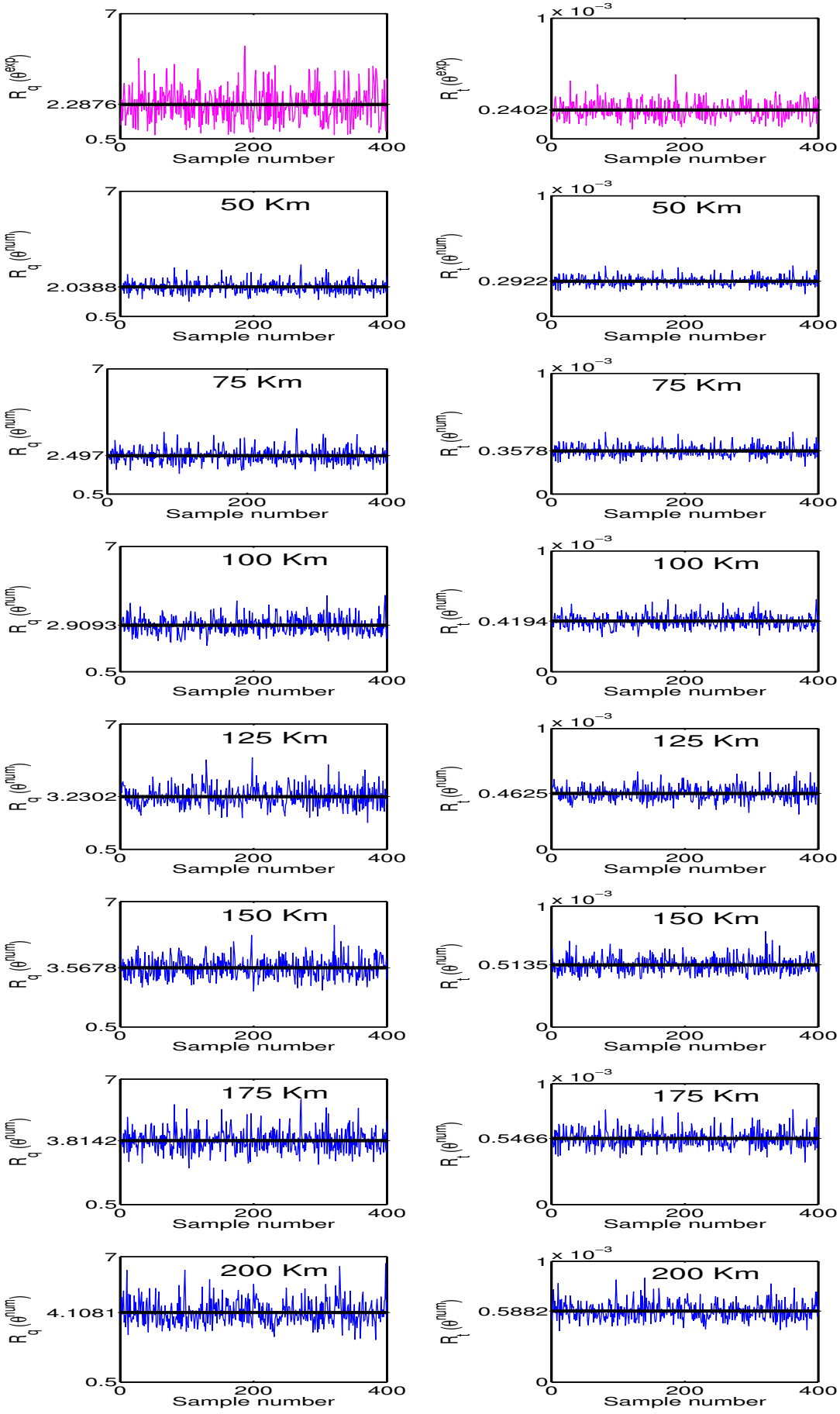

(d) Comparison of R_q (e) Comparison of R_t

Figure 4.10: $C_n^2 = 10^{-12} m^{\frac{-2}{3}}$ (Standard Deviation and Peak to Valley Distance)

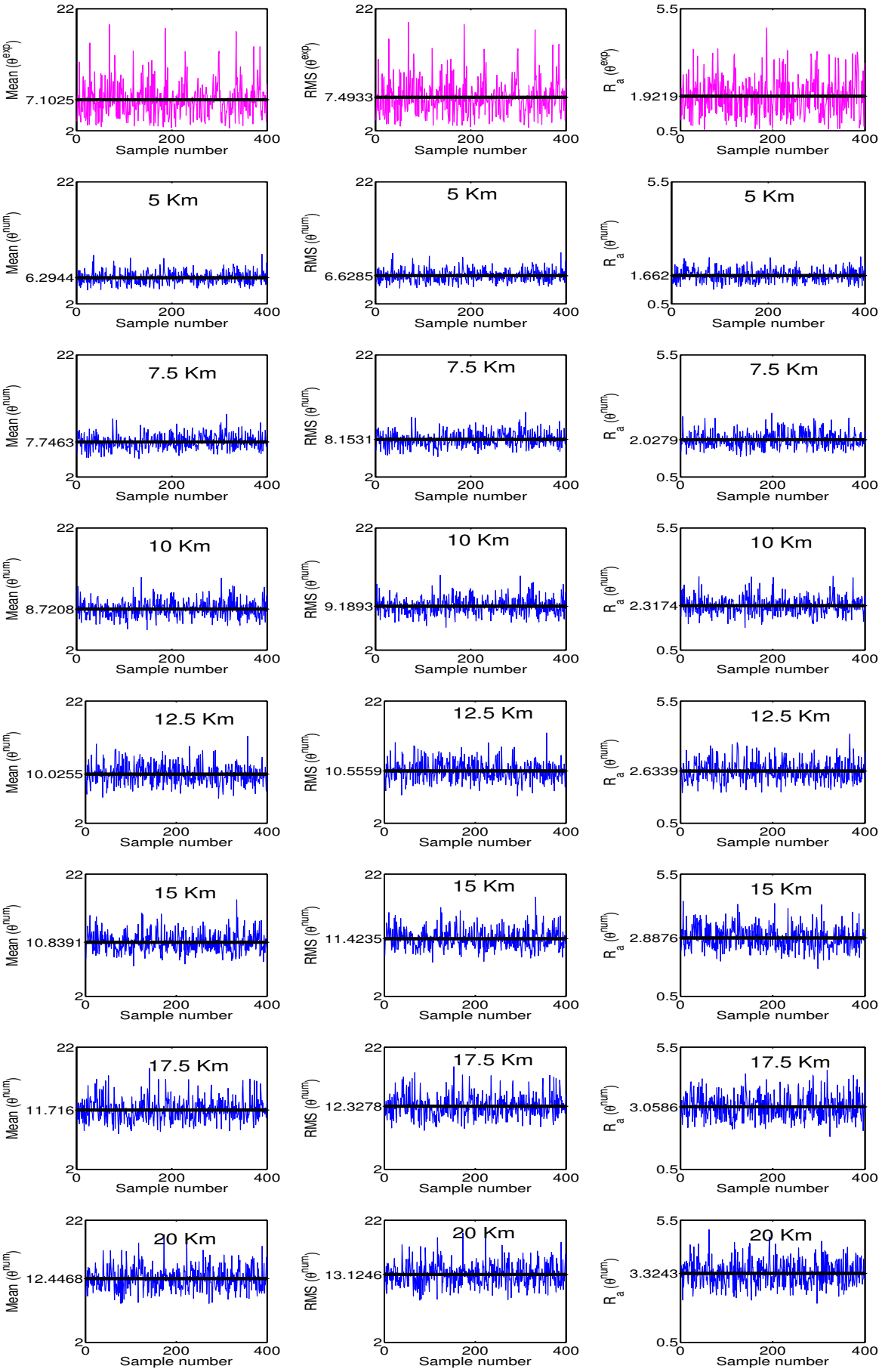

(a) Comparison of Mean (b) Comparison of RMS (c) Comparison of R_a

Figure 4.11: $C_n^2 = 10^{-11} m^{\frac{-2}{3}}$ (Mean, RMS, and Roughness Average)

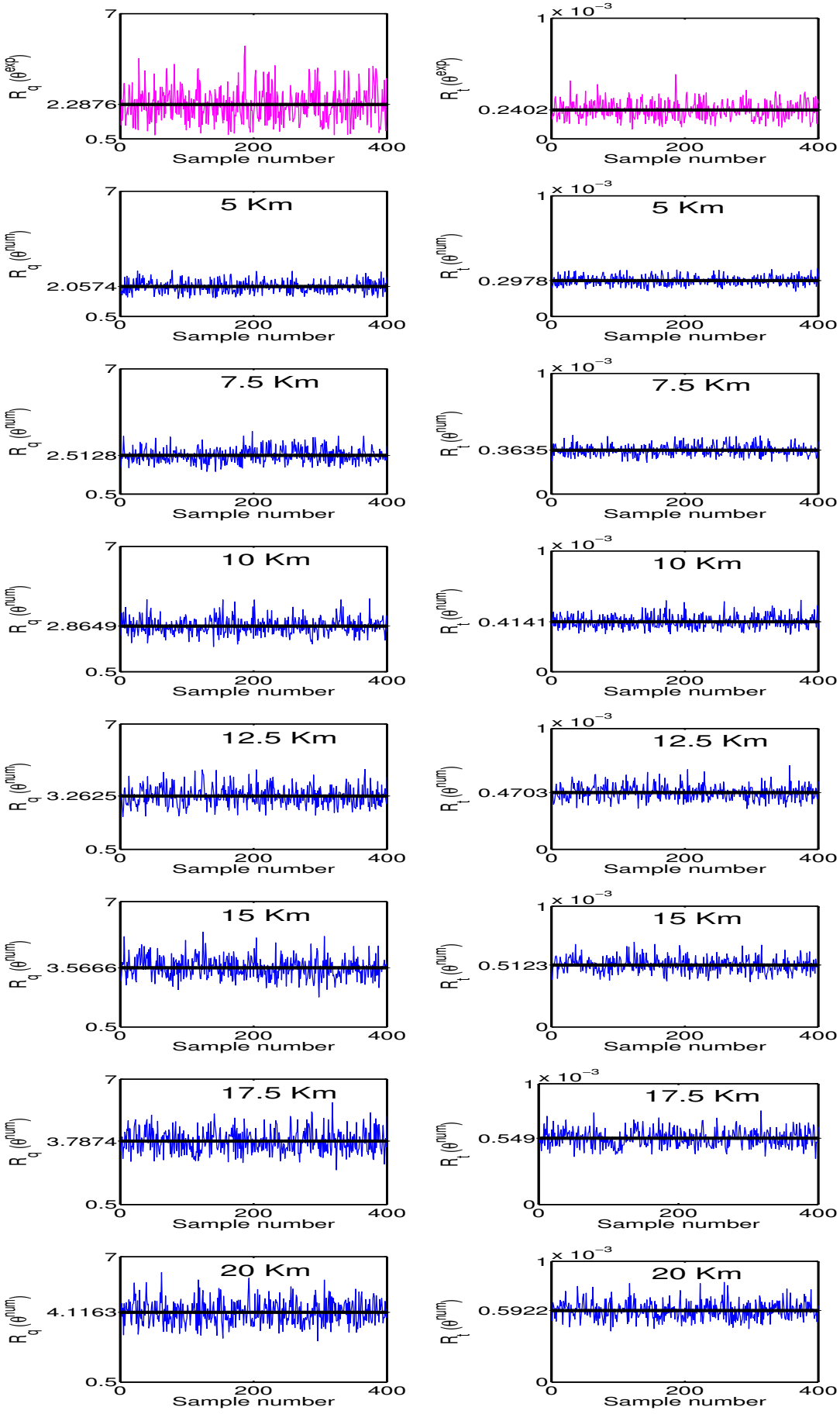

(d) Comparison of R_q (e) Comparison of R_t

Figure 4.12: $C_n^2 = 10^{-11} m^{\frac{-2}{3}}$ (Standard Deviation and Peak to Valley Distance)

The trend visible from all the figures is similar in the sense that, the fluctuations about average values of statistical estimates for numerically generated phases increase with their increasing average values. These in turn increase with increasing δ_z for one particular C_n^2. The mismatch with respect to the calculated statistical estimates of experimentally retrieved phase sample arrays is apparent in all the cases.

Thus, this extensive quantitative analysis, done for atmospheric structure constant values ranging from $10^{-15}\mathrm{m}^{\frac{-2}{3}}$ (very weak turbulence conditions) to $10^{-11}\mathrm{m}^{\frac{-2}{3}}$ (very strong turbulence conditions) shows that the retrieved phases from PRPP (PRPP_2) used in this experiment represent some different class of phase arrays for a wavelength of 633 nm and they do not exactly match with that of Kolmogorov phase screens. But, with this method, nothing can be said emphatically about PRPPs nature.

It should noted here that with the previous experiments shown in Chapter 2, the considered PRPP has already been characterized as a non-Kolmogorov turbulence simulator at 633 nm. Therefore, the method that uses the phase structure function for PRPP characterization is better than the method of statistical parameter estimation. This is attributed to the fact that no conclusion on the said PRPP's nature could be reached at with the latter method, whereas with the phase structure function analysis, a robust conclusion about the PRPP's nature was drawn.

4.4 Summary

In this Chapter, the characterization of Pseudo-Random-Phase-Plate (PRPP_2) has been attempted by using statistical parameters generally employed for characterizing surface roughness. Results of the method used hint towards the possibility of PRPP being a different class of turbulence simulator at 633 nm wavelength and not the conventional Kolmogorov simulator as has been claimed in *Mantravadi et al. (2004)* (for 1550 nm), but nothing can be said emphatically about its nature. However, in Chapter 2, a clear conclusion that the PRPP presents a non-Kolmogorov turbulence regime at 633 nm wavelength was arrived at. Therefore, it is concluded that the method involving the phase structure function is more appropriate for characterizing a PRPP.

CHAPTER 5

Conclusions and Future Scope

The main focus of this thesis was to reveal the nature of specially designed turbulence mimicking media, i.e. the Pseudo-Random-Phase-Plates (PRPPs) and to measure their effects on a propagating 633 nm He-Ne laser beam. Overall, the thesis presented an analysis on the extracted phase using the phase structure function, a demonstration of phase sharing between two spatially separated observers, an estimation of Variance matrix and its derivatives, and an attempt on characterization of a PRPP using standard statistical parameters which are usually used for surface roughness.

- The thesis began with the characterization of PRPPs as non-Kolmogorov turbulence simulators as regards 633 nm wavelength. This was done by calculating phase structure function on the extracted phase in the two classical interferometric geometries namely the Mach-Zehnder and the Michelson's interferometer. It was noticed that the nature of turbulence depends upon the number of passages the beam travels through the PRPPs. More specifically, the tendency of approaching towards Kolmogorov turbulence regime on increasing the number of passages through the given PRPP or PRPPs-in-a-combination was witnessed. Also, a Phase-sharing experiment using the Mach-Zehnder interferometer to distill a shared random secret key between two spatially separated observers was mentioned as an application of PRPP.

- Further, in order to study the effects that these PRPPs can introduce to a propagating 633 nm He-Ne laser wave-field, the thesis focused on the calculation of Variance matrices at different propagation planes (of a 633 nm He-Ne laser wave-field) with the help of intensity and beam centroid data extracted from a Shack-Hartmann-Wavefront-Sensor (SHWFS) at these planes. This was preceded by a description of the Variance matrix genesis and its properties. The Variance matrix calculation at different propagation planes was done for both a freely propagating laser beam and a beam that has encountered a PRPP in its path (either once or

twice). These were subsequently compared using physically significant quantities derived from the Variance matrix. It was found that there is enhancement of the fluctuation in all the measured quantities upon the insertion of the PRPP. Nevertheless, it was seen that the wave-field asymmetry on average decreases upon passage through the PRPP.

- The thesis also presented a comparison of the statistical parameters usually used for characterizing surface roughness, calculated on the phase matrices extracted in the Mach-Zehnder interferometric geometry, with the statistical parameters for known, numerically generated Kolmogorov phase screens, to again determine the nature of one of the said PRPP. It was found that the already discussed method involving phase structure determination is better than the current one for characterizing PRPP at a particular wavelength.

The future scope for the research work in this thesis is as follows:

- Since the static turbulent media (PRPPs) (which have been claimed as Kolmogorov turbulence simulators at 1550 nm wavelength by the suppliers) have been found to be non-Kolmogorov for 633 nm wavelength, these can henceforth be used as either Kolmogorov or non-Kolmogorov simulators at the respective wavelengths. Also, the tendency of approaching towards Kolmogorov turbulence regime on increasing the number of passages through a PRPP or PRPPs-in-a-combination leaves a big future scope for further experimentation and theoretical analysis on such a dependence. In future, one may also consider designing interferometric geometries which can facilitate more than two passages through an inserted medium.

- In phase sharing scheme, the two remote observers can be in principle well-separated spatially so that atmospheric turbulence in the arms of the interferometer generates the shared random phases. The shared random phases can also be used by the respective observers for image encryption purposes as well as other cryptographic applications.

- Wave propagation analysis on a PRPP using the Variance matrix and the derived physically significant parameters can be further extended to more realistic random media such as atmospheric turbulence. Study of the Variance matrix and these

parameters on multiple passages through the PRPP/PRPPs-in-a-combination for various possible wavelengths can also be initiated in future. One can as well consider the propagation study of vortex beams of different charges through single or multiple PRPPs for various possible wavelengths and geometries.

REFERENCES

Al-Habash, M., Andrews, L. C., and Phillips, R. L. (2001). Mathematical model for the irradiance probability density function of a laser beam propagating through turbulent media. *Optical Engineering*, *40*, 1554–1562.

Allen, L., Beijersbergen, M. W., Spreeuw, R., and Woerdman, J. (1992). Orbital angular momentum of light and the transformation of laguerre-gaussian laser modes. *Physical Review A*, *45*, 8185.

Andrews, L. C., and Phillips, R. L. (2005). *Laser beam propagation through random media* volume 10. SPIE press Bellingham.

Andrews, L. C., Phillips, R. L., Sasiela, R. J., and Parenti, R. R. (2006). Strehl ratio and scintillation theory for uplink gaussian-beam waves: beam wander effects. *Optical Engineering*, *45*, 076001–076001.

Banat, M. M. (2003). Statistical characterization of filtered phase noise in optical receivers. *Communications Letters, IEEE*, *7*, 85–87.

Bastiaans, M. (1979). Wigner distribution function and its application to first-order optics. *JOSA*, *69*, 1710–1716.

Beckers, J. M. (1993). Adaptive optics for astronomy-principles, performance, and applications. *Annual review of astronomy and astrophysics*, *31*, 13–62.

Beijersbergen, M., Allen, L., Van der Veen, H., and Woerdman, J. (2003). Astigmatic laser mode converters and transfer of orbital angular momentum. *Optical angular momentum*, *96*, 123–132.

Beland, R. R. (1995). Some aspects of propagation through weak isotropic non-kolmogorov turbulence. In *Photonics West'95* (pp. 6–16). International Society for Optics and Photonics.

Bhatia, A., and Wolf, E. (1954). On the circle polynomials of zernike and related orthogonal sets. In *Mathematical Proceedings of the Cambridge Philosophical Society* (pp. 40–48). Cambridge Univ Press volume 50.

Booker, H. G., Ratcliffe, J., and Shinn, D. (1950). Diffraction from an irregular screen with applications to ionospheric problems. *Philosophical Transactions of the Royal Society of London A: Mathematical, Physical and Engineering Sciences*, *242*, 579–607.

Boreman, G. D., and Dainty, C. (1996). Zernike expansions for non-kolmogorov turbulence. *JOSA A*, *13*, 517–522.

Born, M., and Wolf, E. (1964). Principles of optics electromagnetic theory of propagation. *Principles of Optics Electromagnetic Theory of Propagation, INterference and Diffraction of Light 2nd edition by Max Born, Emil Wolf New York, NY: Pergamon Press, 1964*, *1*.

Buades, A., Coll, B., and Morel, J.-M. (2005). A review of image denoising algorithms, with a new one. *Multiscale Modeling & Simulation*, *4*, 490–530.

Buser, R. (1971). Interferometric determination of the distance dependence of the phase structure function for near-ground horizontal propagation at 6328 å. *JOSA*, *61*, 488–491.

Charnotskii, M. (2013). Sparse spectrum model for a turbulent phase. *JOSA A*, *30*, 479–488.

Charnotskii, M., Myakinin, V., and Zavorotnyy, V. (1990). Observation of superresolution in nonisoplanatic imaging through turbulence. *JOSA A*, *7*, 1345–1350.

Conan, J.-M., Rousset, G., and Madec, P.-Y. (1995). Wave-front temporal spectra in high-resolution imaging through turbulence. *JOSA A*, *12*, 1559–1570.

Courtesy (2011). http://www.mvkonnik.info/2011/03/little-note-on-shack-hartmann-wavefront.html.

Dalaudier, F., Sidi, C., Crochet, M., and Vernin, J. (1994). Direct evidence of sheets in the atmospheric temperature field. *Journal of the Atmospheric Sciences*, *51*, 237–248.

van Dam, M. A., Lane, R. G. et al. (2002). Wave-front sensing from defocused images by use of wave-front slopes. *Applied optics*, *41*, 5497–5502.

Davis, C. C., Zhang, Y., Plett, M. L., Polak-Dingels, P., Barbier, P. R., and Rush, D. W. (1998). Characterization of a liquid-filled turbulence simulator. In *SPIE's International Symposium on Optical Science, Engineering, and Instrumentation* (pp. 38–49). International Society for Optics and Photonics.

Dayton, D., Gonglewski, J., Pierson, B., and Spielbusch, B. (1992). Atmospheric structure function measurements with a shack–hartmann wave-front sensor. *Optics letters*, *17*, 1737–1739.

Donnangelo, N. C., Drake, M. D., Bas, C. F., Rushanan, J. J., and Gervais, D. (2012). Generating identical numerical sequences utilizing a physical property and secure communication using such sequences. US Patent 8,189,785.

Drake, M. D., Bas, C. F., Gervais, D., Renda, P. F., Townsend, D., Rushanan, J. J., Francoeur, J., Donnangelo, N., and Stenner, M. D. (2013). Optical key distribution system using atmospheric turbulence as the randomness generating function: classical optical protocol for information assurance. *Optical Engineering*, *52*, 055008–055008.

Duparre, A., Ferre-Borrull, J., Gliech, S., Notni, G., Steinert, J., and Bennett, J. M. (2002). Surface characterization techniques for determining the root-mean-square roughness and power spectral densities of optical components. *Applied optics*, *41*, 154–171.

Fried, D. L. (1966). Optical resolution through a randomly inhomogeneous medium for very long and very short exposures. *JOSA*, *56*, 1372–1379.

Fried, D. L. (1977). Least-square fitting a wave-front distortion estimate to an array of phase-difference measurements. *JOSA*, *67*, 370–375.

Gadelmawla, E., Koura, M., Maksoud, T., Elewa, I., and Soliman, H. (2002). Roughness parameters. *Journal of Materials Processing Technology*, *123*, 133–145.

Geary, J. M. (1995). *Introduction to wavefront sensors*. SPIE Optical Engineering Press London.

Genoni, M. G., Paris, M. G., and Banaszek, K. (2007). Measure of the non-gaussian character of a quantum state. *Physical Review A*, *76*, 042327.

Greenwood, D. P. (1977). Bandwidth specification for adaptive optics systems. *JOSA*, *67*, 390–393.

Hardy, J. W. (1998). *Adaptive optics for astronomical telescopes*. Oxford University Press.

Herrmann, J. (1980). Least-squares wave front errors of minimum norm. *JOSA*, *70*, 28–35.

Hippler, S., Henning, T., Hormuth, F., Butler, D., and Brandner, W. (2004). Generation of atmosphere-like optical turbulence. *Appl. Opt*, *43*, 2813–2823.

Hudgin, R. H. (1977). Wave-front reconstruction for compensated imaging. *JOSA*, *67*, 375–378.

Ikeda, T., Popescu, G., Dasari, R. R., and Feld, M. S. (2005). Hilbert phase microscopy for investigating fast dynamics in transparent systems. *Optics letters*, *30*, 1165–1167.

Ishimaru, A. (1978). *Wave propagation and scattering in random media* volume 2. Academic press New York.

Jia, P., and Zhang, S. (2012). Simulation and fabrication of the atmospheric turbulence phase screen based on a fractal model. *Research in Astronomy and Astrophysics*, *12*, 584.

Kendall, M. G., and Yule, G. U. (1950). *An introduction to the theory of statistics*. Charles Griffin & Company.

Keskin, O., Jolissaint, L., and Bradley, C. (2006). Hot-air optical turbulence generator for the testing of adaptive optics systems: principles and characterization. *Applied optics*, *45*, 4888–4897.

Khrennikov, A. (2000). Non-kolmogorov probability models and modified bell's inequality. *Journal of Mathematical Physics*, *41*, 1768–1777.

Knepp, D. L. (1983). Multiple phase-screen calculation of the temporal behavior of stochastic waves. *Proceedings of the IEEE*, *71*, 722–737.

Kolmogorov, A. N. (1941). The local structure of turbulence in incompressible viscous fluid for very large reynolds numbers. In *Dokl. Akad. Nauk SSSR* (pp. 299–303). volume 30.

Korotkova, O., and Shchepakina, E. (2010). Color changes in stochastic light fields propagating in non-kolmogorov turbulence. *Optics letters*, *35*, 3772–3774.

Lane, R., and Tallon, M. (1992). Wave-front reconstruction using a shack-hartmann sensor. *Applied optics*, *31*, 6902–6908.

Li, J., Liu, J. Q., and Taylor, D. P. (2007). Optical communication using subcarrier psk intensity modulation through atmospheric turbulence channels. *Communications, IEEE Transactions on*, *55*, 1598–1606.

Lue, N., Choi, W., Popescu, G., Yaqoob, Z., Badizadegan, K., Dasari, R. R., and Feld, M. S. (2009). Live cell refractometry using hilbert phase microscopy and confocal reflectance microscopy. *The Journal of Physical Chemistry A*, *113*, 13327–13330.

Macaskill, C., and Ewart, T. (1984). Computer simulation of two-dimensional random wave propagation. *IMA journal of applied mathematics*, *33*, 1–15.

Mahajan, V. N. (1982). Strehl ratio for primary aberrations: some analytical results for circular and annular pupils. *JOSA*, *72*, 1258–1266.

Mahajan, V. N. (1983). Strehl ratio for primary aberrations in terms of their aberration variance. *JOSA*, *73*, 860–861.

Mahajan, V. N., and Shannon, R. R. (1994). *Zernike circle polynomials and optical aberrations of systems with circular pupils*. Optical Society of America.

Mantravadi, S. V., Rhoadarmer, T. A., and Glas, R. S. (2004). Simple laboratory system for generating well-controlled atmospheric-like turbulence. In *Optical Science and Technology, the SPIE 49th Annual Meeting* (pp. 290–300). International Society for Optics and Photonics.

Marangon, D. G., Vallone, G., and Villoresi, P. (2014). Random bits, true and unbiased, from atmospheric turbulence. *Scientific reports*, *4*.

Martin, J., and Flatté, S. M. (1988). Intensity images and statistics from numerical simulation of wave propagation in 3-d random media. *Applied Optics*, *27*, 2111–2126.

McAulay, A. D., and Li, J. (1999). Improving bandwidth for line-of-sight optical wireless in turbulent air by using phase conjugation. In *Photonics East'99* (pp. 32–39). International Society for Optics and Photonics.

Neal, D. R., Alford, W., and Gruetzner, J. K. (1999). Beam characterization by wavefront sensor. US Patent 5,936,720.

Neal, D. R., Alford, W. J., Gruetzner, J. K., and Warren, M. E. (1996). Amplitude and phase beam characterization using a two-dimensional wavefront sensor. In *Third International Workshop on Laser Beam and Optics Characterization* (pp. 72–82). International Society for Optics and Photonics.

Neal, D. R., Rammage, R. R., Armstrong, D. J., and Turner, W. T. (2000). Apparatus and method for characterizing pulsed light beams. US Patent 6,052,180.

Nistazakis, H. E., Tsiftsis, T. A., and Tombras, G. S. (2009). Performance analysis of free-space optical communication systems over atmospheric turbulence channels. *IET communications*, *3*, 1402–1409.

Noll, R. J. (1976). Zernike polynomials and atmospheric turbulence. *JOSA*, *66*, 207–211.

Paterson, C. (2005). Atmospheric turbulence and orbital angular momentum of single photons for optical communication. *Physical review letters*, *94*, 153901.

Perrin, M. D., Sivaramakrishnan, A., Makidon, R. B., Oppenheimer, B. R., and Graham, J. R. (2003). The structure of high strehl ratio point-spread functions. *The Astrophysical Journal*, *596*, 702.

Phillips, J. D., Goda, M. E., and Schmidt, J. (2005). Atmospheric turbulence simulation using liquid crystal spatial light modulators. In *Optics & Photonics 2005* (pp. 589406–589406). International Society for Optics and Photonics.

Popescu, G., Ikeda, T., Best, C. A., Badizadegan, K., Dasari, R. R., and Feld, M. S. (2005). Erythrocyte structure and dynamics quantified by hilbert phase microscopy. *Journal of biomedical optics*, *10*, 060503–060503.

Rampy, R., Gavel, D., Dillon, D., and Thomas, S. (2012). Production of phase screens for simulation of atmospheric turbulence. *Applied optics*, *51*, 8769–8778.

Rao, C., Jiang, W., and Ling, N. (2000). Spatial and temporal characterization of phase fluctuations in non-kolmogorov atmospheric turbulence. *Journal of Modern Optics*, *47*, 1111–1126.

Rhee, H.-G., Vorburger, T. V., Lee, J. W., and Fu, J. (2005). Discrepancies between roughness measurements obtained with phase-shifting and white-light interferometry. *Applied optics*, *44*, 5919–5927.

Rhoadarmer, T. A., Angel, J. R. P. et al. (2001). Low-cost, broadband static phase plate for generating atmospheric like turbulence. *Applied optics*, *40*, 2946–2955.

Rickett, B. J. (1990). Radio propagation through the turbulent interstellar plasma. *Annual review of astronomy and astrophysics*, *28*, 561–605.

Ricklin, J. C., and Davidson, F. M. (2003). Atmospheric optical communication with a gaussian schell beam. *JOSA A*, *20*, 856–866.

Roddier, F. (1981). V the effects of atmospheric turbulence in optical astronomy. *Progress in optics*, *19*, 281–376.

Roddier, F. (1999). *Adaptive optics in astronomy*. Cambridge university press.

Roddier, N. A. (1990). Atmospheric wavefront simulation using zernike polynomials. *Optical Engineering*, *29*, 1174–1180.

Roggemann, M. C., Welsh, B. M., and Hunt, B. R. (1996). *Imaging through turbulence*. CRC press.

Sasiela, R. J. (2007). *Electromagnetic wave propagation in turbulence: evaluation and application of Mellin transforms*. SPIE.

Schäfer, B., Lübbecke, M., and Mann, K. (2006). Hartmann-shack wave front measurements for real time determination of laser beam propagation parameters. *Review of scientific instruments*, *77*, 053103.

Schäfer, B., and Mann, K. (2000). Investigation of the propagation characteristics of excimer lasers using a hartmann–shack sensor. *Review of Scientific Instruments*, *71*, 2663–2668.

Schäfer, B., and Mann, K. (2002). Determination of beam parameters and coherence properties of laser radiation by use of an extended hartmann-shack wave-front sensor. *Applied optics*, *41*, 2809–2817.

Sedlaček, M., Podgornik, B., and Vižintin, J. (2012). Correlation between standard roughness parameters skewness and kurtosis and tribological behaviour of contact surfaces. *Tribology International*, *48*, 102–112.

Shapiro, J., and Strohbehn, J. (1978). Laser beam propagation in the atmosphere.

Shchepakina, E., and Korotkova, O. (2010). Second-order statistics of stochastic electromagnetic beams propagating through non-kolmogorov turbulence. *Optics express*, *18*, 10650–10658.

Siegman, A. E. (1990). New developments in laser resonators. In *OE/LASE'90, 14-19 Jan., Los Angeles, CA* (pp. 2–14). International Society for Optics and Photonics.

Simon, R., and Mukunda, N. (2000). Optical phase space, wigner representation, and invariant quality parameters. *JOSA A*, *17*, 2440–2463.

Simon, R., Mukunda, N., and Dutta, B. (1994). Quantum-noise matrix for multimode systems: U (n) invariance, squeezing, and normal forms. *Physical Review A*, *49*, 1567.

Southwell, W. H. (1980). Wave-front estimation from wave-front slope measurements. *JOSA*, *70*, 998–1006.

Stribling, B. E., Welsh, B. M., and Roggemann, M. C. (1995). Optical propagation in non-kolmogorov atmospheric turbulence. In *SPIE's 1995 Symposium on OE/Aerospace Sensing and Dual Use Photonics* (pp. 181–196). International Society for Optics and Photonics.

Strohbehn, J. W. (1968). Line-of-sight wave propagation through the turbulent atmosphere. *Proceedings of the IEEE*, *56*, 1301–1318.

Talmi, A., and Ribak, E. N. (2006). Wavefront reconstruction from its gradients. *JOSA A*, *23*, 288–297.

Tatarskii, V. I. (1961). Wave propagation in turbulent medium. *Wave Propagation in Turbulent Medium, by Valerian Ilich Tatarskii. Translated by RA Silverman. 285pp. Published by McGraw-Hill, 1961.*, *1*.

Tatarskii, V. I. (1971). *The effects of the turbulent atmosphere on wave propagation*. Nauka.

Thomas, S. (2004). A simple turbulence simulator for adaptive optics. In *Astronomical Telescopes and Instrumentation* (pp. 766–773). International Society for Optics and Photonics.

Thorlabs (2010). *Optical Wavefront Sensors (Shack-Hartmann Sensors)*. WFS Series Operation Manual.

Toselli, I., Andrews, L. C., Phillips, R. L., and Ferrero, V. (2007). Angle of arrival fluctuations for free space laser beam propagation through non kolmogorov turbulence. In *Defense and Security Symposium* (pp. 65510E–65510E). International Society for Optics and Photonics.

Toselli, I., Andrews, L. C., Phillips, R. L., and Ferrero, V. (2008). Free-space optical system performance for laser beam propagation through non-kolmogorov turbulence. *Optical Engineering*, *47*, 026003–026003.

Tubbs, R. N. (2003). Lucky exposures: Diffraction limited astronomical imaging through the atmosphere. *arXiv preprint astro-ph/0311481*, .

Tyson, R. (2010). *Principles of adaptive optics*. CRC press.

Tyson, R. K., and Frazier, B. W. (2004). *Field guide to adaptive optics* volume 2. SPIE Press.

Vorontsov, M., and Shmalgauzen, V. (1985). The principles of adaptive optics. *Moscow Izdatel Nauka*, *1*.

Wang, J., and Silva, D. (1980). Wave-front interpretation with zernike polynomials. *Applied optics*, *19*, 1510–1518.

Wright, D., Greve, P., Fleischer, J., and Austin, L. (1992). Laser beam width, divergence and beam propagation factor - an international standardization approach. *Optical and Quantum Electronics*, *24*, S993–S1000.

Wu, G., Guo, H., Yu, S., and Luo, B. (2010). Spreading and direction of gaussian–schell model beam through a non-kolmogorov turbulence. *Optics letters*, *35*, 715–717.

Xue, L., Lai, J., Wang, S., and Li, Z. (2011). Single-shot slightly-off-axis interferometry based hilbert phase microscopy of red blood cells. *Biomedical optics express*, *2*, 987–995.

Zhu, X., and Kahn, J. M. (2002). Free-space optical communication through atmospheric turbulence channels. *Communications, IEEE Transactions on*, *50*, 1293–1300.

Zilberman, A., Golbraikh, E., and Kopeika, N. S. (2008). Propagation of electromagnetic waves in kolmogorov and non-kolmogorov atmospheric turbulence: three-layer altitude model. *Applied optics*, *47*, 6385–6391.

APPENDIX A

Error calculation

The error in calculation of slopes of linear curves (shown in Chapter 2) has been done in the following manner :

For a variable y plotted with respect to x, such that $y = f(x)$, one usually represents the absolute error δy in a plot as :

$$y_i = f(x_i) \pm \delta y_i \tag{A.1}$$

with δy_i being the standard deviation with respect to mean value of y_i for the x_i^{th} point, i.e. :

$$\delta y_i = \sqrt{\frac{1}{N}\sum_{i=1}^{N}\left(y_i - \langle y_i \rangle\right)^2} \tag{A.2}$$

N is the total number of data points collected for the x_i^{th} point.

On a logarithmic scale though, instead of representing the absolute error discussed above, a relative error is calculated. This is done in the following manner :

$$\begin{aligned}
\text{Let,} \qquad & z_i = log_{10}(y_i) \qquad (A.3)\\
\Longrightarrow & \delta z_i = \delta(log_{10}(y_i))\\
\text{for small error,} \quad \Longrightarrow & dz_i \approx d(log_{10}(y_i))\\
\Longrightarrow & dz_i = \frac{1}{2.303} d(ln(y_i))\\
\Longrightarrow & dz_i = 0.434\frac{dy_i}{y_i}\\
\Longrightarrow & dz_i \approx 0.434\frac{\delta y_i}{y_i} \qquad (A.4)
\end{aligned}$$

Therefore, Eqn. (A.4) is used for the calculation of error in the log scale graphs for $log_{10}D_{\phi(r)}$ Vs. $log_{10}(r)$ with r being x and $D_{\phi(r)}$ being y (as has been referred above).

Now, once the error has been calculated and represented on the said graphs, the uncertainty in the measured slope is calculated in the following manner :

- The respective slopes for the best fitted lines obtained with minimum and maximum relative error points are calculated.
- The uncertainty is then calculated as :

$$uncert = 0.5 * (slope_{max} - slope_{min}) \tag{A.5}$$

This has been shown with $\pm$ in all the calculated slopes in graphs as well as tables in Chapter 2.

APPENDIX B

Some Important Deductions

B.1 $\Delta\hat{\xi}$ Commutation Relations

The commutation relationships between the elements of the matrix $\Delta\hat{\xi}$:

$$\begin{aligned}\left[\Delta\hat{\xi}_1, \Delta\hat{\xi}_1\right] &= \Delta\hat{\xi}_1\Delta\hat{\xi}_1 - \Delta\hat{\xi}_1\Delta\hat{\xi}_1 \\ &= \Delta\hat{x}\Delta\hat{x} - \Delta\hat{x}\Delta\hat{x} \\ &= 0 \end{aligned} \tag{B.1}$$

$$\begin{aligned}\left[\Delta\hat{\xi}_1, \Delta\hat{\xi}_2\right] &= \Delta\hat{\xi}_1\Delta\hat{\xi}_2 - \Delta\hat{\xi}_2\Delta\hat{\xi}_1 \\ &= \Delta\hat{x}\Delta\hat{p_x} - \Delta\hat{p_x}\Delta\hat{x} \\ &= \left(\hat{x} - \langle\hat{x}\rangle\right)\left(\hat{p_x} - \langle\hat{p_x}\rangle\right) - \left(\hat{p_x} - \langle\hat{p_x}\rangle\right)\left(\hat{x} - \langle\hat{x}\rangle\right) \\ &= \hat{x}\hat{p_x} - \hat{x}\langle\hat{p_x}\rangle - \hat{p_x}\langle\hat{x}\rangle + \langle\hat{x}\rangle\langle\hat{p_x}\rangle - \left(\hat{p_x}\hat{x} - \hat{p_x}\langle\hat{x}\rangle - \hat{x}\langle\hat{p_x}\rangle + \langle\hat{p_x}\rangle\langle\hat{x}\rangle\right) \\ &= \hat{x}\hat{p_x} - \hat{p_x}\hat{x} \\ &= i\text{ƛ} \end{aligned} \tag{B.2}$$

$$\begin{aligned}\left[\Delta\hat{\xi}_1, \Delta\hat{\xi}_3\right] &= \Delta\hat{\xi}_1\Delta\hat{\xi}_3 - \Delta\hat{\xi}_3\Delta\hat{\xi}_1 \\ &= \Delta\hat{x}\Delta\hat{y} - \Delta\hat{y}\Delta\hat{x} \\ &= \left(\hat{x} - \langle\hat{x}\rangle\right)\left(\hat{y} - \langle\hat{y}\rangle\right) - \left(\hat{y} - \langle\hat{y}\rangle\right)\left(\hat{x} - \langle\hat{x}\rangle\right) \\ &= \hat{x}\hat{y} - \hat{x}\langle\hat{y}\rangle - \hat{y}\langle\hat{x}\rangle + \langle\hat{x}\rangle\langle\hat{y}\rangle - \left(\hat{y}\hat{x} - \hat{y}\langle\hat{x}\rangle - \hat{x}\langle\hat{y}\rangle + \langle\hat{y}\rangle\langle\hat{x}\rangle\right) \\ &= \hat{x}\hat{y} - \hat{y}\hat{x} \\ &= 0 \end{aligned} \tag{B.3}$$

$$\left[\Delta\hat{\xi}_1, \Delta\hat{\xi}_4\right] = \Delta\hat{\xi}_1\Delta\hat{\xi}_4 - \Delta\hat{\xi}_4\Delta\hat{\xi}_1$$
$$= \Delta\hat{x}\Delta\hat{p_y} - \Delta\hat{p_y}\Delta\hat{x}$$
$$= (\hat{x} - \langle\hat{x}\rangle)(\hat{p_y} - \langle\hat{p_y}\rangle) - (\hat{p_y} - \langle\hat{p_y}\rangle)(\hat{x} - \langle\hat{x}\rangle)$$
$$= \hat{x}\hat{p_y} - \hat{x}\langle\hat{p_y}\rangle - \hat{p_y}\langle\hat{x}\rangle + \langle\hat{x}\rangle\langle\hat{p_y}\rangle - (\hat{p_y}\hat{x} - \hat{p_y}\langle\hat{x}\rangle - \hat{x}\langle\hat{p_y}\rangle + \langle\hat{p_y}\rangle\langle\hat{x}\rangle)$$
$$= \hat{x}\hat{p_y} - \hat{p_y}\hat{x}$$
$$= 0 \tag{B.4}$$

$$\left[\Delta\hat{\xi}_2, \Delta\hat{\xi}_1\right] = \Delta\hat{\xi}_2\Delta\hat{\xi}_1 - \Delta\hat{\xi}_1\Delta\hat{\xi}_2$$
$$= \Delta\hat{p_x}\Delta\hat{x} - \Delta\hat{x}\Delta\hat{p_x}$$
$$= (\hat{p_x} - \langle\hat{p_x}\rangle)(\hat{x} - \langle\hat{x}\rangle) - (\hat{x} - \langle\hat{x}\rangle)(\hat{p_x} - \langle\hat{p_x}\rangle)$$
$$= \hat{p_x}\hat{x} - \hat{p_x}\langle\hat{x}\rangle - \hat{x}\langle\hat{p_x}\rangle + \langle\hat{p_x}\rangle\langle\hat{x}\rangle - (\hat{x}\hat{p_x} - \hat{x}\langle\hat{p_x}\rangle - \hat{p_x}\langle\hat{x}\rangle + \langle\hat{x}\rangle\langle\hat{p_x}\rangle)$$
$$= \hat{p_x}\hat{x} - \hat{x}\hat{p_x}$$
$$= -i\hbar \tag{B.5}$$

$$\left[\Delta\hat{\xi}_2, \Delta\hat{\xi}_2\right] = \Delta\hat{\xi}_2\Delta\hat{\xi}_2 - \Delta\hat{\xi}_2\Delta\hat{\xi}_2$$
$$= \Delta\hat{p_x}\Delta\hat{p_x} - \Delta\hat{p_x}\Delta\hat{p_x}$$
$$= 0 \tag{B.6}$$

$$\left[\Delta\hat{\xi}_2, \Delta\hat{\xi}_3\right] = \Delta\hat{\xi}_2\Delta\hat{\xi}_3 - \Delta\hat{\xi}_3\Delta\hat{\xi}_2$$
$$= \Delta\hat{p_x}\Delta\hat{y} - \Delta\hat{y}\Delta\hat{p_x}$$
$$= (\hat{p_x} - \langle\hat{p_x}\rangle)(\hat{y} - \langle\hat{y}\rangle) - (\hat{y} - \langle\hat{y}\rangle)(\hat{p_x} - \langle\hat{p_x}\rangle)$$
$$= \hat{p_x}\hat{y} - \hat{p_x}\langle\hat{y}\rangle - \hat{y}\langle\hat{p_x}\rangle + \langle\hat{p_x}\rangle\langle\hat{y}\rangle - (\hat{y}\hat{p_x} - \hat{y}\langle\hat{p_x}\rangle - \hat{p_x}\langle\hat{y}\rangle + \langle\hat{y}\rangle\langle\hat{p_x}\rangle)$$
$$= \hat{p_x}\hat{y} - \hat{y}\hat{p_x}$$
$$= 0 \tag{B.7}$$

$$\left[\Delta\hat{\xi}_2, \Delta\hat{\xi}_4\right] = \Delta\hat{\xi}_2\Delta\hat{\xi}_4 - \Delta\hat{\xi}_4\Delta\hat{\xi}_2$$
$$= \Delta\hat{p_x}\Delta\hat{p_y} - \Delta\hat{p_y}\Delta\hat{p_x}$$
$$= (\hat{p_x} - \langle\hat{p_x}\rangle)(\hat{p_y} - \langle\hat{p_y}\rangle) - (\hat{p_y} - \langle\hat{p_y}\rangle)(\hat{p_x} - \langle\hat{p_x}\rangle)$$
$$= \hat{p_x}\hat{p_y} - \hat{p_x}\langle\hat{p_y}\rangle - \hat{p_y}\langle\hat{p_x}\rangle + \langle\hat{p_x}\rangle\langle\hat{p_y}\rangle - (\hat{p_y}\hat{p_x} - \hat{p_y}\langle\hat{p_x}\rangle - \hat{p_x}\langle\hat{p_y}\rangle + \langle\hat{p_y}\rangle\langle\hat{p_x}\rangle)$$
$$= \hat{p_x}\hat{p_y} - \hat{p_y}\hat{p_x}$$
$$= 0 \tag{B.8}$$

$$\begin{aligned}
\left[\Delta\hat{\xi}_3, \Delta\hat{\xi}_1\right] &= \Delta\hat{\xi}_3\Delta\hat{\xi}_1 - \Delta\hat{\xi}_1\Delta\hat{\xi}_3 \\
&= \Delta\hat{y}\Delta\hat{x} - \Delta\hat{x}\Delta\hat{y} \\
&= (\hat{y} - \langle\hat{y}\rangle)(\hat{x} - \langle\hat{x}\rangle) - (\hat{x} - \langle\hat{x}\rangle)(\hat{y} - \langle\hat{y}\rangle) \\
&= \hat{y}\hat{x} - \hat{y}\langle\hat{x}\rangle - \hat{x}\langle\hat{y}\rangle + \langle\hat{y}\rangle\langle\hat{x}\rangle - (\hat{x}\hat{y} - \hat{x}\langle\hat{y}\rangle - \hat{y}\langle\hat{x}\rangle + \langle\hat{x}\rangle\langle\hat{y}\rangle) \\
&= \hat{y}\hat{x} - \hat{x}\hat{y} \\
&= 0 \qquad \text{(B.9)} \\
\left[\Delta\hat{\xi}_3, \Delta\hat{\xi}_2\right] &= \Delta\hat{\xi}_3\Delta\hat{\xi}_2 - \Delta\hat{\xi}_2\Delta\hat{\xi}_3 \\
&= \Delta\hat{y}\Delta\hat{p_x} - \Delta\hat{p_x}\Delta\hat{y} \\
&= (\hat{y} - \langle\hat{y}\rangle)(\hat{p_x} - \langle\hat{p_x}\rangle) - (\hat{p_x} - \langle\hat{p_x}\rangle)(\hat{y} - \langle\hat{y}\rangle) \\
&= \hat{y}\hat{p_x} - \hat{y}\langle\hat{p_x}\rangle - \hat{p_x}\langle\hat{y}\rangle + \langle\hat{y}\rangle\langle\hat{p_x}\rangle - (\hat{p_x}\hat{y} - \hat{p_x}\langle\hat{y}\rangle - \hat{y}\langle\hat{p_x}\rangle + \langle\hat{p_x}\rangle\langle\hat{y}\rangle) \\
&= \hat{y}\hat{p_x} - \hat{p_x}\hat{y} \\
&= 0 \qquad \text{(B.10)} \\
\left[\Delta\hat{\xi}_3, \Delta\hat{\xi}_3\right] &= \Delta\hat{\xi}_3\Delta\hat{\xi}_3 - \Delta\hat{\xi}_3\Delta\hat{\xi}_3 \\
&= \Delta\hat{y}\Delta\hat{y} - \Delta\hat{y}\Delta\hat{y} \\
&= 0 \qquad \text{(B.11)} \\
\left[\Delta\hat{\xi}_3, \Delta\hat{\xi}_4\right] &= \Delta\hat{\xi}_3\Delta\hat{\xi}_4 - \Delta\hat{\xi}_4\Delta\hat{\xi}_3 \\
&= \Delta\hat{y}\Delta\hat{p_y} - \Delta\hat{p_y}\Delta\hat{y} \\
&= (\hat{y} - \langle\hat{y}\rangle)(\hat{p_y} - \langle\hat{p_y}\rangle) - (\hat{p_y} - \langle\hat{p_y}\rangle)(\hat{y} - \langle\hat{y}\rangle) \\
&= \hat{y}\hat{p_y} - \hat{y}\langle\hat{p_y}\rangle - \hat{p_y}\langle\hat{y}\rangle + \langle\hat{y}\rangle\langle\hat{p_y}\rangle - (\hat{p_y}\hat{y} - \hat{p_y}\langle\hat{y}\rangle - \hat{y}\langle\hat{p_y}\rangle + \langle\hat{p_y}\rangle\langle\hat{y}\rangle) \\
&= \hat{y}\hat{p_y} - \hat{p_y}\hat{y} \\
&= i\hbar \qquad \text{(B.12)} \\
\left[\Delta\hat{\xi}_4, \Delta\hat{\xi}_1\right] &= \Delta\hat{\xi}_4\Delta\hat{\xi}_1 - \Delta\hat{\xi}_1\Delta\hat{\xi}_4 \\
&= \Delta\hat{p_y}\Delta\hat{x} - \Delta\hat{x}\Delta\hat{p_y} \\
&= (\hat{p_y} - \langle\hat{p_y}\rangle)(\hat{x} - \langle\hat{x}\rangle) - (\hat{x} - \langle\hat{x}\rangle)(\hat{p_y} - \langle\hat{p_y}\rangle) \\
&= \hat{p_y}\hat{x} - \hat{p_y}\langle\hat{x}\rangle - \hat{x}\langle\hat{p_y}\rangle + \langle\hat{p_y}\rangle\langle\hat{x}\rangle - (\hat{x}\hat{p_y} - \hat{x}\langle\hat{p_y}\rangle - \hat{p_y}\langle\hat{x}\rangle + \langle\hat{x}\rangle\langle\hat{p_y}\rangle) \\
&= \hat{p_y}\hat{x} - \hat{x}\hat{p_y} \\
&= 0 \qquad \text{(B.13)}
\end{aligned}$$

$$\begin{aligned}
\left[\Delta\hat{\xi}_4, \Delta\hat{\xi}_2\right] &= \Delta\hat{\xi}_4\Delta\hat{\xi}_2 - \Delta\hat{\xi}_2\Delta\hat{\xi}_4 \\
&= \Delta\hat{p_y}\Delta\hat{p_x} - \Delta\hat{p_x}\Delta\hat{p_y} \\
&= \left(\hat{p_y} - \langle\hat{p_y}\rangle\right)\left(\hat{p_x} - \langle\hat{p_x}\rangle\right) - \left(\hat{p_x} - \langle\hat{p_x}\rangle\right)\left(\hat{p_y} - \langle\hat{p_y}\rangle\right) \\
&= \hat{p_y}\hat{p_x} - \hat{p_y}\langle\hat{p_x}\rangle - \hat{p_x}\langle\hat{p_y}\rangle + \langle\hat{p_y}\rangle\langle\hat{p_x}\rangle - \left(\hat{p_x}\hat{p_y} - \hat{p_x}\langle\hat{p_y}\rangle - \hat{p_y}\langle\hat{p_x}\rangle + \langle\hat{p_x}\rangle\langle\hat{p_y}\rangle\right) \\
&= \hat{p_y}\hat{p_x} - \hat{p_x}\hat{p_y} \\
&= 0 \qquad \text{(B.14)} \\
\left[\Delta\hat{\xi}_4, \Delta\hat{\xi}_3\right] &= \Delta\hat{\xi}_4\Delta\hat{\xi}_3 - \Delta\hat{\xi}_3\Delta\hat{\xi}_4 \\
&= \Delta\hat{p_y}\Delta\hat{y} - \Delta\hat{y}\Delta\hat{p_y} \\
&= \left(\hat{p_y} - \langle\hat{p_y}\rangle\right)\left(\hat{y} - \langle\hat{y}\rangle\right) - \left(\hat{y} - \langle\hat{y}\rangle\right)\left(\hat{p_y} - \langle\hat{p_y}\rangle\right) \\
&= \hat{p_y}\hat{y} - \hat{p_y}\langle\hat{y}\rangle - \hat{y}\langle\hat{p_y}\rangle + \langle\hat{p_y}\rangle\langle\hat{y}\rangle - \left(\hat{y}\hat{p_y} - \hat{y}\langle\hat{p_y}\rangle - \hat{p_y}\langle\hat{y}\rangle + \langle\hat{y}\rangle\langle\hat{p_y}\rangle\right) \\
&= \hat{p_y}\hat{y} - \hat{y}\hat{p_y} \\
&= -i\text{ƛ} \qquad \text{(B.15)} \\
\left[\Delta\hat{\xi}_4, \Delta\hat{\xi}_4\right] &= \Delta\hat{\xi}_4\Delta\hat{\xi}_4 - \Delta\hat{\xi}_4\Delta\hat{\xi}_4 \\
&= \Delta\hat{p_y}\Delta\hat{p_y} - \Delta\hat{p_y}\Delta\hat{p_y} \\
&= 0 \qquad \text{(B.16)}
\end{aligned}$$

B.2 Simplification of V

1. The term $\langle(\Delta\hat{x})^2\rangle$:

$$\begin{aligned}
\langle(\Delta\hat{x})^2\rangle &= \langle\left(\hat{x} - \langle\hat{x}\rangle\right)\left(\hat{x} - \langle\hat{x}\rangle\right)\rangle \\
&= \langle\left(\hat{x}^2 - \hat{x}\langle\hat{x}\rangle - \hat{x}\langle\hat{x}\rangle + \langle\hat{x}\rangle^2\right)\rangle \\
&= \langle\hat{x}^2\rangle - \langle\hat{x}\rangle\langle\hat{x}\rangle - \langle\hat{x}\rangle\langle\hat{x}\rangle + \langle\hat{x}\rangle^2 \\
&= \langle\hat{x}^2\rangle - 2\langle\hat{x}\rangle^2 + \langle\hat{x}\rangle^2 \\
&= \langle\hat{x}^2\rangle - \langle\hat{x}\rangle^2 \\
&= \langle\hat{x}^2\rangle - (c_1)^2 \qquad \text{(B.17)}
\end{aligned}$$

where, it should be noted that $\langle\hat{x}\rangle = c_1$ has been defined.

2. The term $\langle(\Delta\hat{y})^2\rangle$:

$$\begin{aligned}\langle(\Delta\hat{y})^2\rangle &= \langle\hat{y}^2\rangle - \langle\hat{y}\rangle^2 \\ &= \langle\hat{y}^2\rangle - (c_2)^2 \end{aligned} \tag{B.18}$$

where, $\langle\hat{y}\rangle = c_2$.

3. The term $\langle(\Delta\hat{p}_x)^2\rangle$:

$$\begin{aligned}\langle(\Delta\hat{p}_x)^2\rangle &= \langle(\hat{p}_x - \langle\hat{p}_x\rangle)(\hat{p}_x - \langle\hat{p}_x\rangle)\rangle \\ &= \langle\big(\hat{p}_x^2 - \hat{p}_x\langle\hat{p}_x\rangle - \hat{p}_x\langle\hat{p}_x\rangle + \langle\hat{p}_x\rangle^2\big)\rangle \\ &= \langle\hat{p}_x^2\rangle - \langle\hat{p}_x\rangle\langle\hat{p}_x\rangle - \langle\hat{p}_x\rangle\langle\hat{p}_x\rangle + \langle\hat{p}_x\rangle^2 \\ &= \langle\hat{p}_x^2\rangle - 2\langle\hat{p}_x\rangle^2 + \langle\hat{p}_x\rangle^2 \\ &= \langle\hat{p}_x^2\rangle - \langle\hat{p}_x\rangle^2 \\ &= \langle\hat{p}_x^2\rangle - (c_3)^2 \end{aligned} \tag{B.19}$$

where again, $\langle\hat{p}_x\rangle = c_3$ has been defined.

4. The term $\langle(\Delta\hat{p}_y)^2\rangle$:

$$\begin{aligned}\langle(\Delta\hat{p}_y)^2\rangle &= \langle\hat{p}_y^2\rangle - \langle\hat{p}_y\rangle^2 \\ &= \langle\hat{p}_y^2\rangle - (c_4)^2 \end{aligned} \tag{B.20}$$

where, $\langle\hat{p}_y\rangle = c_4$.

5. The term $\langle\frac{1}{2}\{\Delta\hat{x},\Delta\hat{p}_x\}\rangle$:

$$\begin{aligned}
\langle\frac{1}{2}\{\Delta\hat{x},\Delta\hat{p}_x\}\rangle &= \langle\frac{1}{2}\{\Delta\hat{p}_x,\Delta\hat{x}\}\rangle = \frac{1}{2}\left(\langle(\hat{x}-\langle\hat{x}\rangle)\left(\hat{p}_x-\langle\hat{p}_x\rangle\right)+\left(\hat{p}_x-\langle\hat{p}_x\rangle\right)\left(\hat{x}-\langle\hat{x}\rangle\right)\rangle\right)\\
&= \frac{1}{2}\left(\langle(\hat{x}\hat{p}_x-\hat{p}_x\langle\hat{x}\rangle-\hat{x}\langle\hat{p}_x\rangle+\langle\hat{x}\rangle\langle\hat{p}_x\rangle)+(\hat{p}_x\hat{x}-\hat{x}\langle\hat{p}_x\rangle-\hat{p}_x\langle\hat{x}\rangle+\langle\hat{p}_x\rangle\langle\hat{x}\rangle)\rangle\right)\\
&= \frac{1}{2}(\langle\hat{x}\hat{p}_x\rangle-\langle\hat{p}_x\rangle\langle\hat{x}\rangle-\langle\hat{x}\rangle\langle\hat{p}_x\rangle+\langle\hat{x}\rangle\langle\hat{p}_x\rangle+\langle\hat{x}\hat{p}_x\rangle\\
&\quad-\langle\hat{p}_x\rangle\langle\hat{x}\rangle-\langle\hat{x}\rangle\langle\hat{p}_x\rangle+\langle\hat{x}\rangle\langle\hat{p}_x\rangle)\\
&= \frac{1}{2}\left(\langle\hat{x}\hat{p}_x\rangle-4\langle\hat{x}\rangle\langle\hat{p}_x\rangle+\langle\hat{p}_x\hat{x}\rangle+2\langle\hat{x}\rangle\langle\hat{p}_x\rangle\right)\\
&= \frac{1}{2}\left(\langle\hat{x}\hat{p}_x\rangle+\langle\hat{p}_x\hat{x}\rangle-2\langle\hat{x}\rangle\langle\hat{p}_x\rangle\right)\\
&= \frac{1}{2}\left(\langle\hat{x}\hat{p}_x\rangle+\langle\hat{p}_x\hat{x}\rangle\right)-(c_1c_3)\\
&= \frac{1}{2}\left(\langle\hat{x}\hat{p}_x+\hat{p}_x\hat{x}\rangle\right)-(c_1c_3)\\
&= \langle\frac{1}{2}\{\hat{x},\hat{p}_x\}\rangle-(c_1c_3)
\end{aligned}\tag{B.21}$$

6. The term $\langle\frac{1}{2}\{\Delta\hat{y},\Delta\hat{p}_y\}\rangle$:

$$\begin{aligned}
\langle\frac{1}{2}\{\Delta\hat{y},\Delta\hat{p}_y\}\rangle &= \langle\frac{1}{2}\{\Delta\hat{p}_y,\Delta\hat{y}\}\rangle = \frac{1}{2}\left(\langle\hat{y}\hat{p}_y\rangle+\langle\hat{p}_y\hat{y}\rangle\right)-2\langle\hat{y}\rangle\langle\hat{p}_y\rangle\\
&= \frac{1}{2}\left(\langle\hat{y}\hat{p}_y+\hat{p}_y\hat{y}\rangle\right)-(c_2c_4)\\
&= \langle\frac{1}{2}\{\hat{y},\hat{p}_y\}\rangle-(c_1c_3)
\end{aligned}\tag{B.22}$$

7. The term $\langle\Delta\hat{x}\Delta\hat{y}\rangle$:

$$\begin{aligned}
\langle\Delta\hat{x}\Delta\hat{y}\rangle &= \langle\Delta\hat{y}\Delta\hat{x}\rangle = \langle(\hat{x}-\langle\hat{x}\rangle)\left(\hat{y}-\langle\hat{y}\rangle\right)\rangle\\
&= \langle(\hat{x}\hat{y}-\hat{x}\langle\hat{y}\rangle-\hat{y}\langle\hat{x}\rangle+\langle\hat{x}\rangle\langle\hat{y}\rangle)\rangle\\
&= \langle\hat{x}\hat{y}\rangle-\langle\hat{x}\rangle\langle\hat{y}\rangle-\langle\hat{y}\rangle\langle\hat{x}\rangle+\langle\hat{x}\rangle\langle\hat{y}\rangle\\
&= \langle\hat{x}\hat{y}\rangle-2\langle\hat{x}\rangle\langle\hat{y}\rangle+\langle\hat{x}\rangle\langle\hat{y}\rangle\\
&= \langle\hat{x}\hat{y}\rangle-\langle\hat{x}\rangle\langle\hat{y}\rangle\\
&= \langle\hat{x}\hat{y}\rangle-(c_1c_2)
\end{aligned}\tag{B.23}$$

8. The term $\langle \Delta\hat{x}\Delta\hat{p}_y \rangle$:

$$\begin{aligned}
\langle \Delta\hat{x}\Delta\hat{p}_y \rangle &= \langle \Delta\hat{p}_y\Delta\hat{x} \rangle = \langle (\hat{x} - \langle \hat{x} \rangle)\,(\hat{p}_y - \langle \hat{p}_y \rangle) \rangle \\
&= \langle (\hat{x}\hat{p}_y - \hat{x}\langle \hat{p}_y \rangle - \hat{p}_y\langle \hat{x} \rangle + \langle \hat{x} \rangle\langle \hat{p}_y \rangle) \rangle \\
&= \langle \hat{x}\hat{p}_y \rangle - \langle \hat{x} \rangle\langle \hat{p}_y \rangle - \langle \hat{p}_y \rangle\langle \hat{x} \rangle + \langle \hat{x} \rangle\langle \hat{p}_y \rangle \\
&= \langle \hat{x}\hat{p}_y \rangle - 2\langle \hat{x} \rangle\langle \hat{p}_y \rangle + \langle \hat{x} \rangle\langle \hat{p}_y \rangle \\
&= \langle \hat{x}\hat{p}_y \rangle - \langle \hat{x} \rangle\langle \hat{p}_y \rangle \\
&= \langle \hat{x}\hat{p}_y \rangle - (c_1 c_4)
\end{aligned} \tag{B.24}$$

9. The term $\langle \Delta\hat{y}\Delta\hat{p}_x \rangle$:

$$\begin{aligned}
\langle \Delta\hat{y}\Delta\hat{p}_x \rangle &= \langle \Delta\hat{p}_x\Delta\hat{y} \rangle = \langle (\hat{y} - \langle \hat{y} \rangle)\,(\hat{p}_x - \langle \hat{p}_x \rangle) \rangle \\
&= \langle (\hat{y}\hat{p}_x - \hat{y}\langle \hat{p}_x \rangle - \hat{p}_x\langle \hat{y} \rangle + \langle \hat{y} \rangle\langle \hat{p}_x \rangle) \rangle \\
&= \langle \hat{y}\hat{p}_x \rangle - \langle \hat{y} \rangle\langle \hat{p}_x \rangle - \langle \hat{p}_x \rangle\langle \hat{y} \rangle + \langle \hat{y} \rangle\langle \hat{p}_x \rangle \\
&= \langle \hat{y}\hat{p}_x \rangle - 2\langle \hat{y} \rangle\langle \hat{p}_x \rangle + \langle \hat{y} \rangle\langle \hat{p}_x \rangle \\
&= \langle \hat{y}\hat{p}_x \rangle - \langle \hat{y} \rangle\langle \hat{p}_x \rangle \\
&= \langle \hat{y}\hat{p}_x \rangle - (c_2 c_3)
\end{aligned} \tag{B.25}$$

10. The term $\langle \Delta\hat{p}_x\Delta\hat{p}_y \rangle$:

$$\begin{aligned}
\langle \Delta\hat{p}_x\Delta\hat{p}_y \rangle &= \langle \Delta\hat{p}_y\Delta\hat{p}_x \rangle = \langle (\hat{p}_x - \langle \hat{p}_x \rangle)\,(\hat{p}_y - \langle \hat{p}_y \rangle) \rangle \\
&= \langle (\hat{p}_x\hat{p}_y - \hat{p}_y\langle \hat{p}_x \rangle - \hat{p}_x\langle \hat{p}_y \rangle + \langle \hat{p}_x \rangle\langle \hat{p}_y \rangle) \rangle \\
&= \langle \hat{p}_x\hat{p}_y \rangle - \langle \hat{p}_y \rangle\langle \hat{p}_x \rangle - \langle \hat{p}_x \rangle\langle \hat{p}_y \rangle + \langle \hat{p}_x \rangle\langle \hat{p}_y \rangle \\
&= \langle \hat{p}_x\hat{p}_y \rangle - 2\langle \hat{p}_x \rangle\langle \hat{p}_y \rangle + \langle \hat{p}_x \rangle\langle \hat{p}_y \rangle \\
&= \langle \hat{p}_x\hat{p}_y \rangle - \langle \hat{p}_x \rangle\langle \hat{p}_y \rangle \\
&= \langle \hat{p}_x\hat{p}_y \rangle - (c_3 c_4)
\end{aligned} \tag{B.26}$$

B.3 Proof of the Uncertainty Principle

Invoking the Schwarz inequality for any two states α and β,

$$\langle \alpha|\alpha \rangle\langle \beta|\beta \rangle \geq |\langle \alpha|\beta \rangle|^2 \tag{B.27}$$

Taking the state $|\alpha\rangle = \Delta\hat{x}|\psi\rangle$ and $|\beta\rangle = \Delta\hat{p_x}|\psi\rangle$ (where $\psi(x,y)$ is as defined in Eqn. (3.19)),

$$\begin{aligned}(|\alpha\rangle)^\dagger &= (\Delta\hat{x}|\psi\rangle)^\dagger \\ &= (|\psi\rangle)^\dagger (\Delta\hat{x})^\dagger \\ &= \langle\psi|\Delta\hat{x}\end{aligned}$$

where, $\langle\psi| = |\psi\rangle^\dagger$, i.e. conjugate transpose of $|\psi\rangle$ and $(\Delta\hat{x})^\dagger = (\Delta\hat{x})$. Similarly,

$$\begin{aligned}(|\beta\rangle)^\dagger &= (\Delta\hat{p_x}|\psi\rangle)^\dagger \\ &= (|\psi\rangle)^\dagger (\Delta\hat{p_x})^\dagger \\ &= \langle\psi|\Delta\hat{p_x}\end{aligned}$$

since, $(\Delta\hat{p}_x)^\dagger = (\Delta\hat{p}_x)$.

On account of the above equations, the Schwarz inequality can be rewritten as :

$$\begin{aligned}\langle\psi|\left(\Delta\hat{x}\right)^2|\psi\rangle\langle\psi|\left(\Delta\hat{p_x}\right)^2|\psi\rangle &\geq |\langle\psi|\Delta\hat{x}\Delta\hat{p_x}|\psi\rangle|^2 \\ \Longrightarrow\langle\left(\Delta\hat{x}\right)^2\rangle\langle\left(\Delta\hat{p_x}\right)^2\rangle &\geq |\langle\Delta\hat{x}|\Delta\hat{p_x}\rangle|^2 \qquad \text{(B.28)}\end{aligned}$$

The term $|\langle\Delta\hat{x}\Delta\hat{p_x}\rangle|^2$ in the RHS of above equation can be expanded in terms of commutator and anti commutator brackets in the following manner :

$$\begin{aligned}\Delta\hat{x}\Delta\hat{p_x} &= \frac{1}{2}\{\Delta\hat{x},\Delta\hat{p_x}\} + \frac{1}{2}[\Delta\hat{x},\Delta\hat{p_x}] \\ \Longrightarrow\langle\Delta\hat{x}\Delta\hat{p_x}\rangle &= \frac{1}{2}\langle\{\Delta\hat{x},\Delta\hat{p_x}\}\rangle + \frac{1}{2}\langle[\Delta\hat{x},\Delta\hat{p_x}]\rangle \\ \Longrightarrow|\langle\Delta\hat{x}\Delta\hat{p_x}\rangle|^2 &= \frac{1}{4}|\langle\{\Delta\hat{x},\Delta\hat{p_x}\}\rangle|^2 + \frac{1}{4}|\langle[\Delta\hat{x},\Delta\hat{p_x}]\rangle|^2. \qquad \text{(B.29)}\end{aligned}$$

Keeping in view the Eqns. (3.30),(3.31) and Eqn. (B.2), Eqn. (B.29) becomes :

$$|\langle\Delta\hat{x}\Delta\hat{p_x}\rangle|^2 = \frac{1}{4}|\langle\{\Delta\hat{x},\Delta\hat{p_x}\}\rangle|^2 + \frac{\text{ƛ}^2}{4}. \qquad \text{(B.30)}$$

Substituting Eqn. (B.29) in Eqn. (B.28) :

$$\begin{aligned} \langle \Delta\hat{x}^2 \rangle \langle \Delta\hat{p_x}^2 \rangle &\geq \frac{1}{4} |\langle \{\Delta\hat{x}, \Delta\hat{p_x}\} \rangle|^2 + \frac{\text{ƛ}^2}{4} \\ \Longrightarrow \langle \Delta\hat{x}^2 \rangle \langle \Delta\hat{p_x}^2 \rangle &- \frac{1}{4} |\langle \{\Delta\hat{x}, \Delta\hat{p_x}\} \rangle|^2 \geq \frac{\text{ƛ}^2}{4} \end{aligned} \tag{B.31}$$

which is nothing but the well known statement for the uncertainty principle.

APPENDIX C

Derivation of Moments

C.1 Continuous Version

The second order moments for a beam, can be calculated in the following manner:

$$\begin{aligned}\langle \hat{x}^2 \rangle &= \frac{\int_{-\infty}^{+\infty}\int_{-\infty}^{+\infty} \psi(x,y)^* \hat{x}^2 \psi(x,y) dxdy}{\int_{-\infty}^{+\infty}\int_{-\infty}^{+\infty} \psi(x,y)^* \psi(x,y) dxdy} \\ &= \frac{\int_{-\infty}^{+\infty}\int_{-\infty}^{+\infty} A(x,y) e^{-i\phi(x,y)} x^2 A(x,y) e^{i\phi(x,y)} dxdy}{\int_{-\infty}^{+\infty}\int_{-\infty}^{+\infty} A(x,y) e^{-i\phi(x,y)} A(x,y) e^{i\phi(x,y)} dxdy}\end{aligned}$$

as $\psi(x,y) = A(x,y)e^{i\phi(x,y)}$, $A(x,y)$ real (refer Eqn. (3.19)) and $\hat{x}^2 \rightarrow x^2$

$$\begin{aligned}&= \frac{\int_{-\infty}^{+\infty}\int_{-\infty}^{+\infty} (A(x,y))^2 x^2 dxdy}{\int_{-\infty}^{+\infty}\int_{-\infty}^{+\infty} (A(x,y))^2 dxdy} \\ &= \frac{\int_{-\infty}^{+\infty}\int_{-\infty}^{+\infty} I(x,y) x^2 dxdy}{\int_{-\infty}^{+\infty}\int_{-\infty}^{+\infty} I(x,y) dxdy} \qquad \text{(C.1)}\end{aligned}$$

In discretised form, one can write the above equation in the following manner:

$$\langle x^2 \rangle = \frac{\sum_{ij} x_{ij}^2 I_{ij}}{\sum_{ij} I_{ij}} \qquad \text{(C.2)}$$

where, i and j are the addressing indices of each of discretized location in the transverse detecting plane, over which the summation is carried out. This, for instance in our case is the CCD detection surface.

Similarly,

$$\langle \hat{y}^2 \rangle = \frac{\int_{-\infty}^{+\infty}\int_{-\infty}^{+\infty} I(x,y) y^2 dxdy}{\int_{-\infty}^{+\infty}\int_{-\infty}^{+\infty} I(x,y) dxdy}$$

$$\langle y^2 \rangle = \frac{\sum_{ij} y_{ij}^2 I_{ij}}{\sum_{ij} I_{ij}} \qquad \text{(C.3)}$$

$$\begin{aligned}
\langle \hat{p}_x^2 \rangle &= \frac{\int_{-\infty}^{+\infty}\int_{-\infty}^{+\infty} \psi(x,y)^* \hat{p}_x^2 \psi(x,y) dxdy}{\int_{-\infty}^{+\infty}\int_{-\infty}^{+\infty} I(x,y) dxdy} \\
&= \frac{\int_{-\infty}^{+\infty}\int_{-\infty}^{+\infty} A(x,y) e^{-i\phi(x,y)} \left(-i\text{ƛ}\frac{\partial}{\partial x}\right)\left(-i\text{ƛ}\frac{\partial}{\partial x}\right) A(x,y) e^{i\phi(x,y)} dxdy}{\int_{-\infty}^{+\infty}\int_{-\infty}^{+\infty} I(x,y) dxdy} \\
&= -\text{ƛ}^2 \frac{\int_{-\infty}^{+\infty}\int_{-\infty}^{+\infty} A(x,y) e^{-i\phi(x,y)} \frac{\partial}{\partial x}\left(\frac{\partial}{\partial x}\left(A(x,y) e^{i\phi(x,y)}\right)\right) dxdy}{\int_{-\infty}^{+\infty}\int_{-\infty}^{+\infty} I(x,y) dxdy}. \qquad \text{(C.4)}
\end{aligned}$$

Considering :

$$\frac{\partial}{\partial x} u(x)v(x) = u(x)\frac{\partial}{\partial x} v(x) + v(x)\frac{\partial}{\partial x} u(x)$$

Integrating on both sides :

$$\begin{aligned}
\int_{-\infty}^{+\infty} \frac{\partial}{\partial x} u(x)v(x) dx &= \int_{-\infty}^{+\infty} u(x)\frac{\partial}{\partial x} v(x) dx + \int_{-\infty}^{+\infty} v(x)\frac{\partial}{\partial x} u(x) dx \\
\int_{-\infty}^{+\infty} u(x)\frac{\partial}{\partial x} v(x) dx. &= \int_{-\infty}^{+\infty} \frac{\partial}{\partial x} u(x)v(x) dx - \int_{-\infty}^{+\infty} v(x)\frac{\partial}{\partial x} u(x) dx
\end{aligned}$$

In the present case, in Eqn.(C.4) :

$$\begin{aligned}
u(x) &= A(x,y) e^{-i\phi(x,y)} \\
v(x) &= \frac{\partial}{\partial x}\left(A(x,y) e^{i\phi(x,y)}\right) \qquad \text{(C.5)}
\end{aligned}$$

so that :

$$\begin{aligned}
A(x,y) e^{-i\phi(x,y)} \frac{\partial}{\partial x}\left(\frac{\partial}{\partial x}\left(A(x,y) e^{i\phi(x,y)}\right)\right) &= \\
\frac{\partial}{\partial x}\left(\left(A(x,y) e^{-i\phi(x,y)}\right)\left(\frac{\partial}{\partial x} A(x,y) e^{i\phi(x,y)}\right)\right) - & \\
\frac{\partial}{\partial x}\left(A(x,y) e^{i\phi(x,y)}\right)\frac{\partial}{\partial x}\left(A(x,y) e^{-i\phi(x,y)}\right) & \qquad \text{(C.6)}
\end{aligned}$$

and thus :

$$\begin{aligned}\int_{-\infty}^{+\infty} A(x,y)e^{-i\phi(x,y)}\frac{\partial}{\partial x}\left(\frac{\partial}{\partial x}\left(A(x,y)e^{i\phi(x,y)}\right)\right)dx &= \\ \int_{-\infty}^{+\infty}\frac{\partial}{\partial x}\left(\left(A(x,y)e^{-i\phi(x,y)}\right)\left(\frac{\partial}{\partial x}A(x,y)e^{i\phi(x,y)}\right)\right)dx - & \\ \int_{-\infty}^{+\infty}\frac{\partial}{\partial x}\left(A(x,y)e^{i\phi(x,y)}\right)\frac{\partial}{\partial x}\left(A(x,y)e^{-i\phi(x,y)}\right)dx & \\ = & \\ \left(\left(A(x,y)e^{-i\phi(x,y)}\right)\left(\frac{\partial}{\partial x}A(x,y)e^{i\phi(x,y)}\right)\right)_{-\infty}^{+\infty} - & \\ \int_{-\infty}^{+\infty}\frac{\partial}{\partial x}\left(A(x,y)e^{i\phi(x,y)}\right)\frac{\partial}{\partial x}\left(A(x,y)e^{-i\phi(x,y)}\right)dx &\end{aligned}$$

Now since, $A(x,y)e^{i\phi(x,y)}$ is a well behaved wave function which goes to zero at $-\infty$ or $+\infty$, $\left(\left(A(x,y)e^{-i\phi(x,y)}\right)\left(\frac{\partial}{\partial x}A(x,y)e^{i\phi(x,y)}\right)\right)_{-\infty}^{+\infty} = 0$. Hence,

$$\begin{aligned}\int_{-\infty}^{+\infty} A(x,y)e^{-i\phi(x,y)}\frac{\partial}{\partial x}\left(\frac{\partial}{\partial x}\left(A(x,y)e^{i\phi(x,y)}\right)\right)dx &= \\ -\int_{-\infty}^{+\infty}\frac{\partial}{\partial x}\left(A(x,y)e^{i\phi(x,y)}\right)\frac{\partial}{\partial x}\left(A(x,y)e^{-i\phi(x,y)}\right)dx &\end{aligned}$$

Eqn. (C.4) becomes,

$$\begin{aligned}\langle\hat{p}_x^2\rangle &= \text{ƛ}^2\frac{\int_{-\infty}^{+\infty}\int_{-\infty}^{+\infty}\frac{\partial}{\partial x}\left(A(x,y)e^{i\phi(x,y)}\right)\frac{\partial}{\partial x}\left(A(x,y)e^{-i\phi(x,y)}\right)dxdy}{\int_{-\infty}^{+\infty}\int_{-\infty}^{+\infty}I(x,y)dxdy} \\ &= \text{ƛ}^2\frac{\int_{-\infty}^{+\infty}\int_{-\infty}^{+\infty}\left(\frac{\partial A(x,y)}{\partial x}e^{i\phi(x,y)} + iA(x,y)e^{i\phi(x,y)}\frac{\partial\phi(x,y)}{\partial x}\right)}{\int_{-\infty}^{+\infty}\int_{-\infty}^{+\infty}I(x,y)dxdy}\times \\ &\qquad\frac{\int_{-\infty}^{+\infty}\int_{-\infty}^{+\infty}\left(\frac{\partial A(x,y)}{\partial x}e^{-i\phi(x,y)} - iA(x,y)e^{-i\phi(x,y)}\frac{\partial\phi(x,y)}{\partial x}\right)dxdy}{\int_{-\infty}^{+\infty}\int_{-\infty}^{+\infty}I(x,y)dxdy} \\ &= \text{ƛ}^2\frac{\int_{-\infty}^{+\infty}\int_{-\infty}^{+\infty}\left(\frac{\partial A(x,y)}{\partial x}\right)^2 + \left(A(x,y)\frac{\partial\phi(x,y)}{\partial x}\right)^2 dxdy}{\int_{-\infty}^{+\infty}\int_{-\infty}^{+\infty}I(x,y)dxdy} \\ &= \text{ƛ}^2\frac{\int_{-\infty}^{+\infty}\int_{-\infty}^{+\infty}\left(\frac{\partial A(x,y)}{\partial x}\right)^2 + \left(A(x,y)\frac{\partial\phi(x,y)}{\partial x}\right)^2 dxdy}{\int_{-\infty}^{+\infty}\int_{-\infty}^{+\infty}I(x,y)dxdy}\end{aligned}$$

From Eqn. (3.20), $\left(\frac{\partial A(x,y)}{\partial x}\right)^2 = \frac{1}{4I(x,y)}\left(\frac{\partial I(x,y)}{\partial x}\right)^2$ and $\left(A(x,y)\frac{\partial\phi(x,y)}{\partial x}\right)^2 = I(x,y)\left(\frac{\partial\phi(x,y)}{\partial x}\right)^2$.

Therefore,

$$\langle \hat{p}_x^2 \rangle = \text{ƛ}^2 \frac{\int_{-\infty}^{+\infty}\int_{-\infty}^{+\infty} \frac{1}{4I(x,y)} \left(\frac{\partial I(x,y)}{\partial x}\right)^2 + I(x,y)\left(\frac{\partial \phi(x,y)}{\partial x}\right)^2 dxdy}{\int_{-\infty}^{+\infty}\int_{-\infty}^{+\infty} I(x,y)dxdy}.$$

The discretised version of the same is:

$$\langle p_x^2 \rangle = \text{ƛ}^2 \frac{\sum_{ij} \frac{1}{4I_{ij}} \left(\frac{\partial I}{\partial x}\right)_{ij}^2}{\sum_{ij} I_{ij}} + \text{ƛ}^2 \frac{\sum_{ij} \left(\frac{\partial \phi(x,y)}{\partial x}\right)_{ij}^2 I_{ij}}{\sum_{ij} I_{ij}}. \tag{C.7}$$

By similar arguments,

$$\langle \hat{p}_y^2 \rangle = \text{ƛ}^2 \frac{\int_{-\infty}^{+\infty}\int_{-\infty}^{+\infty} \frac{1}{4I(x,y)} \left(\frac{\partial I(x,y)}{\partial y}\right)^2 + I(x,y)\left(\frac{\partial \phi(x,y)}{\partial y}\right)^2 dxdy}{\int_{-\infty}^{+\infty}\int_{-\infty}^{+\infty} I(x,y)dxdy}.$$

In discrete form:

$$\langle p_y^2 \rangle = \text{ƛ}^2 \frac{\sum_{ij} \frac{1}{4I_{ij}} \left(\frac{\partial I}{\partial y}\right)_{ij}^2}{\sum_{ij} I_{ij}} + \text{ƛ}^2 \frac{\sum_{ij} \left(\frac{\partial \phi(x,y)}{\partial y}\right)_{ij}^2 I_{ij}}{\sum_{ij} I_{ij}}. \tag{C.8}$$

$$\begin{aligned}
\langle \hat{p}_x \hat{p}_y \rangle &= \frac{\int_{-\infty}^{+\infty}\int_{-\infty}^{+\infty} \psi^*(x,y)\left(-i\text{ƛ}\frac{\partial}{\partial x}\right)\left(-i\text{ƛ}\frac{\partial}{\partial y}\right)\psi(x,y)dxdy}{\int_{-\infty}^{+\infty}\int_{-\infty}^{+\infty} I(x,y)dxdy} \\
&= \frac{\int_{-\infty}^{+\infty}\int_{-\infty}^{+\infty} A(x,y)e^{-i\phi(x,y)}\left(-i\text{ƛ}\frac{\partial}{\partial x}\right)\left(-i\text{ƛ}\frac{\partial}{\partial y}\right)A(x,y)e^{i\phi(x,y)}dxdy}{\int_{-\infty}^{+\infty}\int_{-\infty}^{+\infty} I(x,y)dxdy} \\
&= -\text{ƛ}^2 \frac{\int_{-\infty}^{+\infty}\int_{-\infty}^{+\infty} A(x,y)e^{-i\phi(x,y)}\left(\frac{\partial}{\partial x}\left(\frac{\partial}{\partial y}\left(A(x,y)e^{i\phi(x,y)}\right)\right)\right)dxdy}{\int_{-\infty}^{+\infty}\int_{-\infty}^{+\infty} I(x,y)dxdy}
\end{aligned}$$

Using Eqs. (C.5), with $u(x) = A(x,y)e^{-i\phi(x,y)}$ and $v(x) = \frac{\partial}{\partial y}\left(A(x,y)e^{i\phi(x,y)}\right)$,

$$\begin{aligned}
A(x,y)e^{-i\phi(x,y)}\left(\frac{\partial}{\partial x}\left(\frac{\partial}{\partial y}\left(A(x,y)e^{i\phi(x,y)}\right)\right)\right) &= \\
\frac{\partial}{\partial x}\left(A(x,y)e^{-i\phi(x,y)}\left(\frac{\partial}{\partial y}\left(A(x,y)e^{i\phi(x,y)}\right)\right)\right) - & \\
\frac{\partial}{\partial y}\left(A(x,y)e^{i\phi(x,y)}\right)\frac{\partial}{\partial x}\left(A(x,y)e^{-i\phi(x,y)}\right) &
\end{aligned}$$

Integrating with respect to x on both the sides,

$$\int_{-\infty}^{+\infty} A(x,y)e^{-i\phi(x,y)}\left(\frac{\partial}{\partial x}\left(\frac{\partial}{\partial y}\left(A(x,y)e^{i\phi(x,y)}\right)\right)\right)dx = \int_{-\infty}^{+\infty}\frac{\partial}{\partial x}\left(A(x,y)e^{-i\phi(x,y)}\left(\frac{\partial}{\partial y}\left(A(x,y)e^{i\phi(x,y)}\right)\right)\right)dx - \int_{-\infty}^{+\infty}\frac{\partial}{\partial y}\left(A(x,y)e^{i\phi(x,y)}\right)\frac{\partial}{\partial x}\left(A(x,y)e^{-i\phi(x,y)}\right)dx$$

from which the first term in R.H.S. is zero because $\psi(x,y)$ is well behaved wave function. Hence,

$$\int_{-\infty}^{+\infty} A(x,y)e^{-i\phi(x,y)}\left(\frac{\partial}{\partial x}\left(\frac{\partial}{\partial y}\left(A(x,y)e^{i\phi(x,y)}\right)\right)\right)dx = -\int_{-\infty}^{+\infty}\frac{\partial}{\partial y}\left(A(x,y)e^{i\phi(x,y)}\right)\frac{\partial}{\partial x}\left(A(x,y)e^{-i\phi(x,y)}\right)dx$$

Now, Eqn. (C.9) becomes,

$$\begin{aligned}
\langle\hat{p}_x\hat{p}_y\rangle &= \hbar^2\frac{\int_{-\infty}^{+\infty}\int_{-\infty}^{+\infty}\frac{\partial}{\partial y}\left(A(x,y)e^{i\phi(x,y)}\right)\frac{\partial}{\partial x}\left(A(x,y)e^{-i\phi(x,y)}\right)dxdy}{\int_{-\infty}^{+\infty}\int_{-\infty}^{+\infty}I(x,y)dxdy} \\
&= \hbar^2\frac{\int_{-\infty}^{+\infty}\int_{-\infty}^{+\infty}\left(\frac{\partial A(x,y)}{\partial y}e^{i\phi(x,y)}+iA(x,y)\frac{\partial\phi(x,y)}{\partial y}e^{i\phi(x,y)}\right)}{\int_{-\infty}^{+\infty}\int_{-\infty}^{+\infty}I(x,y)dxdy}\times \\
&\quad \frac{\int_{-\infty}^{+\infty}\int_{-\infty}^{+\infty}\left(\frac{\partial A(x,y)}{\partial x}e^{-i\phi(x,y)}-iA(x,y)\frac{\partial\phi(x,y)}{\partial x}e^{-i\phi(x,y)}\right)dxdy}{\int_{-\infty}^{+\infty}\int_{-\infty}^{+\infty}I(x,y)dxdy} \\
&= \hbar^2\frac{\int_{-\infty}^{+\infty}\int_{-\infty}^{+\infty}\left(\frac{\partial A(x,y)}{\partial y}+iA(x,y)\frac{\partial\phi(x,y)}{\partial y}\right)\left(\frac{\partial A(x,y)}{\partial x}-iA(x,y)\frac{\partial\phi(x,y)}{\partial x}\right)dxdy}{\int_{-\infty}^{+\infty}\int_{-\infty}^{+\infty}I(x,y)dxdy} \\
&= \hbar^2\frac{\int_{-\infty}^{+\infty}\int_{-\infty}^{+\infty}\left(\frac{\partial A(x,y)}{\partial y}\frac{\partial A(x,y)}{\partial x}+iA(x,y)\frac{\partial\phi(x,y)}{\partial y}\frac{\partial A(x,y)}{\partial x}\right)dxdy}{\int_{-\infty}^{+\infty}\int_{-\infty}^{+\infty}I(x,y)dxdy}+ \\
&\quad \hbar^2\frac{\int_{-\infty}^{+\infty}\int_{-\infty}^{+\infty}\left(-iA(x,y)\frac{\partial A(x,y)}{\partial y}\frac{\partial\phi(x,y)}{\partial x}+A^2(x,y)\frac{\partial\phi(x,y)}{\partial y}\frac{\partial\phi(x,y)}{\partial x}\right)dxdy}{\int_{-\infty}^{+\infty}\int_{-\infty}^{+\infty}I(x,y)dxdy} \\
&= \hbar^2\frac{\int_{-\infty}^{+\infty}\int_{-\infty}^{+\infty}\left(\frac{\partial A(x,y)}{\partial y}\frac{\partial A(x,y)}{\partial x}+A^2(x,y)\frac{\partial\phi(x,y)}{\partial y}\frac{\partial\phi(x,y)}{\partial x}\right)dxdy}{\int_{-\infty}^{+\infty}\int_{-\infty}^{+\infty}I(x,y)dxdy}+ \\
&\quad \hbar^2\frac{\int_{-\infty}^{+\infty}\int_{-\infty}^{+\infty}\left(iA(x,y)\frac{\partial\phi(x,y)}{\partial y}\frac{\partial A(x,y)}{\partial x}-iA(x,y)\frac{\partial A(x,y)}{\partial y}\frac{\partial\phi(x,y)}{\partial x}\right)dxdy}{\int_{-\infty}^{+\infty}\int_{-\infty}^{+\infty}I(x,y)dxdy}
\end{aligned}$$

Again refering to Eqns. (C.5), with $u(x) = A^2(x,y) = I(x,y)$, $v(x) = \frac{\partial\phi(x,y)}{\partial y}$,

$$\begin{aligned}
\int_{-\infty}^{+\infty} \frac{\partial}{\partial x}\left(I(x,y)\frac{\partial\phi(x,y)}{\partial y}\right)dx &= \int_{-\infty}^{+\infty}\frac{\partial I(x,y)}{\partial x}\frac{\partial\phi(x,y)}{\partial y}dx + \int_{-\infty}^{+\infty} I(x,y)\frac{\partial}{\partial x}\left(\frac{\partial\phi(x,y)}{\partial y}\right)dx \\
\left(I(x,y)\frac{\partial\phi(x,y)}{\partial y}\right)_{-\infty}^{+\infty} &= \int_{-\infty}^{+\infty}\frac{\partial I(x,y)}{\partial x}\frac{\partial\phi(x,y)}{\partial y}dx + \int_{-\infty}^{+\infty} I(x,y)\frac{\partial}{\partial x}\left(\frac{\partial\phi(x,y)}{\partial y}\right)dx \\
0 &= \int_{-\infty}^{+\infty}\frac{\partial I(x,y)}{\partial x}\frac{\partial\phi(x,y)}{\partial y}dx + \int_{-\infty}^{+\infty} I(x,y)\frac{\partial}{\partial x}\left(\frac{\partial\phi(x,y)}{\partial y}\right)dx
\end{aligned}$$

as $I(x,y) = 0$ at $-\infty$ or $+\infty$

$$\begin{aligned}
\int_{-\infty}^{+\infty}\frac{\partial I(x,y)}{\partial x}\frac{\partial\phi(x,y)}{\partial y}dx &= -\int_{-\infty}^{+\infty} I(x,y)\frac{\partial}{\partial x}\left(\frac{\partial\phi(x,y)}{\partial y}\right)dx \\
\text{Therefore, } \int_{-\infty}^{+\infty} A(x,y)\frac{\partial A(x,y)}{\partial x}\frac{\partial\phi(x,y)}{\partial y}dx &= -\frac{1}{2}\int_{-\infty}^{+\infty} I(x,y)\frac{\partial}{\partial x}\left(\frac{\partial\phi(x,y)}{\partial y}\right)dx \\
\text{Similarly, } \int_{-\infty}^{+\infty} A(x,y)\frac{\partial\phi(x,y)}{\partial x}\frac{\partial A(x,y)}{\partial y}dy &= -\frac{1}{2}\int_{-\infty}^{+\infty} I(x,y)\frac{\partial}{\partial y}\left(\frac{\partial\phi(x,y)}{\partial x}\right)dy
\end{aligned}$$

Substituting the above in Eqn. (C.9),

$$\begin{aligned}
\langle\hat{p}_x\hat{p}_y\rangle &= \text{ƛ}^2\frac{\int_{-\infty}^{+\infty}\int_{-\infty}^{+\infty}\left(\frac{\partial A(x,y)}{\partial y}\frac{\partial A(x,y)}{\partial x} + A^2(x,y)\frac{\partial\phi(x,y)}{\partial y}\frac{\partial\phi(x,y)}{\partial x}\right)dxdy}{\int_{-\infty}^{+\infty}\int_{-\infty}^{+\infty} I(x,y)dxdy} + \\
&\quad i\text{ƛ}^2\frac{\int_{-\infty}^{+\infty}\int_{-\infty}^{+\infty} -\frac{1}{2}I(x,y)\frac{\partial}{\partial x}\left(\frac{\partial\phi(x,y)}{\partial y}\right) + \frac{1}{2}I(x,y)\frac{\partial}{\partial y}\left(\frac{\partial\phi(x,y)}{\partial x}\right)dxdy}{\int_{-\infty}^{+\infty}\int_{-\infty}^{+\infty} I(x,y)dxdy}
\end{aligned}$$

The second term in R.H.S. in the above equation is equal to 0 since $\frac{\partial}{\partial x}\left(\frac{\partial\phi(x,y)}{\partial y}\right) = \frac{\partial}{\partial y}\left(\frac{\partial\phi(x,y)}{\partial x}\right)$. So,

$$\langle\hat{p}_x\hat{p}_y\rangle = \text{ƛ}^2\frac{\int_{-\infty}^{+\infty}\int_{-\infty}^{+\infty}\left(\frac{\partial A(x,y)}{\partial y}\frac{\partial A(x,y)}{\partial x} + A^2(x,y)\frac{\partial\phi(x,y)}{\partial y}\frac{\partial\phi(x,y)}{\partial x}\right)dxdy}{\int_{-\infty}^{+\infty}\int_{-\infty}^{+\infty} I(x,y)dxdy}$$

from Eqn. (3.20),

$$= \text{ƛ}^2\frac{\int_{-\infty}^{+\infty}\int_{-\infty}^{+\infty}\left(\frac{1}{4I(x,y)}\frac{\partial I(x,y)}{\partial y}\frac{\partial I(x,y)}{\partial x} + I(x,y)\frac{\partial\phi(x,y)}{\partial y}\frac{\partial\phi(x,y)}{\partial x}\right)dxdy}{\int_{-\infty}^{+\infty}\int_{-\infty}^{+\infty} I(x,y)dxdy}$$

In discretised form:

$$\langle\hat{p}_x\hat{p}_y\rangle = \text{ƛ}^2\frac{\sum_{ij}\frac{1}{4I_{ij}}\left(\frac{\partial I}{\partial x}\right)_{ij}\left(\frac{\partial I}{\partial y}\right)_{ij}}{\sum_{ij} I_{ij}} + \text{ƛ}^2\frac{\sum_{ij}\left(\frac{\partial\phi(x,y)}{\partial x}\right)_{ij}\left(\frac{\partial\phi(x,y)}{\partial y}\right)_{ij} I_{ij}}{\sum_{ij} I_{ij}} \quad \text{(C.9)}$$

Also, since $\langle \hat{p}_x \hat{p}_y \rangle = \langle \hat{p}_y \hat{p}_x \rangle$,

$$\langle \hat{p}_y \hat{p}_x \rangle = \text{ƛ}^2 \frac{\int_{-\infty}^{+\infty} \int_{-\infty}^{+\infty} \left(\frac{1}{4I(x,y)} \frac{\partial I(x,y)}{\partial y} \frac{\partial I(x,y)}{\partial x} + I(x,y) \frac{\partial \phi(x,y)}{\partial y} \frac{\partial \phi(x,y)}{\partial x} \right) dxdy}{\int_{-\infty}^{+\infty} \int_{-\infty}^{+\infty} I(x,y) dxdy}$$

and,

$$\langle \hat{p}_y \hat{p}_x \rangle = \text{ƛ}^2 \frac{\sum_{ij} \frac{1}{4I_{ij}} \left(\frac{\partial I}{\partial y} \right)_{ij} \left(\frac{\partial I}{\partial x} \right)_{ij}}{\sum_{ij} I_{ij}} + \text{ƛ}^2 \frac{\sum_{ij} \left(\frac{\partial \phi(x,y)}{\partial y} \right)_{ij} \left(\frac{\partial \phi(x,y)}{\partial x} \right)_{ij} I_{ij}}{\sum_{ij} I_{ij}} \quad \text{(C.10)}$$

$$\begin{aligned}
\langle \frac{1}{2} \{ \hat{x}, \hat{p}_x \} \rangle &= \frac{\int_{-\infty}^{+\infty} \int_{-\infty}^{+\infty} \psi(x,y)^* \frac{1}{2} \{ \hat{x}, \hat{p}_x \} \psi(x,y) dxdy}{\int_{-\infty}^{+\infty} \int_{-\infty}^{+\infty} I(x,y) dxdy} \\
&= \frac{\int_{-\infty}^{+\infty} \int_{-\infty}^{+\infty} \psi(x,y)^* \frac{1}{2} \left(\hat{x}\hat{p}_x + \hat{p}_x \hat{x} \right) \psi(x,y) dxdy}{\int_{-\infty}^{+\infty} \int_{-\infty}^{+\infty} I(x,y) dxdy} \\
&= \frac{\int_{-\infty}^{+\infty} \int_{-\infty}^{+\infty} A(x,y) e^{-i\phi(x,y)} \frac{1}{2} \left(\hat{x}\hat{p}_x + \hat{p}_x \hat{x} \right) A(x,y) e^{i\phi(x,y)} dxdy}{\int_{-\infty}^{+\infty} \int_{-\infty}^{+\infty} I(x,y) dxdy} \\
&= \frac{\int_{-\infty}^{+\infty} \int_{-\infty}^{+\infty} A(x,y) e^{-i\phi(x,y)} \frac{1}{2} \left(\hat{x}\hat{p}_x \right) A(x,y) e^{i\phi(x,y)} dxdy}{\int_{-\infty}^{+\infty} \int_{-\infty}^{+\infty} I(x,y) dxdy} + \\
&\quad \frac{\int_{-\infty}^{+\infty} \int_{-\infty}^{+\infty} A(x,y) e^{-i\phi(x,y)} \frac{1}{2} \left(\hat{p}_x \hat{x} \right) A(x,y) e^{i\phi(x,y)} dxdy}{\int_{-\infty}^{+\infty} \int_{-\infty}^{+\infty} I(x,y) dxdy} \\
&= \frac{\int_{-\infty}^{+\infty} \int_{-\infty}^{+\infty} A(x,y) e^{-i\phi(x,y)} \frac{1}{2} \left(x \left(-i\text{ƛ} \frac{\partial}{\partial x} \right) \right) A(x,y) e^{i\phi(x,y)} dxdy}{\int_{-\infty}^{+\infty} \int_{-\infty}^{+\infty} I(x,y) dxdy} + \\
&\quad \frac{\int_{-\infty}^{+\infty} \int_{-\infty}^{+\infty} A(x,y) e^{-i\phi(x,y)} \frac{1}{2} \left(\left(-i\text{ƛ} \frac{\partial}{\partial x} \right) x \right) A(x,y) e^{i\phi(x,y)} dxdy}{\int_{-\infty}^{+\infty} \int_{-\infty}^{+\infty} I(x,y) dxdy}
\end{aligned}$$

$$
\begin{aligned}
= & \frac{\int_{-\infty}^{+\infty}\int_{-\infty}^{+\infty} A(x,y)e^{-i\phi(x,y)}\frac{1}{2}\left(x(-i\lambda)\frac{\partial A(x,y)}{\partial x}e^{i\phi(x,y)}\right)dxdy}{\int_{-\infty}^{+\infty}\int_{-\infty}^{+\infty} I(x,y)dxdy} + \\
& \frac{\int_{-\infty}^{+\infty}\int_{-\infty}^{+\infty} A(x,y)e^{-i\phi(x,y)}\frac{1}{2}\left(x\lambda A(x,y)\frac{\partial \phi(x,y)}{\partial x}e^{i\phi(x,y)}\right)dxdy}{\int_{-\infty}^{+\infty}\int_{-\infty}^{+\infty} I(x,y)dxdy} + \\
& \frac{\int_{-\infty}^{+\infty}\int_{-\infty}^{+\infty} A(x,y)e^{-i\phi(x,y)}\frac{1}{2}\left((-i\lambda)\frac{\partial A(x,y)}{\partial x}e^{i\phi(x,y)}x\right)dxdy}{\int_{-\infty}^{+\infty}\int_{-\infty}^{+\infty} I(x,y)dxdy} + \\
& \frac{\int_{-\infty}^{+\infty}\int_{-\infty}^{+\infty} A(x,y)e^{-i\phi(x,y)}\frac{1}{2}\left(\lambda A(x,y)\frac{\partial \phi(x,y)}{\partial x}e^{i\phi(x,y)}x\right)dxdy}{\int_{-\infty}^{+\infty}\int_{-\infty}^{+\infty} I(x,y)dxdy} + \\
& \frac{\int_{-\infty}^{+\infty}\int_{-\infty}^{+\infty} A(x,y)e^{-i\phi(x,y)}\frac{1}{2}\left((-i\lambda)A(x,y)e^{i\phi(x,y)}\right)dxdy}{\int_{-\infty}^{+\infty}\int_{-\infty}^{+\infty} I(x,y)dxdy} \\
= & \frac{\int_{-\infty}^{+\infty}\int_{-\infty}^{+\infty}\left((-i\lambda)A(x,y)x\frac{\partial A(x,y)}{\partial x} + \frac{1}{2}(-i\lambda)A^2(x,y) + \lambda A^2(x,y)x\frac{\partial \phi(x,y)}{\partial x}\right)dxdy}{\int_{-\infty}^{+\infty}\int_{-\infty}^{+\infty} I(x,y)dxdy}
\end{aligned}
$$

Considering,

$$
(-i\lambda)\frac{1}{2}\int_{-\infty}^{+\infty}\frac{\partial}{\partial x}A^2(x,y)xdx = (-i\lambda)\int_{-\infty}^{+\infty}A(x,y)x\frac{\partial A(x,y)}{\partial x}dx + (-i\lambda)\frac{1}{2}\int_{-\infty}^{+\infty}A^2(x,y)dx
$$

Here, the amplitude square term ($A^2(x,y)$ in the R.H.S.) is an even function of x. A multiplication by another x makes the term inside the integral, an odd function with respect to x. Therefore, the integral has a value zero. On applying the above argument to Eqn. (C.11), it becomes:

$$
\begin{aligned}
= & \frac{\int_{-\infty}^{+\infty}\int_{-\infty}^{+\infty}\lambda A^2(x,y)x\frac{\partial \phi(x,y)}{\partial x}dxdy}{\int_{-\infty}^{+\infty}\int_{-\infty}^{+\infty} I(x,y)dxdy} \\
= & \lambda\frac{\int_{-\infty}^{+\infty}\int_{-\infty}^{+\infty} I(x,y)x\frac{\partial \phi(x,y)}{\partial x}dxdy}{\int_{-\infty}^{+\infty}\int_{-\infty}^{+\infty} I(x,y)dxdy}
\end{aligned}
$$

In a discrete fashion:

$$
\langle\frac{1}{2}\{\hat{x},\hat{p}_x\}\rangle = \lambda\frac{\sum_{ij}x_{ij}\left(\frac{\partial \phi(x,y)}{\partial x}\right)_{ij}I_{ij}}{\sum_{ij}I_{ij}} \tag{C.11}
$$

Similar arguments lead to,

$$\langle\frac{1}{2}\{\hat{y},\hat{p}_y\}\rangle = \text{ƛ}\frac{\int_{-\infty}^{+\infty}\int_{-\infty}^{+\infty} I(x,y)y\frac{\partial\phi(x,y)}{\partial y}dxdy}{\int_{-\infty}^{+\infty}\int_{-\infty}^{+\infty} I(x,y)dxdy}$$

$$\langle\frac{1}{2}\{\hat{y},\hat{p}_y\}\rangle = \text{ƛ}\frac{\sum_{ij} y_{ij}\left(\frac{\partial\phi(x,y)}{\partial y}\right)_{ij} I_{ij}}{\sum_{ij} I_{ij}} \tag{C.12}$$

$$\begin{aligned}
\langle\hat{x}\hat{p}_y\rangle &= \frac{\int_{-\infty}^{+\infty}\int_{-\infty}^{+\infty}\psi(x,y)^*\hat{x}\hat{p}_y\psi(x,y)dxdy}{\int_{-\infty}^{+\infty}\int_{-\infty}^{+\infty} I(x,y)dxdy} \\
&= \frac{\int_{-\infty}^{+\infty}\int_{-\infty}^{+\infty} A(x,y)e^{-i\phi(x,y)}\hat{x}\hat{p}_y A(x,y)e^{i\phi(x,y)}dxdy}{\int_{-\infty}^{+\infty}\int_{-\infty}^{+\infty} I(x,y)dxdy} \\
&= \frac{\int_{-\infty}^{+\infty}\int_{-\infty}^{+\infty} A(x,y)e^{-i\phi(x,y)}x\left(-i\text{ƛ}\frac{\partial}{\partial y}\right)A(x,y)e^{i\phi(x,y)}dxdy}{\int_{-\infty}^{+\infty}\int_{-\infty}^{+\infty} I(x,y)dxdy} \\
&= \frac{\int_{-\infty}^{+\infty}\int_{-\infty}^{+\infty} A(x,y)e^{-i\phi(x,y)}x\left(-i\text{ƛ}\right)\left(\frac{\partial A(x,y)}{\partial y}e^{i\phi(x,y)} + iA(x,y)\frac{\partial\phi(x,y)}{\partial y}e^{i\phi(x,y)}\right)dxdy}{\int_{-\infty}^{+\infty}\int_{-\infty}^{+\infty} I(x,y)dxdy} \\
&= \frac{\int_{-\infty}^{+\infty}\int_{-\infty}^{+\infty}\left(A(x,y)x\left(-i\text{ƛ}\right)\frac{\partial A(x,y)}{\partial y} + A^2(x,y)x\text{ƛ}\frac{\partial\phi(x,y)}{\partial y}\right)dxdy}{\int_{-\infty}^{+\infty}\int_{-\infty}^{+\infty} I(x,y)dxdy}
\end{aligned}$$

Considering,

$$\begin{aligned}
\int_{-\infty}^{+\infty}\frac{\partial\left(A^2(x,y)\right)}{\partial y}dy &= \int_{-\infty}^{+\infty} 2A(x,y)\frac{\partial A(x,y)}{\partial y}dy \\
\left(A^2(x,y)\right)_{-\infty}^{+\infty} &= \int_{-\infty}^{+\infty} 2A(x,y)\frac{\partial A(x,y)}{\partial y}dy \\
0 &= \int_{-\infty}^{+\infty} 2A(x,y)\frac{\partial A(x,y)}{\partial y}dy
\end{aligned}$$

Therefore,

$$\begin{aligned}
\langle\hat{x}\hat{p}_y\rangle &= \frac{\int_{-\infty}^{+\infty}\int_{-\infty}^{+\infty} A^2(x,y)x\text{ƛ}\frac{\partial\phi(x,y)}{\partial y}dxdy}{\int_{-\infty}^{+\infty}\int_{-\infty}^{+\infty} I(x,y)dxdy} \\
&= \text{ƛ}\frac{\int_{-\infty}^{+\infty}\int_{-\infty}^{+\infty} I(x,y)x\frac{\partial\phi(x,y)}{\partial y}dxdy}{\int_{-\infty}^{+\infty}\int_{-\infty}^{+\infty} I(x,y)dxdy}
\end{aligned}$$

and,

$$\langle \hat{x}\hat{p}_y \rangle = \text{ƛ} \frac{\sum_{ij} x_{ij} \left(\frac{\partial \phi(x,y)}{\partial y} \right)_{ij} I_{ij}}{\sum_{ij} I_{ij}}$$

Since, $\langle \hat{x}\hat{p}_y \rangle = \langle \hat{p}_y \hat{x} \rangle$,

$$\langle \hat{p}_y \hat{x} \rangle = \text{ƛ} \frac{\int_{-\infty}^{+\infty} \int_{-\infty}^{+\infty} I(x,y) x \frac{\partial \phi(x,y)}{\partial y} dxdy}{\int_{-\infty}^{+\infty} \int_{-\infty}^{+\infty} I(x,y) dxdy},$$

the discretised version being,

$$\langle \hat{p}_y \hat{x} \rangle = \text{ƛ} \frac{\sum_{ij} x_{ij} \left(\frac{\partial \phi(x,y)}{\partial y} \right)_{ij} I_{ij}}{\sum_{ij} I_{ij}}$$

Similarly,

$$\langle \hat{y}\hat{p}_x \rangle = \langle \hat{p}_x \hat{y} \rangle = \text{ƛ} \frac{\int_{-\infty}^{+\infty} \int_{-\infty}^{+\infty} I(x,y) y \frac{\partial \phi(x,y)}{\partial x} dxdy}{\int_{-\infty}^{+\infty} \int_{-\infty}^{+\infty} I(x,y) dxdy}$$

which can be written in a dicrete manner as:

$$\langle \hat{y}\hat{p}_x \rangle = \langle \hat{p}_x \hat{y} \rangle = \text{ƛ} \frac{\sum_{ij} y_{ij} \left(\frac{\partial \phi(x,y)}{\partial y} \right)_{ij} I_{ij}}{\sum_{ij} I_{ij}}$$

$$\begin{aligned}
\langle \hat{x}\hat{y} \rangle &= \frac{\int_{-\infty}^{+\infty} \int_{-\infty}^{+\infty} \psi(x,y)^* \hat{x}\hat{y}\psi(x,y) dxdy}{\int_{-\infty}^{+\infty} \int_{-\infty}^{+\infty} I(x,y) dxdy} \\
&= \frac{\int_{-\infty}^{+\infty} \int_{-\infty}^{+\infty} A(x,y) e^{-i\phi(x,y)} xy A(x,y) e^{i\phi(x,y)} dxdy}{\int_{-\infty}^{+\infty} \int_{-\infty}^{+\infty} I(x,y) dxdy} \\
&= \frac{\int_{-\infty}^{+\infty} \int_{-\infty}^{+\infty} A^2(x,y) xy dxdy}{\int_{-\infty}^{+\infty} \int_{-\infty}^{+\infty} I(x,y) dxdy} \\
&= \frac{\int_{-\infty}^{+\infty} \int_{-\infty}^{+\infty} I(x,y) xy dxdy}{\int_{-\infty}^{+\infty} \int_{-\infty}^{+\infty} I(x,y) dxdy}
\end{aligned}$$

The discrete version of the above is:

$$\langle \hat{x}\hat{y} \rangle = \frac{\sum_{ij} I_{ij} x_{ij} y_{ij}}{\sum_{ij} I_{ij}} \tag{C.13}$$

Since, $\langle \hat{x}\hat{y} \rangle = \langle \hat{y}\hat{x} \rangle$,

$$\langle \hat{y}\hat{x} \rangle = \frac{\int_{-\infty}^{+\infty}\int_{-\infty}^{+\infty} I(x,y)yxdxdy}{\int_{-\infty}^{+\infty}\int_{-\infty}^{+\infty} I(x,y)dxdy}$$

and,

$$\langle \hat{y}\hat{x} \rangle = \frac{\sum_{ij} I_{ij} y_{ij} x_{ij}}{\sum_{ij} I_{ij}} \tag{C.14}$$

C.2 Discrete Version

Considering the Eqns. (3.8), the discrete versions of the equations for the first moments and the second moments can be written as :

$$\begin{aligned} \langle \hat{x} \rangle &= \frac{\int_{-\infty}^{+\infty}\int_{-\infty}^{+\infty} xI(x,y)dxdy}{\int_{-\infty}^{+\infty}\int_{-\infty}^{+\infty} I(x,y)dxdy} \\ &= \frac{\sum_{ij} x_{ij} I_{ij}}{\sum_{ij} I_{ij}}, \end{aligned} \tag{C.15}$$

$$\begin{aligned} \langle \hat{y} \rangle &= \frac{\int_{-\infty}^{+\infty}\int_{-\infty}^{+\infty} yI(x,y)dxdy}{\int_{-\infty}^{+\infty}\int_{-\infty}^{+\infty} I(x,y)dxdy} \\ &= \frac{\sum_{ij} y_{ij} I_{ij}}{\sum_{ij} I_{ij}} \end{aligned} \tag{C.16}$$

$$\begin{aligned} \langle \hat{p}_x \rangle &= \text{ϰ}\frac{\int_{-\infty}^{+\infty}\int_{-\infty}^{+\infty} \frac{\partial\phi(x,y)}{\partial x} I(x,y)dxdy}{\int_{-\infty}^{+\infty}\int_{-\infty}^{+\infty} I(x,y)dxdy} \\ &= \frac{\sum_{ij} \left(\frac{x - x_0}{f}\right)_{ij} I_{ij}}{\sum_{ij} I_{ij}}, \end{aligned} \tag{C.17}$$

$$\begin{aligned} \langle \hat{p}_y \rangle &= \text{ϰ}\frac{\int_{-\infty}^{+\infty}\int_{-\infty}^{+\infty} \frac{\partial\phi(x,y)}{\partial y} I(x,y)dxdy}{\int_{-\infty}^{+\infty}\int_{-\infty}^{+\infty} I(x,y)dxdy} \\ &= \frac{\sum_{ij} \left(\frac{y - y_0}{f}\right)_{ij} I_{ij}}{\sum_{ij} I_{ij}}, \end{aligned} \tag{C.18}$$

and similarly the second moments are given by :

$$\begin{aligned}\langle \hat{x}^2 \rangle &= \frac{\int_{-\infty}^{+\infty}\int_{-\infty}^{+\infty} x^2 I(x,y)dxdy}{\int_{-\infty}^{+\infty}\int_{-\infty}^{+\infty} I(x,y)dxdy} \\ &= \frac{\sum_{ij} x_{ij}^2 I_{ij}}{\sum_{ij} I_{ij}}, \end{aligned} \tag{C.19}$$

$$\begin{aligned}\langle \hat{x}\hat{p}_x \rangle &= \text{ƛ}\frac{\int_{-\infty}^{+\infty}\int_{-\infty}^{+\infty} x\left(\frac{\partial\phi(x,y)}{\partial x}\right) I(x,y)dxdy}{\int_{-\infty}^{+\infty}\int_{-\infty}^{+\infty} I(x,y)dxdy} \\ &= \frac{\sum_{ij} x_{ij}\left(\frac{x-x_0}{f}\right)_{ij} I_{ij}}{\sum_{ij} I_{ij}}, \end{aligned} \tag{C.20}$$

$$\begin{aligned}\langle \hat{y}^2 \rangle &= \frac{\int_{-\infty}^{+\infty}\int_{-\infty}^{+\infty} y^2 I(x,y)dxdy}{\int_{-\infty}^{+\infty}\int_{-\infty}^{+\infty} I(x,y)dxdy} \\ &= \frac{\sum_{ij} y_{ij}^2 I_{ij}}{\sum_{ij} I_{ij}} \end{aligned} \tag{C.21}$$

$$\begin{aligned}\langle \hat{y}\hat{p}_y \rangle &= \text{ƛ}\frac{\int_{-\infty}^{+\infty}\int_{-\infty}^{+\infty} y\left(\frac{\partial\phi(x,y)}{\partial y}\right) I(x,y)dxdy}{\int_{-\infty}^{+\infty}\int_{-\infty}^{+\infty} I(x,y)dxdy} \\ &= \frac{\sum_{ij} y_{ij}\left(\frac{y-y_0}{f}\right)_{ij} I_{ij}}{\sum_{ij} I_{ij}}, \end{aligned} \tag{C.22}$$

$$\begin{aligned}\langle \hat{p}_x^2 \rangle &= \text{ƛ}^2\frac{\int_{-\infty}^{+\infty}\int_{-\infty}^{+\infty}\frac{1}{4I(x,y)}\left(\frac{\partial I(x,y)}{\partial x}\right)^2 dxdy}{\int_{-\infty}^{+\infty}\int_{-\infty}^{+\infty} I(x,y)dxdy} + \\ &\quad \text{ƛ}^2\frac{\int_{-\infty}^{+\infty}\int_{-\infty}^{+\infty}\left(\frac{\partial\phi}{\partial x}\right)^2 I(x,y)dxdy}{\int_{-\infty}^{+\infty}\int_{-\infty}^{+\infty} I(x,y)dxdy} \\ &= \text{ƛ}^2\frac{\sum_{ij}\frac{1}{4I_{ij}}\left(\frac{\partial I}{\partial x}\right)_{ij}^2}{\sum_{ij} I_{ij}} + \\ &\quad \frac{\sum_{ij}\left(\frac{x-x_0}{f}\right)_{ij}^2 I_{ij}}{\sum_{ij} I_{ij}}. \end{aligned} \tag{C.23}$$

$$
\begin{aligned}
\langle \hat{p}_y^2 \rangle &= \aleph^2 \frac{\int_{-\infty}^{+\infty}\int_{-\infty}^{+\infty} \frac{1}{4I(x,y)} \left(\frac{\partial I(x,y)}{\partial y}\right)^2}{\int_{-\infty}^{+\infty}\int_{-\infty}^{+\infty} I(x,y)dxdy} + \\
&\quad \aleph^2 \frac{\int_{-\infty}^{+\infty}\int_{-\infty}^{+\infty} \left(\frac{\partial \phi}{\partial y}\right)^2 I(x,y)dxdy}{\int_{-\infty}^{+\infty}\int_{-\infty}^{+\infty} I(x,y)dxdy} \\
&= \aleph^2 \frac{\sum_{ij} \frac{1}{4I_{ij}} \left(\frac{\partial I}{\partial y}\right)_{ij}^2}{\sum_{ij} I_{ij}} + \\
&\quad \frac{\sum_{ij} \left(\frac{y-y_0}{f}\right)_{ij}^2 I_{ij}}{\sum_{ij} I_{ij}}.
\end{aligned} \tag{C.24}
$$

$$
\begin{aligned}
\langle p_x p_y \rangle &= \aleph^2 \frac{\int_{-\infty}^{+\infty}\int_{-\infty}^{+\infty} \frac{1}{4I(x,y)} \left(\frac{\partial I(x,y)}{\partial x}\right)\left(\frac{\partial I(x,y)}{\partial y}\right) dxdy}{\int_{-\infty}^{+\infty}\int_{-\infty}^{+\infty} I(x,y)dxdy} + \\
&\quad \aleph^2 \frac{\int_{-\infty}^{+\infty}\int_{-\infty}^{+\infty} \left(\frac{\partial \phi}{\partial x}\right)\left(\frac{\partial \phi}{\partial y}\right) I(x,y)dxdy}{\int_{-\infty}^{+\infty}\int_{-\infty}^{+\infty} I(x,y)dxdy} \\
&= \aleph^2 \frac{\sum_{ij} \frac{1}{4I_{ij}} \left(\frac{\partial I}{\partial x}\right)_{ij} \left(\frac{\partial I}{\partial y}\right)_{ij}}{\sum_{ij} I_{ij}} + \\
&\quad \frac{\sum_{ij} \left(\frac{x-x_0}{f}\right)_{ij} \left(\frac{y-y_0}{f}\right)_{ij} I_{ij}}{\sum_{ij} I_{ij}}
\end{aligned} \tag{C.25}
$$

APPENDIX D

Details of Wavefront Sensor and Microlens Array

Table D.1: Wavefront Sensor Specifications

Wavefront Sensor	**Description**
Aperture size	5.95 mm $\times$ 4.76 mm max.
Camera resolution	1280 $\times$ 1024 Pixels max., selectable
Pixel size	4.65 μm $\times$ 4.65μm
Shutter	Global
Number of active lenslets	39 $\times$ 31
Wavefront accuracy	$\frac{\lambda}{15}$ rms (@ 633 nm)
Wavefront sensitivity	$\frac{\lambda}{50}$ rms (@ 633 nm)
Wavefront dynamic range	$> 100\lambda$ (@ 633 nm)
Local Wavefront curvature	> 7.4mm
Exposure range	79 μs - 65 ms
Frame rate	15 Hz. max.
Image digitization	8 bit
Optical input connector	C-Mount
Physical size (H $\times$ W $\times$ D)	34 mm $\times$ 32 mm $\times$ 45.5 mm
Power supply	< 1.5 W, via USB

Table D.2: Microlens Array Specifications

Microlens Array	**Description**
Included Microlens array	MLA150M-5C
Substrate material	Fused silica (quartz)
Wavelength range	300-1100 nm
Free aperture	$\oslash$ 9 mm
Lenslet grid type	Square grid
Lenslet pitch	150 μm
Lens shape	Round, Plano convex spherical
Lens diameter	146 μm
Coating	Chrome apertures
Reflectivity	$< 25\%$
Nominal focal length	5.2 mm
Effective focal length (mounted in SHWFS)	3.7 mm

LIST OF PAPERS BASED ON THESIS

Journal Papers

1. **Richa Sharma** and C.S.Narayanamurthy, *Single and double passage interferometric analysis of Pseudo-Random-Phase-Plates*, Optics Communications, Elsevier, 345, 2015, 37-46.

2. **Richa Sharma** and C.S.Narayanamurthy, *Characterization of Pseudo-Random-Phase-Plate as a Kolmogorov/non-Kolmogorov turbulence simulator using statistical parameters and the phase structure function*, Journal of Optics, Springer. (In press, published online August 11, 2015)

3. **Richa Sharma**, J. Solomon Ivan, and C. S. Narayanamurthy, *Wave propagation analysis using the Variance matrix*, Journal of Optical Society of America A., OSA, 31(10), 2014, 2185-2191.

4. **Richa Sharma**, J. Solomon Ivan, and C.S.Narayanamurthy, *Comparative statistical analysis of phase profiles of a pseudo random phase plate with Kolmogorov's phase screens*, Optik, Elsevier. (In press, published online August 19, 2015)

5. Lijo Thomas, J. Solomon Ivan, Ameen Yasir, **Richa Sharma**, Rakesh Kumar Singh, C. S. Narayanamurthy, and K. S. Dasgupta., *Phase-sharing using a Mach-Zehnder interferometer*, Applied Optics, 54(4), 2015, 699-706.

Conference Papers

1. **Richa Sharma** and C.S.Narayanamurthy, *Influence of Pseudo-Random-Phase-Plates' sequence in phase analysis with single and double passage interferometers*, International conference on Optics and Photonics (ICOP), Kolkata, India, 2015. (poster)

2. **Richa Sharma**, J. Solomon Ivan, and C. S. Narayanamurthy, *Hilbert transform pair method for phase profile retrieval of a pseudo random phase plate*, International conference on Optics & Opto-electronics (ICOL), Dehradun, India, 2014. (poster)

3. **Richa Sharma**, J. Solomon Ivan, and C. S. Narayanamurthy, *Study of a laser beam propagated through a random phase plate*, International conference on Optics & Opto-electronics (ICOL), Dehradun, India, 2014. (poster)

Papers under Preparation

1. Wave propagation analysis on a Double Passage through a Pseudo-Random-Phase-Plate.

2. Vortex beam propagation through a Pseudo-Random-Phase-Plate.